Lawrence Berkeley National Laboratory
LBL Publications

Title

CUPID pre-CDR

Permalink

https://escholarship.org/uc/item/5sz8q20k

Author

Group, The CUPID Interest

Publication Date

2019-07-22

Peer reviewed

eScholarship.org Powered by the California Digital Library
University of California

CUPID pre-CDR

CUPID Interest Group

July 23, 2019

arXiv:1907.09376v1 [physics.ins-det] 22 Jul 2019

Contents

1 Executive Summary **5**

2 Motivations **7**
2.1 Lepton number violation and neutrinoless double beta decay . . . 7
2.2 Isotope selection and summary of the current searches . . . 7
2.3 Proposed next-generation searches . . . 9
2.4 CUPID: the next-generation bolometric search for $0\nu\beta\beta$ decay . . . 9

3 Overview of the experiment **12**
3.1 CUPID detector concept . . . 12
3.2 Infrastructure introduction . . . 13
3.3 Cryogenics . . . 13
3.3.1 The CUORE cryostat . . . 13
3.3.2 Low-vibration environment . . . 14
3.3.3 Low-radioactivity environment . . . 16
3.3.4 Cooldown system and thermal performance . . . 16
3.3.5 CUORE cooldown . . . 17
3.3.6 Lessons learned . . . 17
3.3.7 Upgrades for CUPID . . . 17
3.3.8 CUORE precooling stage: the Fast Cooling System . . . 18
3.4 The CUORE Cryogeny Monitor and Control System . . . 19
3.5 Electric demand and infrastructures . . . 19
3.6 Water cooling system . . . 20
3.7 Detector assembly and installation . . . 21
3.7.1 Underground cleanroom facilities . . . 21
3.7.2 Other support facilities . . . 22
3.7.3 Gluing . . . 22
3.7.4 Mechanical assembly . . . 23
3.7.5 Wire bonding . . . 24
3.7.6 Closing and storage . . . 24
3.7.7 Detector installation . . . 25
3.7.8 Radon abatement . . . 25
3.8 Front-end electronics . . . 26
3.8.1 The back-end electronics system stage: anti-aliasing and DAQ . . . 26
3.8.2 Very front-end and Faraday room . . . 26
3.8.3 Power supply and stabilization pulser . . . 28
3.9 Computing infrastructure: data acquisition, storage, online processing, and monitoring . . . 28
3.10 Calibration systems . . . 29
3.10.1 Li_2MoO_4 calibration . . . 29
3.10.2 Light detector calibration . . . 29
3.11 Muon tagger . . . 29
3.12 Cryogenic testing infrastructure . . . 31
3.12.1 Underground cryostats at LNGS . . . 31
3.12.2 Cryostats outside LNGS . . . 32
3.12.3 Edelweiss-II cryostat at LSM . . . 32
3.12.4 CROSS cryostat at LSC . . . 32

4 Enrichment, purification, and crystallization **33**
4.1 Procurement of ^{100}Mo-enriched molybdenum . . . 33
4.2 Purification of materials for crystal growth . . . 33
4.2.1 Enriched ^{100}Mo purification . . . 33
4.2.2 Lithium purification . . . 35
4.3 Chemical processing and synthesis of Li_2MoO_4 . . . 35
4.4 Crystal growth by the low-thermal-gradient Czochralski technique . . . 35
4.5 Scintillation elements production and surface treatment . . . 36
4.6 Enriched ^{100}Mo recycling . . . 37
4.7 Other possible crystal growth methods . . . 37

4.7.1 Ordinary Czochralski crystal growth . . . 37
4.7.2 Crystal production by Bridgman method . . . 38
4.8 Quality assurance: detector prototypes and tests . . . 38

5 Phonon and light sensors **39**
5.1 Neutron transmutation doped Ge thermistors . . . 39
5.2 Heaters . . . 39
5.3 Baseline technology: Ge light absorbers with NTD sensors . . . 40
5.4 Alternative Options . . . 40
5.4.1 Neganov-Luke-assisted NTDs . . . 40
5.4.2 Transition edge sensors . . . 42
5.4.3 Kinetic inductance detectors . . . 43
5.5 Light collection optimization . . . 45
5.6 Thermal and mechanical support . . . 45

6 Material selection and treatment **46**
6.0.1 Surface cleaning . . . 46
6.0.2 Material handling and critical storage . . . 46
6.1 Radiopurity assessment . . . 47
6.1.1 HPGe γ ray spectroscopy . . . 47
6.1.2 Neutron activation analysis . . . 48
6.1.3 ICP mass spectrometry . . . 48
6.1.4 Surface measurements . . . 48

7 Background sources and suppression **50**
7.1 Background sources and their mitigation . . . 50
7.1.1 α/β discrimination . . . 51
7.1.2 Rejection of 2ν background . . . 52
7.2 Background in CUORE and CUPID-0 . . . 53
7.2.1 CUORE background model . . . 53
7.2.2 CUPID-0 background model . . . 55
7.3 Background in CUPID-Mo demonstrator . . . 56
7.4 Predicted CUPID backgrounds . . . 56
7.4.1 ^{238}U, ^{232}Th from close sources . . . 57
7.4.2 ^{238}U, ^{232}Th in the cryostat and radiation shields . . . 60
7.4.3 Cosmogenic Isotopes in the crystals and materials . . . 60
7.4.4 Neutron-induced backgrounds . . . 60
7.4.5 Muon-induced background . . . 61
7.4.6 Neutrino-induced background . . . 61

8 Phased Deployment **62**

9 Physics sensitivity and other measurements **63**
9.1 Sensitivity to $0\nu\beta\beta$ decay . . . 63
9.2 Exotic processes . . . 65
9.2.1 Other double beta decays . . . 65
9.2.2 Violations of fundamental principles . . . 66
9.2.3 Tri-nucleon decays . . . 66
9.2.4 Dark Matter . . . 67

10 Alternative configuration: enriched TeO_2 detectors **68**
10.1 Enriched $^{130}TeO_2$ raw material for crystal growth . . . 68
10.2 Enriched $^{130}TeO_2$ crystal growth . . . 69
10.3 Recovery and recycling . . . 69

11 Implementation and Timeline **69**

12 CUPID Group of Interest **70**

13 Bibliography **72**

Acronyms

$0\nu\beta\beta$ - Neutrinoless Double Beta Decay

$2\nu\beta\beta$ - Two-neutrino Double Beta Decay

BI - Background Index

BM - Background Model

C-TAL - CUORE Towers Assembly Line

DM - Dark Matter

DR - Diluition Refrigerator

DU - Diluition Unit

FCS - Fast Cooling System

FCU - Fast Cooling Unit

IO - Inverted Ordering

IVC - Inner Vacuum Chamber

KIDs - Kinetic Inductance Detectors

LD - Light Detector

LNGS - Laboratori Nazionali del Gran Sasso

LSM - Laboratoire Souterrain de Modane

MC - Mixing Chamber

NAA - Neutron Activation Analysis

NL - Neganov-Luke

NME - Nuclear Matrix Element

NTD - Neutron Transmutation Doped (Ge thermistor)

OVC - Outer Vacuum Chamber

PEP - Pauli exclusion principle

PGA - Programmable Gain Amplifier

PSA - Parts storage Area

PT - Pulse Tube

ROI - Region Of Interest

TES - Transition Edge Sensors

TSP - Tower Support Plate

1 Executive Summary

The study of neutrinoless double beta decay ($0\nu\beta\beta$) is one of the most sensitive low-energy searches for new physics [1]. If observed, this very elusive decay would imply a lepton number violation by two units and would prove the existence of massive Majorana neutrinos [1–3]. The decay produces a monochromatic peak in the kinetic energy sum spectrum of the two emitted electrons. The only necessary and sufficient signature used to distinguish the $0\nu\beta\beta$ decay from peaks produced by other processes (e.g. the full energy peaks due to environmental gamma lines) is its position at the $0\nu\beta\beta$ transition energy. Excellent energy resolution, large detector masses, and very small backgrounds are of paramount importance for the discovery potential of any experiment.

Significant experimental efforts in recent years have improved the $0\nu\beta\beta$ sensitivity in several isotopes, and with a variety of detection techniques [4, 5]. The race towards discovery is characterized by the increase in the experimental mass, which has led to the construction of ton-scale detectors. With the increase in mass has also come the difficult but steady progress in removing the spurious background events that can jeopardize the observation of a $0\nu\beta\beta$ decay. Background reduction presents the hardest challenge. This has led to the development of improved detection techniques and to the study of different $0\nu\beta\beta$ candidate nuclei. It has also driven the painstaking process of improving the radiopurity of the detector components.

Recent advances in operating large sensitive detectors have undoubtedly proven that cryogenic particle detectors (often called bolometers) are among the most attractive devices for the construction of a large, sensitive $0\nu\beta\beta$ experiment. The bolometric detectors are characterized by excellent energy resolution, which suppresses the irreducible background from the Standard Model process of two-neutrino double beta decay ($2\nu\beta\beta$). Moreover, good energy resolution largely reduces the risk of misidentifying a background peak for the $0\nu\beta\beta$ one. Large detectors can be operated reliably, with low backgrounds. Bolometric detectors are scalable, allowing gradual, phased deployment. Finally, these detectors have a unique feature of allo deployment of different double-beta decay isotopes in the same infrastructure. This true multi-isotope approach may prove invaluable in case of a discovery.

Over the last decade, bolometers have demonstrated excellent operational characteristics (detector mass, resolution, reproducibility, and background level). TeO_2-based bolometric detectors such as CUORE-0 [6] and CUORE [7] have produced world-leading $0\nu\beta\beta$ results. Moreover, bolometers containing different $\beta\beta$ candidates such as ^{82}Se, ^{100}Mo, and ^{116}Cd performed equally well in dedicated tests [8–14]. Most recently, CUPID-0 [15, 16] at Laboratori Nazionali del Gran Sasso (LNGS) and CUPID-Mo [17] at Laboratoire Souterrain de Modane (LSM) demonstrated that it is possible to improve the detector background using active background rejection techniques that are considered a fundamental requirement for any next generation experiment.

CUORE is the largest $0\nu\beta\beta$ detector of its kind and is the reference point for any future bolometric $0\nu\beta\beta$ experiment. With a large cryostat able to cool a one-ton detector to temperatures below 10 mK [18, 19] and its specially designed infrastructure ensuring a low-noise and low-radioactivity environment for its 988 crystal bolometric array, CUORE is searching for $0\nu\beta\beta$ in ^{130}Te with unprecedented sensitivity. CUORE is currently one of the most competitive $0\nu\beta\beta$ experiments in operation. If $0\nu\beta\beta$ is not found at its sensitivity scale, CUORE will provide fundamental information for the next steps in this field.

A further increase in the experimental sensitivity will require the implementation of new ideas and new technical solutions able to surpass CUORE limits. At the same time, the significant investment required to realize CUORE and the success of its cryogenic and scientific operations motivates ongoing efforts towards defining the next-generation experiment based on the same infrastructure and know-how developed within CUORE. A path forward that introduces new technology capable of reducing the backgrounds by at least two orders of magnitude while deploying up to a ton of the isotope of interest in a few timely phases is both scientifically motivated and plausible.

In this document we discuss a well-defined strategy that, starting from the present experimental configuration of CUORE, looks toward a future experiment characterized by a substantial improvement in $0\nu\beta\beta$ discovery sensitivity. CUPID (CUORE Upgrade with Particle IDentification) starts from the CUORE [7] technical expertise, material selection, background model, and excellent energy resolution, and combines it with the capability to eliminate the backgrounds from α particles using scintillating crystal [13, 15, 16]. In addition, the high Q-value of $0\nu\beta\beta$ in ^{100}Mo naturally suppresses the gamma backgrounds by over an order of magnitude, compared to CUORE. We demonstrate that the scintillating bolometer technology based on Li_2MoO_4 crystals highly enriched in ^{100}Mo is scalable to ton-scale isotopic masses. An experiment deployed in the existing CUORE cryostat would have a discovery potential covering the entire inverted hierarchy region of neutrino masses. An expansion to a metric ton of ^{100}Mo

in a larger cryostat would enable an experiment with the normal hierarchy sensitivity.

We discuss strategies for deploying CUPID after the end of the CUORE scientific operations in a way that delivers results in a timely manner, and maintains scientific leadership in $0\nu\beta\beta$ searches over the next decade.

The baseline design of the CUPID detector to be deployed in the CUORE cryostat is conservative and its sensitivity is based on mature data-driven background model. Such a detector could be ready for construction as early as 2021, when the technical design is finalized. For reference, we list here the main parameters of the CUPID detector in Table 1. The CUPID discovery and exclusion sensitivity as a function of livetime are depicted in Fig. 1.

Table 1: Main parameters of the conservative baseline CUPID detector design.

Parameter	Baseline
Crystal	Li_2MoO_4
Crystal size	⌀50 mm× h50 mm
Crystal mass (g)	308
Number of crystals	1534
Number of light detectors	1652
Detector mass (kg)	472
^{100}Mo mass (kg)	253
Energy resolution FWHM (keV)	5
Background index (counts/(keV·kg·yr))	10^{-4}
Containment efficiency	79%
Selection efficiency	90%
Livetime	10 years
Half-life limit sensitivity (90%) C.L.	1.5×10^{27} y
Half-life discovery sensitivity (3σ)	1.1×10^{27} y
$m_{\beta\beta}$ limit sensitivity (90%) C.L.	$10 - 17$ meV
$m_{\beta\beta}$ discovery sensitivity (3σ)	$12 - 20$ meV

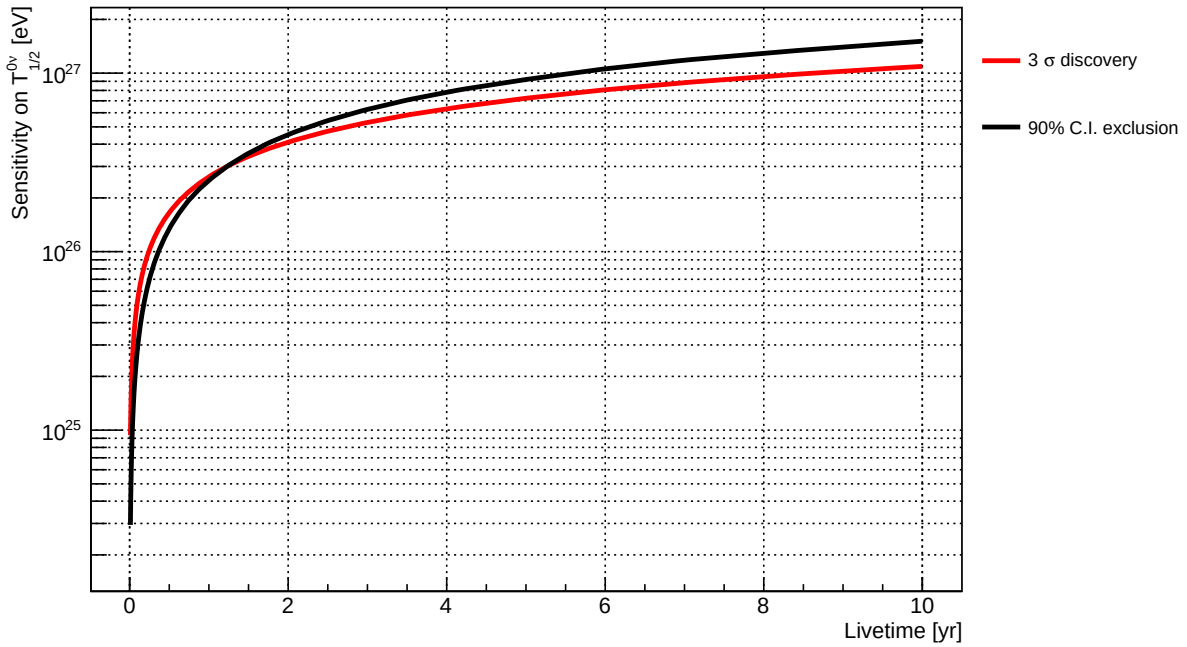


Figure 1: CUPID sensitivity curves as a function of the experiment livetime. The red curves correspond to the 3 σ discovery sensitivity, the black one to the 90% C.I. Bayesian exclusion sensitivity.

2 Motivations

2.1 Lepton number violation and neutrinoless double beta decay

Double beta decay is the rarest observed nuclear transition. It is a weak process that takes place between two even-even isobars when the decay to the intermediate nucleus is energetically forbidden due to the pairing interaction and is possible for 35 nuclei. The $2\nu\beta\beta$ decay — a second order weak transition — conserves the lepton number and was detected in eleven nuclei with half-lives in the range 10^{18} – 10^{21} yr. The neutrinoless process, corresponding to $(A, Z) \rightarrow (A, Z + 2) + 2e^-$, may be induced by a number of mechanisms beyond the Standard Model.

The detection of $0\nu\beta\beta$ decay would be a major breakthrough [1–3], proving that neutrino, unlike all the other fermions, is a Majorana rather than a Dirac particle: the neutrino would be the only spin-$\frac{1}{2}$ particle coinciding with its own antimatter partner, a possibility naturally set by its neutrality. In this context, a new mechanism of mass generation, besides the Higgs mechanism, could occur and naturally explain the smallness of light-neutrino masses. In addition, the matter-antimatter asymmetry in the Universe could be accounted for by CP violation in the neutrino sector. In spite of these major implications on neutrinos, we remark however that $0\nu\beta\beta$ decay is much more than a neutrino physics experiment. It is a powerful, inclusive test of lepton number violation, which creates electrons according to the process $2n \rightarrow 2p + 2e^-$, implemented in the nuclear matter. From a beyond-Standard-Model perspective, lepton number violation is as important as baryon number violation. Therefore, the experimental search for $0\nu\beta\beta$ decay must be pursued with the highest possible sensitivity, regardless of the related neutrino-physics scenario.

In spite of the richness of the physics connected to $0\nu\beta\beta$ decay (Sec. 9), the so-called mass mechanism, which represents a minimal extension of the Standard Model, is particularly important. In this scenario, the virtual particles mediating $0\nu\beta\beta$ decay are the three massive light neutrinos observed so far and which undergo flavor oscillations. The mass mechanism neatly relates the $0\nu\beta\beta$ decay rate to the mixing angles and mass splittings of the three known neutrinos (partially accessible through other searches), sets well-defined experimental targets, and provides a metric that allows us to compare the current results and the future sensitivities of experiments studying different isotopes and adopting different technical approaches.

The parameters involved in the mass mechanism appear in Eqs. (2) and (3) of Sec. 9, where they are related to the main output of the experimental searches consisting of the constrained (or measured, if $0\nu\beta\beta$ decay is detected) half-life $T^{0\nu}_{1/2}$. These parameters are the phase space $G_{0\nu}$, the axial vector coupling constant g_A, the nuclear matrix element $\mathcal{M}$ relevant for the light-neutrino exchange, and the effective Majorana mass $m_{\beta\beta}$ defined in Eq. (3) of Sec. 9, which contains the neutrino-physics information delivered by $0\nu\beta\beta$ decay investigation. The experimental results in terms of $T^{0\nu}_{1/2}$ can be translated to bounds (or values) for $m_{\beta\beta}$, exploiting the knowledge about $G_{0\nu}$, $\mathcal{M}$ and g_A. While $G_{0\nu}$ is exactly calculable, $\mathcal{M}$ is known to within a factor 2–3 depending on the nuclear model. The value of g_A is usually taken as 1.25, close to that measured for the free neutron. However, values much lower than that, even by a factor 2, have been proposed. This g_A quenching would have a dramatically negative impact on the rate prediction, and is under extensive examination and discussion in the theoretical nuclear physics community.

In this introduction, we will use the sensitivity to $m_{\beta\beta}$, which spans an interval of values due to the uncertainties on $\mathcal{M}$, as a metric to present the state-of-the-art of the field. It will also be used to describe future scenarios and the role CUPID plays in these developments, as depicted in Fig. 2. A thorough discussion is carried out in Sec. 9.

2.2 Isotope selection and summary of the current searches

The $0\nu\beta\beta$ decay signal is a distinctive monochromatic peak in the sum-energy spectrum of the two emitted electrons at the Q-value ($Q_{\beta\beta}$) of the reaction. Given the long expected lifetime ($> 10^{25-26}$ y), the $0\nu\beta\beta$ decay search requires large sources, containing tons of the isotope of interest. Required detector characteristics are high energy resolution, high efficiency, and low background [4, 5]. High $Q_{\beta\beta}$ values are a crucial advantage, as this feature positively affects both the phase space $G_{0\nu}$ and the background level. As a consequence, at the moment only nine isotopes are experimentally relevant thanks to their large $Q_{\beta\beta}$ (see Fig. 3). Two energy markers are especially relevant for the expected background [5]: the 2615 keV marker, representing the end-point of the γ radioactivity, and the 3270 keV marker, corresponding to the β decay Q-value of ^{214}Bi, which belongs to the radon (^{222}Rn) progeny.

A first group of three candidate $0\nu\beta\beta$ isotopes (^{76}Ge, ^{130}Te, and ^{136}Xe) features $Q_{\beta\beta}$s above 2 MeV but below both markers, and therefore have to cope with the natural γ background and with the radon-

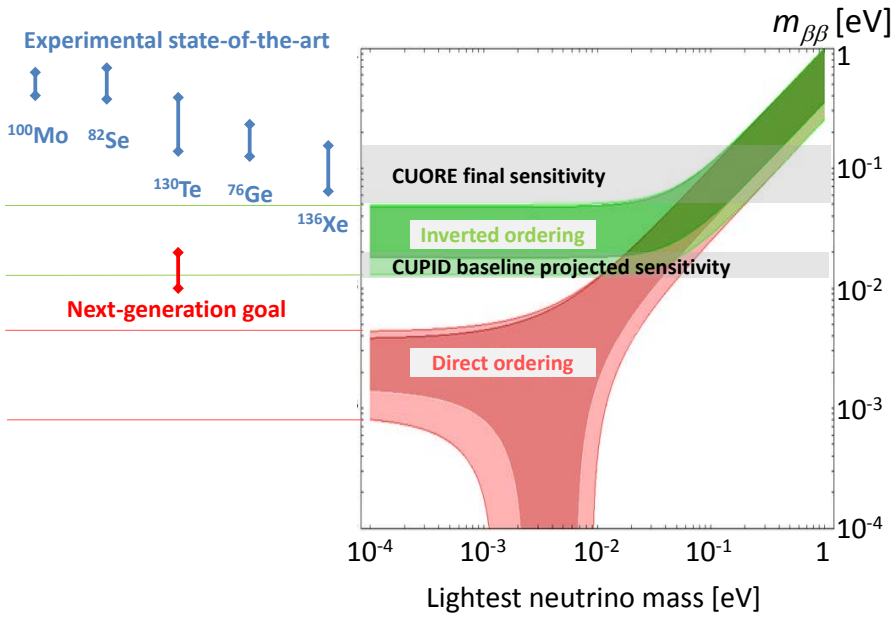


Figure 2: The effective Majorana mass $m_{\beta\beta}$ as a function of the lightest neutrino mass provides the parameter space typically used to compare $0\nu\beta\beta$ decay experiments. The experimental state-of-the art and the goal of next-generation experiments are shown on the left. The final sensitivity of CUORE and the projected sensitivity of CUPID baseline are also reported.

induced one. However, superb detection technologies can be employed for these nuclei: germanium diodes (GERDA [20] and MAJORANA [21]), xenon gaseous and liquid detectors (EXO-200 [22], NEXT [23], and other projects), large liquid-scintillator volumes incorporating the candidate nuclei (KamLAND-Zen [24] and SNO+ [25]), and TeO_2 bolometers (CUORE [7]). Thus, it is not surprising that the currently most sensitive experiments study these three nuclei (^{136}Xe in KamLAND-Zen, ^{76}Ge in GERDA and ^{130}Te in CUORE), with limits on $m_{\beta\beta}$ of 61–165 meV [24], 120–260 meV [20], and 110–520 meV [7] respectively. The current results barely approach the onset of the inverted ordering (IO) region of the neutrino mass pattern, which extends in the range 15–50 meV for a vanishing lightest-neutrino mass. These experiments, even at the completion of their experimental program, are far from fully exploring this region. In addition to these three ongoing projects, there are other searches based on one of the same isotopes that are under commissioning or fully funded, or will take data soon. In this context, we will mention: SNO+ [25], which will study ^{130}Te dissolved in liquid scintillator in the SNO set-up; LEGEND-200 [26], based on the GERDA and MAJORANA experiences and exploiting at maximum the current GERDA set-up for the study of ^{76}Ge; and NEXT-100 [23], a high pressure electro-luminescence TPC studying ^{136}Xe. Even these experiments, however, do not have the sensitivity required to cover the IO band.

Continuing our survey of the most promising isotopes, we remark that the three candidates ^{48}Ca, ^{96}Zr, and ^{150}Nd are in the best position to carry out a background-free experiment, since their $Q_{\beta\beta}$s are higher than the ^{214}Bi β endpoint and therefore are not affected by γ radioactivity. Unfortunately, these are currently ruled out as being part of a viable and competitive experiment because they have a very low isotopic abundance; at this time, large-scale enrichment is impossible or prohibitively expensive.

The remaining three candidate isotopes (^{82}Se, ^{100}Mo, and ^{116}Cd) feature an expected $0\nu\beta\beta$ decay signal out of the bulk of the γ environmental background, but radon-related contamination may still be influential. These nuclei can be embedded in a number of compounds that allow the growth of large scintillating crystals. Radon radioactivity is not a severe issue in this case because the active part of the detector is not a fluid that can be contaminated by gaseous radon emanation. This technology is currently applied to ^{82}Se in CUPID-0 [15, 16] and to ^{100}Mo in both CUPID-Mo [27] and AMoRE [28]. In scintillating bolometers, each event provides a thermal and a scintillation signal. Their simultaneous detection enables the discrimination of α particles, which present a generally lower light yield than that of β particles of the same energy [29]. Another possibility is to perform pulse-shape discrimination in the scintillation signal [30] and for some crystal events in the thermal signal [31]. These methods can reject energy-degraded surface αs, which are expected to be the dominant background source above 2.6 MeV. CUPID will follow this experimental approach, as discussed in detail in Sec. 2.4.

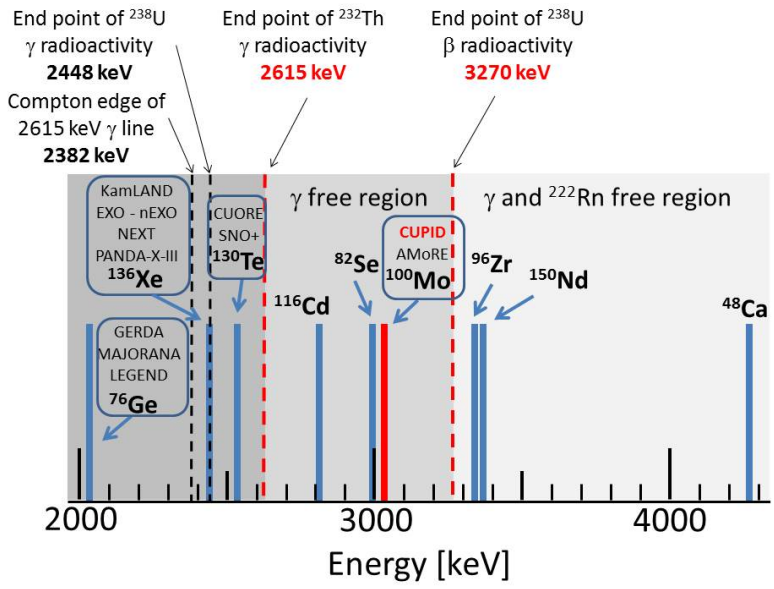


Figure 3: The positions of the expected signals in a two-electron sum-energy spectrum for the nine most favorable $0\nu\beta\beta$ decay isotopes. These are compared with background energy markers related to the maximum γ energies of the ^{238}U and ^{232}Th chains and the maximum β energy of the ^{238}U chain. The main experiments are also mentioned in relation with their selected nucleus. For essentially technical reasons, most searches investigate the three least favorable isotopes. The isotope selected for the CUPID baseline is ^{100}Mo, while ^{130}Te is an alternative option.

2.3 Proposed next-generation searches

As already mentioned, the current objective of the experimental search for $0\nu\beta\beta$ decay is to explore deep into the IO region. Some of the proposed next-generation projects can in principle fully cover the allowed IO region and detect $0\nu\beta\beta$ decay even in case of direct ordering, provided that the lightest neutrino mass is larger than 10 meV. This is the main physics goal of CUPID.

We will briefly discuss here the main next-generation projects [32]. A quantitative analysis of their physics reach, in comparison with CUPID, is presented in Sec. 9 and graphically in Fig. 47.

Future projects can be broadly classified into two categories: experiments using a fluid-embedded $0\nu\beta\beta$ source (featuring large, sensitive masses and easy scalability) and experiments using a crystal-embedded $0\nu\beta\beta$ source (featuring high energy resolution and efficiency). In the first class we have Xe-based TPC projects like nEXO (evolution of the closed EXO-200), NEXT-1.5t (evolution of the imminent NEXT-100), and Panda-X-III [33]. This also includes experiments which dissolve the source in a large liquid-scintillator matrix exploiting existing infrastructures like KamLAND2-Zen (evolution of the current KamLAND-Zen-800) and SNO+-phase-II (evolution of the imminent SNO+-phase-I). In the second class we have experiments based on germanium diodes like LEGEND-1t (evolution of the planned LEGEND-200) and those which exploit the bolometric technique, like the multi-step AMoRE program (AMoRE-I and AMoRE-II, which represent the evolution of the current AMoRE pilot), and finally CUPID, which is based on the large experience gathered by CUORE and the demonstrators CUPID-Mo and CUPID-0. The most prominent projects in this rich scenario are nEXO, LEGEND-1t, NEXT-1.5t, and CUPID, which have a 3 σ discovery sensitivity that, at least for some matrix element calculations, reaches below 20 meV for $m_{\beta\beta}$ (see Fig. 47).

2.4 CUPID: the next-generation bolometric search for $0\nu\beta\beta$ decay

Bolometers are ideal detectors to perform sensitive $0\nu\beta\beta$ searches [29, 34, 35]. They can provide an energy resolution at the few per-mil level, a total efficiency at the 70%–90% level, and extremely low background thanks to the high radiopurity achievable in the crystals used as detectors [36]. Moreover, several high-$Q_{\beta\beta}$ candidates (^{48}Ca, ^{76}Ge, ^{82}Se, ^{100}Mo, ^{116}Cd, and ^{130}Te) can be studied with the same cryogenic apparatus.

The active part of a bolometer consists of a crystal coupled to a thermal sensor, which converts temperature variations into a voltage or current pulse, depending on the sensor technology. The typical masses for crystals used in $0\nu\beta\beta$ decay search are in the 0.1–1 kg range. Bolometers of this size must be operated at very low temperatures (< 20 mK) so that the crystal heat capacity is low enough to provide high-amplitude signals for energy depositions in the range of interest (∼MeV-scale for $0\nu\beta\beta$ decay). In the CUPID baseline, the thermal sensor will be a Neutron Transmutation Doped (NTD) Ge thermistor, already adopted in Cuoricino, CUORE, CUPID-0, and CUPID-Mo. NTDs are mainly sensitive to thermal phonons and essentially act as a thermometer (see Sec. 5.1 for further details).

The environmental γ flux represents one of the main sources of background for most of the present experiments. As mentioned above, the highest energy-relevant γ line in natural radioactivity is the 2615 keV full-energy peak of ^{208}Tl, belonging to the ^{232}Th decay chain. The energy region above $\sim$ 2.5 MeV is dominated by α events induced by surface radioactive contaminants, as shown by the results of Cuoricino, CUORE-0, and CUORE [37]. Exploiting the luminescence of some detector materials, it is possible to distinguish between α events and signal-like events. As the light yield for energy depositions induced by α and β particles of the same energy is different, the simultaneous detection of light and heat, and the comparison of the respective signal amplitudes, leads to an effective rejection of the α background (Fig. 4). This approach was extensively studied and proved successful in many independent demonstrator experiments [29, 35, 38], and is the method chosen for CUPID. Particle IDentification (PID) is only possible with the installation of a light detector, which in the CUPID design is also a bolometer facing the main crystal (Sec. 5). Medium-scale demonstrators like CUPID-0 [15, 30] and CUPID-Mo [17, 27], involving tens of scintillating bolometers, show that this technique is viable, robust and reproducible.

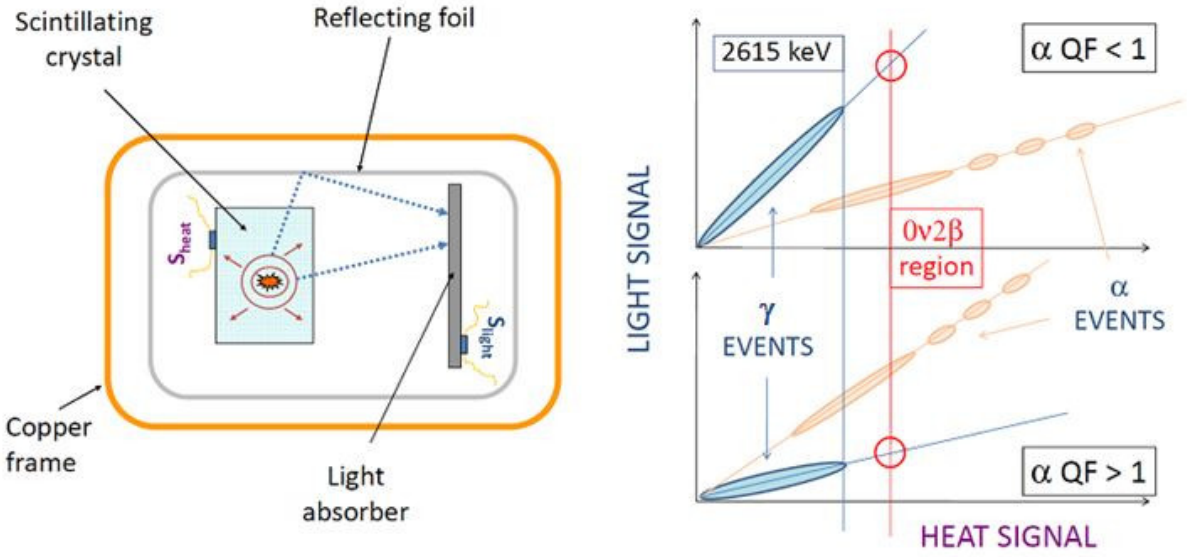


Figure 4: Left: the main elements of a scintillating bolometer consist of two phonon sensors. The heat signal is read from the crystal containing the $0\nu\beta\beta$ candidate, and the light signal from the optical bolometer collecting the scintillation light. Right: concept of αparticle rejection exploiting the simultaneous measurement of heat and light for the same event. Top-right: the common situation where αs produce less scintillation light than βs and have a Quenching Factor (QF) < 1. This is an example case of Li_2MoO_4 and $CdWO_4$ crystals. Bottom-right: the opposite case with QF > 1. The only crystal known to follow this behavior is ZnSe.

The material selection for the CUPID crystals is based on the extensive experience collected by the previous projects MIBETA, Cuoricino, CUORE, BOLUX, LUCIFER, ISOTTA, and LUMINEU. The copious results achieved so far on more than 10 compounds, joined with the preliminary results from the CUORE background model (Sec. 7), indicate that the optimal choice for CUPID is lithium molybdate (Li_2MoO_4) [12, 39], containing the candidate ^{100}Mo with $Q_{\beta\beta}$= 3034 keV (Fig. 3). Section 4 describes the enrichment, the purification, and the crystallization methods allowing the development of $Li_2{}^{100}MoO_4$ crystals with the required features. The Li_2MoO_4 light yield is compatible with the desired α-background rejection, while the demonstrated radiopurity of the crystals, which are grown from enriched materials, satisfies the CUPID requirements.

In its baseline design, CUPID will consist of an array of 1534 Li_2MoO_4 crystals, grown from molybdenum enriched at $\geq 95\%$ in ^{100}Mo. The single-crystal mass will be approximately 308 g, corresponding to a total ^{100}Mo mass of about 253 kg. CUPID will be housed in the present cryogenic facility of CUORE, located in the Laboratori Nazionali del Gran Sasso of INFN, Italy, and will benefit from its infrastructure and operation procedures (see Sec. 3). The expected background index (BI) is about 10^{-4} counts/(keV·kg·yr) in the ^{100}Mo region of interest (ROI) (see Sec. 7). These parameters will allow CUPID to fully explore the IO region of the effective Majorana neutrino mass (see Fig. 2) and to

have a high discovery potential if the lightest neutrino mass is larger than 10 meV, regardless of the neutrino-mass ordering. For a detailed discussion on CUPID sensitivity and physics reach, see Sec. 9 and Fig. 47.

One of the aforementioned advantages of the bolometric technology is its possible application to several favorable candidates. Competitive experiments can be performed using crystals of ZnSe (candidate ^{82}Se), Li_2MoO_4 (candidate ^{100}Mo), $CdWO_4$ (candidate ^{116}Cd), and TeO_2 (candidate ^{130}Te). These multiple searches can be performed just changing the crystals and keeping the same detector configuration, assembly procedures, cryogenic infrastructure, readout electronics, data-acquisition system, and analysis tools [38, 40].

The CUORE background model clearly shows the current superiority of the ^{100}Mo option, essentially because of its favorable $Q_{\beta\beta}$ (see Fig. 3). However, ^{130}Te embedded in TeO_2 crystals is maintained as a possible alternative. The ^{130}Te option is motivated by the excellent technical performance of the TeO_2 bolometers, whose fabrication and operation were successfully tested on hundreds of elements [7, 41], and by the uniquely high natural isotopic abundance of ^{130}Te (34%), which makes its enrichment especially affordable. The PID in TeO_2 requires an outstanding optical bolometer capable of detecting the feeble Cherenkov light emitted by a $0\nu\beta\beta$ decay event [42], which is an order of magnitude lower than the scintillation light from Li_2MoO_4. The related light-detector technology is discussed in Sec. 5, while the overall tellurium option is presented in Sec. 10.

3 Overview of the experiment

3.1 CUPID detector concept

In CUPID, the main bolometer crystals will be grown from $Li_2{}^{100}MoO_4$. The Mo component will be enriched to $\geq 95\%$ in ^{100}Mo. At this stage of the conceptual design, we envision the use of cylindrical crystals with 50 mm diameter and 50 mm height, corresponding to a mass of ~ 308 g. We selected such a mass so that pile-up of ^{100}Mo ordinary $2\nu\beta\beta$ decay events in a single crystal will contribute to background in the ROI at a level compatible with the CUPID target BI of 10^{-4} counts/(keV·kg·yr) (see Section 7.1.2).

As in CUORE, a NTD Ge thermistor will be glued to the crystal on a flat surface, in order to provide the thermal signal. In the baseline design, the curved surface of each crystal are surrounded by a light-reflecting foil to maximize light collection, and the flat surfaces of the crystals are exposed to bolometric light detectors fabricated from Ge wafers with 5 cm diameter. The Ge wafers are also instrumented with an NTD as a thermal detector. The structure of a single CUPID scintillating bolometer is shown in Fig. 5. The crystals and the light-detector wafers are supported by PTFE elements connecting them to round copper frames. These frames are stacked by means of copper columns, forming a detector tower conceptually similar to those of CUPID-0 and CUPID-Mo. Light detectors are placed between successive crystals, thus each light detector will serve two crystals at the same time. With this design, we anticipate 1534 crystals in the full array, corresponding to about 253 kg of ^{100}Mo. Fig. 44 of Section 7.4 shows the CUPID array hosted inside the CUORE cryostat. The basic unit geometry is a cylindrical main bolometer with reflective foil and Ge light detector disc. This has been used with great success in CUPID-0 [30] (see Fig. 5, right panel) and CUPID-Mo [17]. The array will be operated at 10-20 mK.

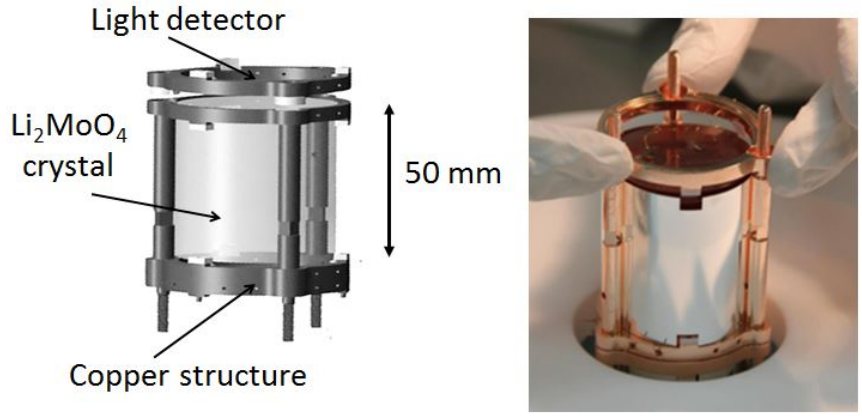


Figure 5: Left: schematic view of the CUPID single module according to the baseline design. Right: photo of a CUPID-0 scintillating bolometer, prefiguring the CUPID single-module structure. The reflective foil surrounding the crystal is visible.

In the rest of this section, we describe the results achieved in CUPID-Mo and its preparation measurements. CUPID-Mo is placed in the context of the LUMINEU project [17, 27, 39], which shows the maturity reached by the proposed technology and the high standard of the Li_2MoO_4 detectors in terms of energy resolution, α/β rejection capabilities, internal radiopurity, and overall reproducibility of the results. The single module of CUPID-Mo consists of a crystal of $Li_2{}^{100}MoO_4$ enriched at more than $\sim 96\%$ in ^{100}Mo. The crystals are cylinders with 44 mm diameter and 45 mm height coupled to NTD Ge thermistors. At least one of the flat surfaces of each crystal is exposed to a light detector, consisting of an NTD-instrumented Ge wafer with a diameter of 44 mm and coated with a 70-nm-thick SiO layer on both sides to maximize light absorption. In the tests preceding CUPID-Mo, we operated modules with and without reflecting foils, achieving a satisfactory α/β separation in both cases. In CUPID-Mo, we opted for a conservative approach and used the reflective foil in all the 20 modules installed. The results achieved in the tests preceding CUPID-Mo and confirmed by CUPID-Mo itself are summarized below:

- We routinely obtained energy resolutions of ~ 5 keV FWHM at 2615 keV.
- The heat-light readout yields an α rejection at the level of 99.9% with nearly full acceptance of the β and γ events.
- The strict crystal production protocol guarantees internal contamination $\lesssim 5$ μBq/kg for both ^{232}Th and ^{238}U, and $\lesssim 5$ mBq/kg for ^{40}K.
- The heat channel features rise-times (from 10% to 90% of the signal maximum) of $\sim$ 15–30 ms and decay-times (from 90% to 30% of the signal maximum) of $\sim$ 100–500 ms, depending on the detector and on the operation temperature.

The size of the main crystal and of the light detector, their mechanical and geometrical arrangements, and the readout approach adopted in both these tests and in CUPID-Mo closely resemble the baseline solution proposed for CUPID. Hence, we expect very similar performances for both the heat and the light detectors.

An alternative option will be considered for the crystal shape and size. We will investigate the possibility of operating cubic $Li_2{}^{100}MoO_4$ crystals with a side of 45 mm, corresponding to a mass of ~ 280 g. This geometry allows to arrange the crystals in tightly-packed towers with 4 crystals per floor, as in Cuoricino, CUORE-0, and CUORE. In this design, the amount of passive material between crystals is minimized, substantially increasing the possibility of suppressing surface background by anti-coincidence. This is of special importance for the β component that cannot be rejected by α discrimination. Such a configuration would allow to eliminate the scintillating foil and operate the crystals in a fully open structure. Dedicated tests will be required to check that α/β separation maintains a high enough efficiency in spite of the reduced light collection efficiency.

3.2 Infrastructure introduction

CUPID will benefit significantly from the existing infrastructure developed for CUORE. This includes: the unique CUORE cryogenic system, capable of cooling ∼1000 kg payloads < 10 mK temperatures; internal (cryogenic) and external (room temperature) calibration systems; underground cleanrooms for detector assembly and parts storage; a mature detector assembly line; dedicated R&D dilution refrigerators both underground and on the surface for testing components; and well-established procedures and facilities for the surface-cleaning of detector parts. In the following sections, we describe the existing infrastructure in detail and provide a conceptual overview of the upgrades envisioned for CUPID.

3.3 Cryogenics

3.3.1 The CUORE cryostat

Figure 6 shows a schematic of the CUORE cryostat [19] consisting of six nested vessels, with the innermost containing the experimental volume of about 1 m^3. The different stages are at decreasing temperatures of about 300 K, 40 K, 4 K, 800 mK (also called the still), 50 mK (HEat Exchanger, HEX), and 10 mK (Mixing Chamber, MC). The 300 K and the 4 K vessels are vacuum-tight and are called the outer vacuum chamber (OVC) and inner vacuum chamber (IVC), respectively. Inside the inner vacuum chamber, two lead shields protect the detectors from external radioactivity sources. The internal lateral lead shield stands in between the still and the HEX stage, while the top lead is positioned below the MC plate. The CUORE detector is attached to the Tower Support Plate (TSP) placed right below the top lead.

The cryostat is provided with different cooling units. The 40 K and 4 K plates are cooled down through 5 Pulse Tube refrigerators (PTs). The still, HEX, and MC plates are cooled down by a ^{3}He/^{4}He Dilution Unit (DU) integrated in the system.

A standalone structure (Fig. 6), supports and mechanically decouples the cryostat itself from the rest of the world to minimize the vibrational noise. The support structure basement consists of two reinforced concrete walls connected to its foundation through four rubber dampeners with high damping coefficients. This solution allows for an effective decoupling of the seismic structure from the ground. On top of the walls, four tubular sand-filled steel columns are installed around the perimeter. The columns in turn support the the main support platform, a grid of steel beams from which the cryostat hangs by means of three ropes connected to the 300 K plate.

The 300 K plate holds directly or indirectly all cryostat components through a cascade of dedicated bars, with three bars per plate to ensure a precise vertical alignment. In particular, the 300 K plate holds the 40 K, 4 K and still plates; the HEX plate is held by the still plate and supports in turn the MC plate. Each plate holds the corresponding vessel, which acts as thermal radiation shield. The internal lateral shield is mechanically supported by the still plate, but thermalized to the 4 K one, while the top lead directly hangs from the 300 K plate and is thermalized to the HEX plate. The TSP support is similar to that of the top lead. However, the former is mechanically decoupled from the cryostat and is held by a Y-beam which lies on three vibration isolators directly anchored to the main support platform. The cryostat is located inside a cleanroom, while the Y-beam is placed in a Faraday room hosting the readout electronics (Fig. 7).

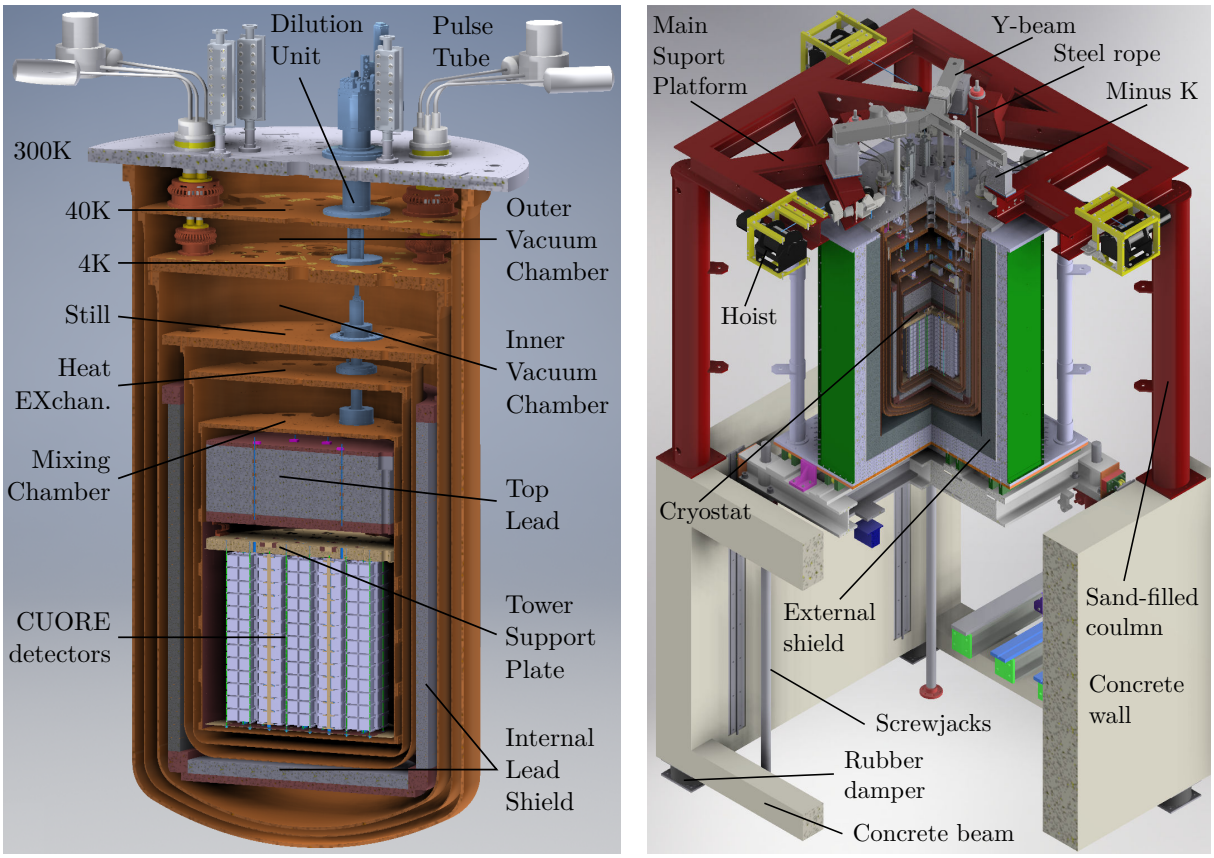


Figure 6: Left: the CUORE cryostat with the different thermal stages, the vacuum chambers, the cooling elements, the lead shields, and the detector indicated. Right: rendering of the cryostat support structure. The external shield sits on a movable platform that can be lifted to surround the cryostat during the detector operation. When raised, the external shield is at the level of the cryostat cleanroom.

3.3.2 Low-vibration environment

The CUORE cryostat must provide low-noise environment suitable for a bolometric detector. Noise abatement had to be extensively considered from the early design down to the commissioning phases. The first step in this direction was to cope with mechanical vibrations, which generate power by means of micro-friction. When this power is dissipated on the coldest stages, it can prevent the experimental stage from reaching a stable operating temperature. The impact on the bolometers is even more severe. Namely, the crystals are weakly coupled to the cooling unit and are more sensitive to temperature changes. Even when the effect is not relevant for temperature stabilization, vibrational noise still contributes to the overall noise and directly impacts the energy resolution of the detectors.

We adopted different solutions in order to mitigate the problem, protecting the detector from any vibration source. On one hand, the entire cryostat support structure is intended for decoupling the system from the surrounding environment. On the other hand, the PTs themselves are a large source of vibrations, hence we installed a series of devices to dissipate a significant fraction of this power outside the cryostat.

In particular, the choice for a remote motor option for the CUORE PTs, with the rotating valve separated from the PT head, reduces the amount of transmitted vibrations and allows us to separate the valve grounding from the main one, electrically decoupling the PT and the cryostat from the external world. Furthermore, the PTs are not directly anchored to the cryostat plates, as depicted in Fig. 6. At the level of the 300 K plate, a polyurethane ring compensates for the horizontal displacement of the PTs due to the thermal contractions at the cold stages. Inside the cryostat, flexible thermalizations (copper braids) link the cold heads of each PT to the cryostat flanges at the 40 K and 4 K stages, therefore making a softer connection between the PTs and the cryostat plates. A substantial effort has also been made to avoid any mechanical contact between the cryostat or main support platform and all the vibrating PT elements. The rotating valves and the buffer volumes are suspended by means of bungee cords. At the same time, the combination of custom rigid and flexible high pressure lines have been routed from the

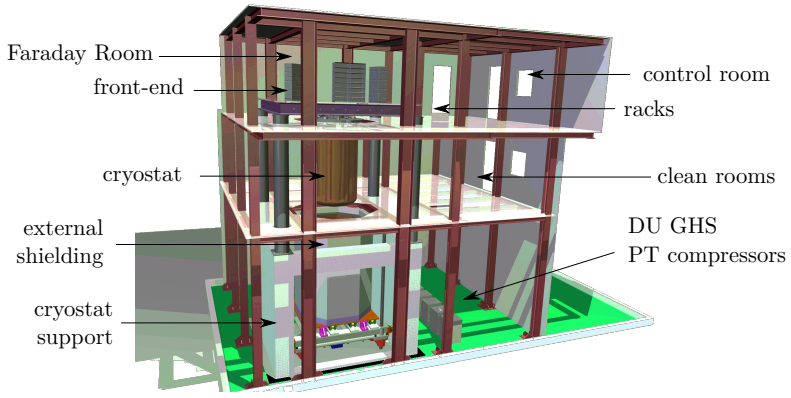


Figure 7: Rendering of the CUORE hosting building. The ground floor hosts the cryostat and shielding support structure, and most cryogenic components. The middle floor consists of 5 cleanrooms for the detector mounting and hosts the cryostat. The top floor is dedicated to the data acquisition system and to the electronics, which is located inside a Faraday room.

compressors in order to vertically drop on the rotating valves.

The PT compressors are located 15–20 m away from the 300 K plate and are supported by a metallic structure connected to the ground via elastomers. The incoming/outgoing He flexlines pass through a sandbox rigidly connected to the ground, thus absorbing a significant fraction of the generated vibrations. The flexlines are covered with neoprene to reduce acoustic noise, while at the entrance of the Faraday room the presence of ceramic electric insulators ensures that the long lines do not act like antennas.

In addition, instead of relying on the micro-stepping driver by default embedded in the compressors, the PT rotating valves in CUORE are driven by devices specifically intended to minimize the motor vibrations. These elements are fundamental to control the relative phases of the PT pressure oscillations and fix them in a configuration that minimizes the vibration transmission to the detector [43].

The CUORE detector is mechanically decoupled from the cryostat. The TSP hangs from the steel Y-beam, which is positioned on top of three Minus K vibration isolators directly anchored to the main support platform (Fig. 6). The isolators behave like soft spring when subjected to small displacements and act as a low-pass filter with a cut-off frequency of ~ 0.5 Hz.

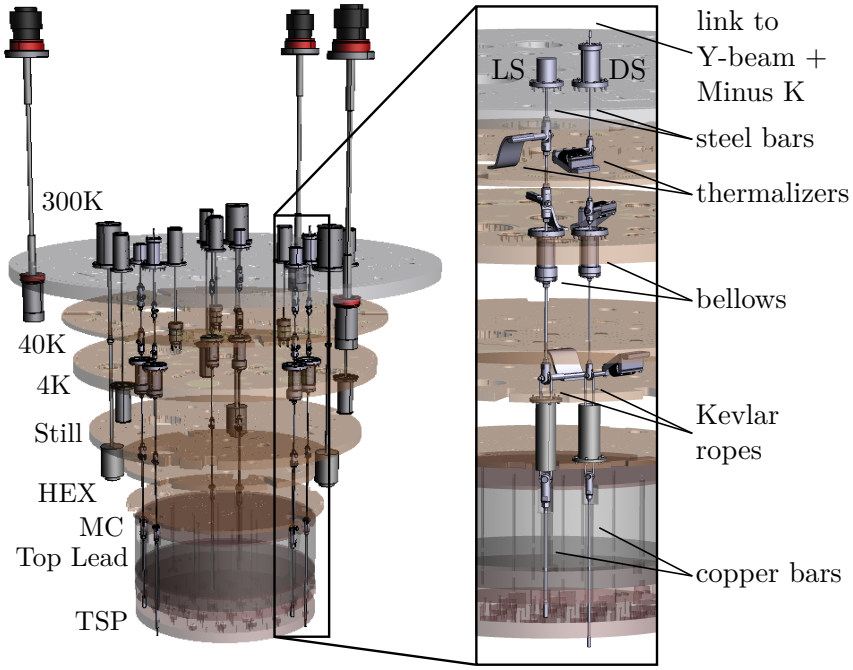


Figure 8: Rendering of the cryostat the supporting elements. The zoom shows the details of the detector and lead suspension systems.

The connection between the TSP and the Y-beam is made by means of the detector suspension system. This, as well as the top lead suspension system, consists of three composite bars (see Fig. 8). The top part, between the Y-beam (300 K plate for the lead suspension system) and the the still level, is made of segmented steel rods, which are thermalized at each thermal stage. The middle part, between the still and the MC, consists of a double Kevlar rope to minimize the heat input at the coldest stages. Finally, the lowest part is made by high purity copper rods, chosen for theirs low radioactivity content.

3.3.3 Low-radioactivity environment

The CUORE cryostat must not only satisfy the requirements related to the cryogenics, mechanics and detector performances, but also to the radioactive content of its components, resulting in a strict selection of both the materials and the production techniques. The use of copper was preferred for the largest masses, i.e. for plates and vessels, resulting in a total mass of > 6 tons. The only exception was made for the 300 K plate and the upper part of the vessel flange, which are made of austenitic stainless steel to guarantee a better mechanical stability and vacuum tightness given the huge load they sustain.

In particular, all the vessels and plates down to the HEX stage are made of Oxygen-Free Electrolytic copper, which presents a radioactive content $< 6.5{\cdot}10^{-5}$ Bq/kg and $< 5.4{\cdot}10^{-5}$ Bq/kg for ^{232}Th and ^{238}U, respectively. The MC flange and plate, the TSP, and the crystal holders are made of Cu NOSV, a special copper alloy suitable for cryogenic use produced by Aurubis. Cu NOSV features a high conductivity at low temperatures, with a residual resistance ratio > 400, a low hydrogen content, and bulk radioactivity contents even lower those of Oxygen-Free Electrolytic copper. All the copper was stored underground and extracted only for the machining operations to avoid recontamination by cosmic radiation.

The lead shielding, inserted to protect the detector from the external radiation, underwent a similar material selection process. The internal lateral shield consists of a 6 cm thick lead vessel made of radiopure lead of archaeological origin [44]. The top lead consists of five 6 cm thick disks of pure commercial lead piled and sandwiched between two copper plates. The choice for this material is less critical since the top lead is separated from the detectors by more than 9 cm of copper. High purity cooper has been used for the support parts: Oxygen-Free Electrolytic copper for the internal lateral shield rings and bottom plate, and Cu NOSV for the top lead plates.

The entire cryostat is installed inside a cleanroom (see Sec. 3.7.1). The high cleanliness standards reduced the risk of recontaminating the various parts during the commissioning phase and allowed a safe installation of the detectors. In particular the 300 K plate lies at the level of the cleanroom ceiling and separates the cleanroom environment from the standard one (see Fig. 7 for comparison).

3.3.4 Cooldown system and thermal performance

Given its extraordinary size and mass, CUORE utilizes a customly designed cryogen-free cryostat instrumented with multiple PMTs and a custom ^{3}He/^{4}He dilution refrigerator. The total mass to be cooled down is about 13.7 tons, of which 12.7 tons to below 4 K. The heat content to be extracted from the system is very large: the inner vacuum chamber enthalpy difference between room temperature (295 K) and 40 K, which represents more than 95% of the total, is $\sim 6.9 \cdot 10^8$ J. The PT cooling power is > 100 W at 300 K and quickly decreases at lower temperatures, down to < 50 W at 100 K. Moreover, PTs are designed to work at high temperatures only for short periods. Therefore, we designed and realized a dedicated apparatus, the Fast Cooling System (FCS), to reduce the cool down time by directly injecting cold He gas inside the inner vacuum chamber and forcing its circulation through a dedicated cooling circuit (see Sec 3.3.8). The FCS drives the initial phase of the cool down and is turned off when the system is at ≤ 100 K at all thermal stages. Meanwhile, the PTs are turned on. The PTs, first supporting the FCS and then alone, eventually bring the 40 K and 4 K stages to their base temperatures while the inner stages follow the 4 K one. The cool down is completed by the DU, which reaches and maintain the coldest stage temperatures, keeping a steady detector temperature of ~ 10 mK.

The CUORE cryostat utilizes five PT415-RM by Cryomech. In principle, 3 PTs would be enough to guarantee the 40 K and 4 K stage base temperatures. However, we decided to keep a spare unit in case one fails and, since an inactive PT creates a connection between the 300 K, 40 K, and 4 K stages, thus representing a thermal load for the system, we installed 2 extra PTs. We characterized the individual PTs in order to quantify the available cooling power, which is ~ 80 W and ~ 2 W at 35 K and 3.5 K, respectively, for the corresponding thermal stages and with 4 active PTs.

The CUORE DU is a high-power Joule-Thomson custom CF-3000, manufactured by Leiden Cryogenics, and is a standalone element with respect to the cryostat. As for the PTs, the DU is provided with two incoming mixture lines for redundancy, so that it is possible to continue stable operations in case one of the two lines fails. The presence of two independent condensing lines also yields a higher cooling power during cooldown, reaching flows > 8 mmol/s.

Aiming at operating the CUORE cryostat at base temperature of ~ 10 mK, we set very stringent requirements on the DU cooling power and performed several tests both at the construction site (Leiden, The Netherlands) and at LNGS. The cooling power is 2 mW at 100 mK and 4 µW at 10 mK, while stable operating temperatures of ~ 6 mK were achieved during the cryostat commissioning. The obtained values exceeded the expectations.

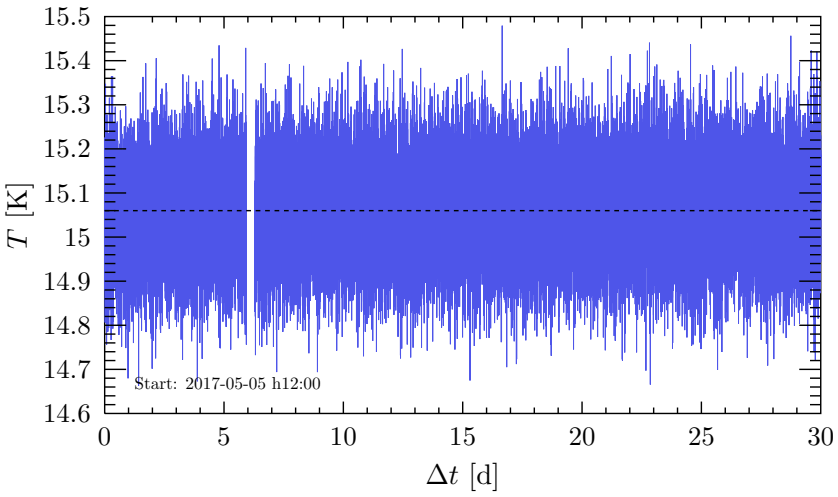


Figure 9: Base temperature stability over a thirty days period during the initial phase of the CUORE data taking. The MC temperature is 15.06 ± 0.10 mK. The dashed line indicates the average value. The gap on day 6 is due to hardware operations on the cryogenic system.

3.3.5 CUORE cooldown

The CUORE cryostat is a very complex and, despite the large masses involved, a very delicate machine. Custom design and construction were required for most of its components and numerous tests had to be performed to verify the correct functioning of the various parts. At the same time, special attention was required to ensure that any addition or modification to the apparatus did not compromise the overall performance. The commissioning of the cryogenic system proceeded by steps and involved a period of about four years. The ultimate test for the cryogenic system could only be demonstrated by the cooldown and operation of the full CUORE detector itself.

As expected, it took about 20 days in order to bring the 40 K and 4 K stages to their base temperatures. Once the DU was turned on, it took less than 4 days to reach the temperatures 0.89 K, 55 mK and 8 mK for the still, HEX, and MC stages, respectively.

An initial characterization of the detector identified 15 mK as a suitable operating temperature. We thus performed a first science run at this temperature. Fig. 9 shows the stability of the system for over one month of operation, which ultimately confirms the success of the CUORE cryogenic infrastructure.

3.3.6 Lessons learned

In the design of the CUORE cryogenic system, we considered many requirements. Building a system capable of cooling down a ton of detectors to mK temperatures in a seismically safe environment with ultra-low vibrations and radioactivity levels is an extremely complex challenge. These requirements are often in conflict, thus we gave the priority to the most critical aspects, i.e. the thermal performances of the system. As an example, we kept large safety margins in the design of the thermal conductances between the PTs and the cryostat resulting in a lower temperature of the 40 K and 4 K stages at the price of a lower mechanical decoupling between the PTs and the cryostat plates.

The CUORE cooldown has been successful and the cryogenic system performances exceeded the expectations. On the other hand, the vibration isolation of the detectors is far from optimal and we had to adopt several corrections in order to decrease the detector noise. The main sources of vibrational noise measured on the CUORE detectors turned out to be the PTs themselves, which are too strongly coupled to the cryostat structure. For this reason we introduced various modifications in the structure outside the cryostat.

With the knowledge accumulated in CUORE we can now refine the cryogenic system acting on the interior part of the cryostat and improving the vibration induced noise.

3.3.7 Upgrades for CUPID

We envision two main upgrades of the CUORE cryogenic system oriented towards the vibrational noise suppression. First, we plan to reduce the mechanical coupling between the PTs and the cryostat with two dedicated R&Ds:

– the search, design and characterization of copper conductances with high residual resistance ratio that can guarantee a comparable thermal conductivity with a lower mechanical coupling with respect to the present arrangement;

– the development of innovative heat exchangers based on gaseous helium.

The latter type of coupling is more difficult to implement in the CUORE cryostat but could bring relevant improvements. A similar idea was already developed by Cryoconcept. If successful, the gas heat exchangers could bring the possibility of running the cryostat with just 3 PTs an additional benefit.

The second planned improvement is to increase the rigidity of the cryostat internal structure. Indeed, we verified that the CUORE detectors suffer from low frequency noise generated by tiny power dissipation originated by friction of moving parts. These movements are induced by the PTs vibration. Stiffening the cryostat internal structure will limit the impact of the PTs vibrations on the detectors, keeping them at frequencies higher than the signal bandwidth.

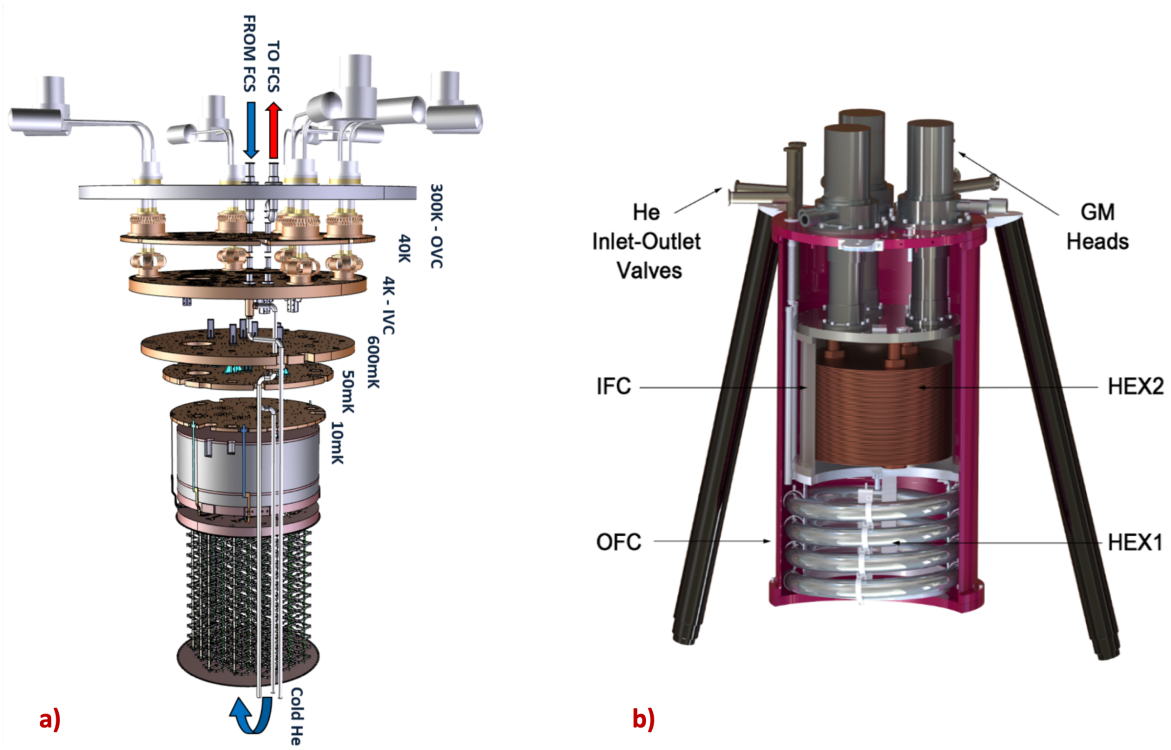


Figure 10: Helium circulation inside CUORE/ cryostat. Cold ^{4}He enters from the valve located on the top of the 300K plateand goes directly to the bottom, exchanges heat; b) Cross section view of the Fast Cooling Unit.

3.3.8 CUORE precooling stage: the Fast Cooling System

The CUORE FCS is composed of the five PT refrigerators and an external system that flows cold ^{4}He inside the IVC to improve the heat exchange, as shown in Fig. 10.a. This external system involves a Fast Cooling Unit (FCU), which is a cryostat containing two heat exchangers, a gas blower, double-walled flexible pipes, a filtering system and several other components and sensors.

Fast Cooling System Basic Parameters Constrains	Comments
$P_{IVC} < 1400$ mbar	Inner Vacuum Chamber (IVC) critical pressure
$P_{IN} > 930$ mbar	Pressures inside FCS have to exceed the atmospheric pressure ($P_{IN} > P_{ATM}$)
$P_{IN} < P_{OUT} < 1350$ mbar	When the blower is on: $P_{OUT} > P_{IN} \neq 0$
$\Delta P = P_{OUT} - P_{IN} < 400$ mbar	Limit on the pressure gradient produced by the blower
$T_{HEX2} < 202°$ K	Temperature inside the IFC has to be below the ^{222}Rn melting point
$\Delta T = T_{OUT} - T_{IN} < 40°$ K	To avoid crystals to break down, the cooling gradient must be controlled
$\Phi(^4He) < 5$ g s^{-1}	Limit on the circulating Helium flow
$\nu_{BUSCH} < 25$ Hz	BUSCH Blower frequency

Figure 11: Fast Cooling System operational parameter constrains.

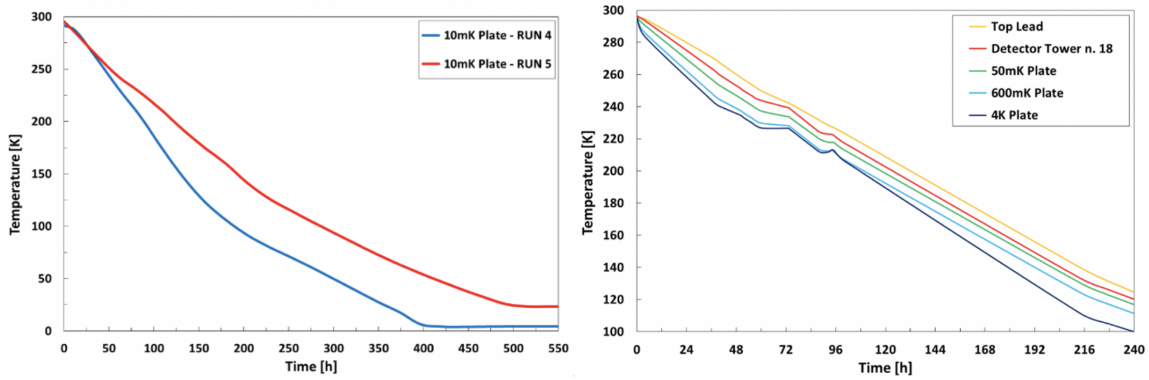


Figure 12: Left Panel – Comparison of the FCS performances on the 10 mK plate between Run 4 and Run 5 (CUORE Run 1) cooldown (see text for Run details). During the Run 5 cooldown, for technical reasons, only three out of five PTs were used to reach 25 K; the remaining PTs and the DR have been switched on later. Right Panel – Physics Run: cryostat temperature trend cooling down with the FCS.

The FCS helium circuit is designed to have two main temperature stages: stage one, upstream of the FCU, has helium gas at room temperature, where the He blower forces the gas moving; stage two, downstream of the FCU, has helium at low temperature, where the gas goes into CUORE cryostat for cooling purpose. This procedure allows us to use a normal helium blower (no cryopumps are needed for gas circulation), while the temperatures of the helium, entering the cryostat, can go down to $\sim$ 30-40 K.

The entire precooling process has several critical issues that have to be taken into account. For example, to avoid damage to the crystals, the temperature gradient needs to be $\Delta T < 40$ K and the pressures of the He gas entering ($P_{\rm out}$) or exiting ($P_{\rm in}$) from the cryostat has to be limited within a specific range ($\Delta P \equiv P_{\rm out} - P_{\rm in} < 350$ mbar). Another important aspects is that the helium flux $\Phi_{\rm He}$ cannot exceed 5 g s^{-1}. Moreover, to prevent possible ^{222}Rn radioactive contamination, the entire gas circuit pressures need to be kept above the external pressure and the He temperatures inside the heat exchanger, largely below the ^{222}Rn melting point of $\sim$ 202 K. Fig. 11 shows a list of the FCS basic parameter constrains as adopted during CUORE precooldown operations.

During the first CUORE precooldown in December 2016, the FCS successfully brought the large mass of CUORE's cryostat and crystals down to 100 K in 10 days (see Fig. 12).
A peak cooling speed value of 1.09 $\pm$ 0.02 Kh^{-1} was measured inside the IVC, while having a mean value around 0.90 $\pm$ 0.02 Kh^{-1} decreasing to 0.49 $\pm$ 0.02 Kh^{-1} at the end of the precooling process. Fig. 12 shows the results achieved during the FCS Run 4 (no detector installed, only a mini test tower) and the FCS Run 5 that correspond to CUORE Run I, the first physical run. The lower performances achieved during Run I are mainly due to three factors: for technical reasons, PT refrigerators were switched on later; only three out of five PTs were used; and interruptions were experienced during the cool down due to external factors such as blackouts.

An increase of $\sim$20-30 % of cooling efficiency and speed can be easily reached if the system runs smoothly, without too many changes in the gas circulation rate, and at least 4 of the 5 PTs are used.

3.4 The CUORE Cryogeny Monitor and Control System

The CUORE Cryogeny Monitor and Control System is an important part of the whole CUORE Slow Control System. It consists of about hundred LabVIEW based Virtual Instruments, organized in a more general expandable architecture, dedicated to monitor and control different instrumentation and related variables. It runs on a dedicated 17 slots NI PXIe located at the second floor of the CUORE hut. It acquires all the required information coming from all the different instrumentation and controls. This can be done manually or automatically for most of the vital aspects of the experiment such as the HV quality, the UPS status and performances, the water cooling complex, and all the Cryogenic equipment.

3.5 Electric demand and infrastructures

The maximum power load that LNGS can deliver to the CUORE experiments and to the associated infrastructures is $P_{\rm max}$= 162 kW. The delivered power can be shared between normal service, with power $P_{\rm NS}$, and the UPS Service with power $P_{\rm UPS}$. Without modifying the present electrical network, the

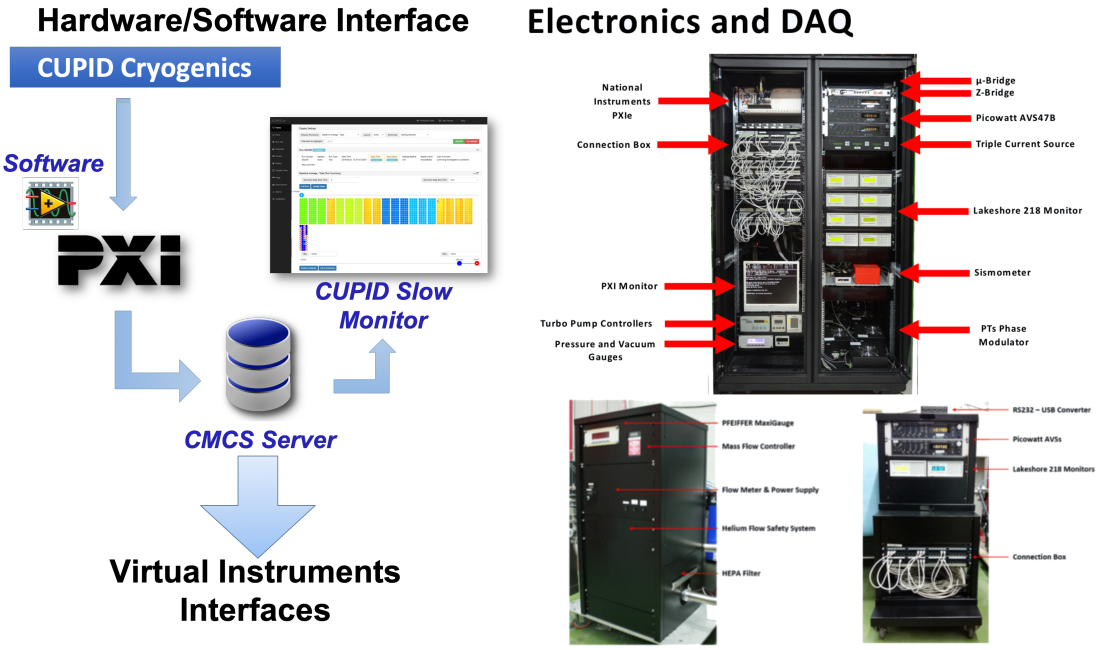


Figure 13: Left Panel – CUPID Cryogenic Monitor and Control System Hardware/Software Interface. Right Panel – Electronics and DAQ for the cryogenic system as it's at the present for CUORE Experiment.

following constrains apply: $P_{\rm NS} + P_{\rm UPS} < 162$ kW and $\rm P_{UPS} < 140$ kW. Presently, CUORE uses two UPS Systems, called UPS-1 and UPS-2. UPS-1 electrical loads are the water cooling, the PTs, the DU and related pumps, the main vacuum pumps, the backup pumps, the PLC rack, the cleanroom, and the radon abatement system. UPS-2 electrical loads are the electronics, DAQ, and all equipment located in the Faraday room. The total maximum load size, under UPS is 96 kW. The existing CUORE electric infrastructure allows us to have an extra UPS system with a maximum power load of 50 kVA (40 kW), leaving more than enough power (25 kW) for normal electric service available for other needs.

Based on a measurement performed on CUORE during standard running conditions, we measured a UPS-1 electrical peak power of $P^{\rm UPS\text{-}1}_{\rm peak} \sim 41.8$ kW ($\sim 50\% P^{\rm UPS\text{-}1}_{\rm max}$) with an average electrical power of $P^{\rm UPS\text{-}1}_{\rm AVG} \sim 17.2$ kW. Similarly, UPS-2 delivered $P^{\rm UPS\text{-}2}_{\rm peak} \sim 10.2$ kW ($\sim 50\,\% P^{\rm UPS\text{-}2}_{\rm max}$), with $P^{\rm UPS\text{-}2}_{\rm AVG} \sim 5.2$ kW. These measurements confirm that there is enough room for adding small cryogenic devices, an emergency chiller, and an extra UPS without modifying or expanding the present electric network.

3.6 Water cooling system

Each CUORE PT is connected to a water-cooled PT1010 Cryomech compressor that needs to dissipate, in water, a maximum power of 12 kW for a total 60 kW for the full PT system. Each compressor works with an average water flux of 11.5 l/min. As a comparison, the DU needs to dissipate a power of just ~ 2 kW. The present CUORE water cooling system is twofold. Under normal running conditions, the circuit that cools down all the critical components of the CUORE cryogenic system passes through a heat exchanger directly connected to the Hall A conduit of the primary laboratory water circuit.

An emergency condition state occurs when the laboratory-chilled water cannot reach the CUORE heat exchanger. In such a situation, the secondary water circuit is isolated from the laboratory primary circuit and directly connected to a small chiller (McQuay, M4AC 120 CR), located outside the Hall A. This chiller has a buffer of 300 L of cold water and can deliver 10°C water for a maximum integrated power of 40 kW. At present, only three out of five PTs, plus the DU, can be operated during an emergency condition. The size of the chiller was originally not intended to work for the CUORE cryogenic system, as it was inherited from the much smaller experiment Cuoricino. During precooling, a larger number of Cryomech compressors (7-8) run at the same time and require the dissipation of $\sim$ 90–100 kW of total heat power. We plan to double the size of the external chiller and put the chilling system under UPS to allow stable operations even when there are temporary external problems.

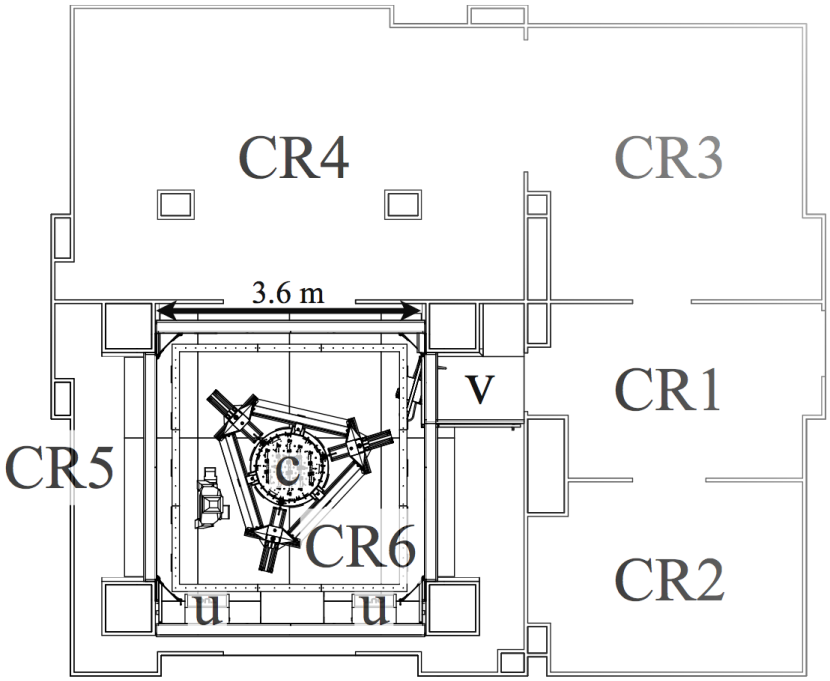


Figure 14: Map of the CUORE cleanroom. It is a class 1000 cleanroom with approximately 100 m^2 floor space divided into five sub-volumes.

3.7 Detector assembly and installation

In this section we describe the assembly procedure and facilities used for CUORE. At this stage of the conceptual design we expect many of these procedures will be similar for CUPID. We highlight lessons learned and areas which will differ and will need technical R&D to develop procedures.

The assembly process for CUORE consisted of four steps:

- gluing, i.e., fixing sensors to the crystals;
- mechanical assembly of the copper frames, crystals and CuPEN readout strips into towers;
- wirebonding, i.e., forming the electrical connection between sensors and the readout strips;
- tower closing, extraction and storage.

Each CUORE tower is composed of 13 identical floors with 4 bolometers each. These are held in position by a composite structure formed by pure copper frames providing the necessary mechanical support and PTFE holders that provide the cleanest possible contact to prevent crystal recontamination.

3.7.1 Underground cleanroom facilities

The four main assembly steps took place in the CUORE cleanroom on the first floor of the CUORE hut underground at the LNGS (Fig. 7). The cleanroom is a class 1000 with approximately 100 m^2 floor space, divided into five sub-volumes (called CR1, CR2, CR3, CR4 and CR5, Fig. 14). CR1 is an entrance area, divided in sub-areas by curtains in order to separate the vestibule from the entrance to the other rooms (except CR4, which is accessible from CR3 only). The use of the other rooms changed according to the different phases of the CUORE construction, in particular during the detector assembly and cryostat commissioning phase, and the detector installation phase.

In the construction phase, CR2 was dedicated to the semi-automatic gluing system. Namely, CR2 has a feedthrough towards the ground floor of the hut, where the pump and the main unit of the robotic arm of the gluing system are located. It is served with water lines for the gluing system chiller. The CUORE gluing proceeded independently from other activities in the hut.

The mechanical assembly and wirebonding took place in CR3 and CR4 through the CUORE Towers Assembly Line (C-TAL). Dedicated glove boxes were used to assemble and wire the several components in a clean environment, preserving the radiopurity of the detector during the construction. An ancillary glove

box was also used to prepare the sub-assemblies for the operations in the main ones. Once completed, the CUORE towers were stored in dedicated areas of CR3 and CR4 in special boxes flushed with nitrogen.

The heavy mechanical work of constructing the cryostat took place in CR5. In reality, CR5 could not be maintained as a cleanroom until the end of the cryostat commissioning. CR5 personnel used the same entrance to the hut as personnel doing critically clean work in CR2, CR3, and CR4, leading to difficulties maintaining cleanliness of CR5 itself. Therefore, the installation of the CUORE detector into the cryostsat took place in a special soft-wall cleanroom (called CR6), designed to fit into CR5 and supplied with radon-free air. The introduction of CR6 was not the only modification of the CUORE cleanroom in view of the tower installation. CR1 was re-organized in order to guarantee a clean path between CR3/CR4, where the stored towers were located, and CR6; CR2 became a second vestibule; CR4 became a storage area.

Some modifications of the logistical environment will be required of the CUORE assembly line in order for it to be used for the CUPID detector assembly. Primarily, the wire bonding operations must be decoupled from the detector mounting. Wire bonding is a delicate task that can only be performed by trained personnel, and can interfere with the detector mounting if the two operations are performed in the same space. Considering that both the procedures must be completely revised for CUPID, this is an opportunity to properly decouple these tasks and relocate the bonding equipment outside C-TAL. Moreover, completely decoupling CR5 from the other rooms is desirable to preserve the cleanliness of the other cleanroom areas.

3.7.2 Other support facilities

We also performed many core assembly tasks in other facilities provided by LNGS. We cleaned and processed the small parts such as heaters, thermistors, PTFE supports, and tools for assembly using cleanrooms, wet benches, and laminar flow hoods in the above-ground chemical labs. LNGS also provided lab space for electrical testing the CuPEN readout strips. We used the underground parts storage area, adjacent to the CUORE hut, to store parts prior to assembly, as well as to store glued crystals prior to integration into towers. We also employed a fume hood and a cleanroom for cleaning and reprocessing of thermistors and heaters that were not successfully glued to the crystals. We expect CUPID will require similar support.

3.7.3 Gluing

As noted earlier, we performed the gluing in CR2. We carried out the entire operation in a nitrogen-flushed glovebox to prevent any radon recontamination of the crystals. The system consisted of a station for crystal loading and inspection: a robotic arm moved the crystals from the inspection station to a staging position in the glovebox. Precision positioners were designed to hold the sensors (thermistors and heaters, see Sec. 5) in a fixed position relative to the crystal during gluing. A human operator mounted the sensors on the positioner while a second operator prepared glue for the upcoming operation. Once ready, a second robotic arm printed a matrix of glue dots on the sensor. The operators then instpected the deposited glue matrix with the aid of high resolution cameras and imaging processing software. If the glue matrix passed quality inspection, the robotic arm moved a crystal from the staging area to the positioner allowing the crystal face to come into contact with the glue matrix. The glue was allowed to cure for 50 minutes. After curing, the robotic arm repositioned the glued crystal to the staging area. At the end of the operation, the operators inspected the cured glue matrix with the aid of high-resolution cameras. A semi-automatic GUI interface controlled the entire procedure, which required a team of three technicians and one physicist supervisor. A picture of the CUORE gluing tool is displayed in Fig. 15.

For CUPID, new sensor positioners are needed because of the cylindrical geometry of the Li_2MoO_4 crystals and Ge wafer light detectors. In particular, the latter can be designed starting from the solution adopted during the gluing of the CUPID-0 detector. In this case the Ge wafer was encapsulated in a dedicated PTFE holder, allowing us to handle them as "normal" crystals [30].

The robotic positioning arm and glue dispensing arm requires reprogramming to account for the different geometries and glue matrix patterns for each sensor-detector combination. In CUORE, one tower worth of crystals were glued every two weeks, with operations mostly confined to a single 8-hour shift on weekdays. The time was dominated by the cure time of the glue, i.e. the time that had to elapse before moving on the next crystal. The system had approximately 20% downtime for routine and non-routine maintenance.

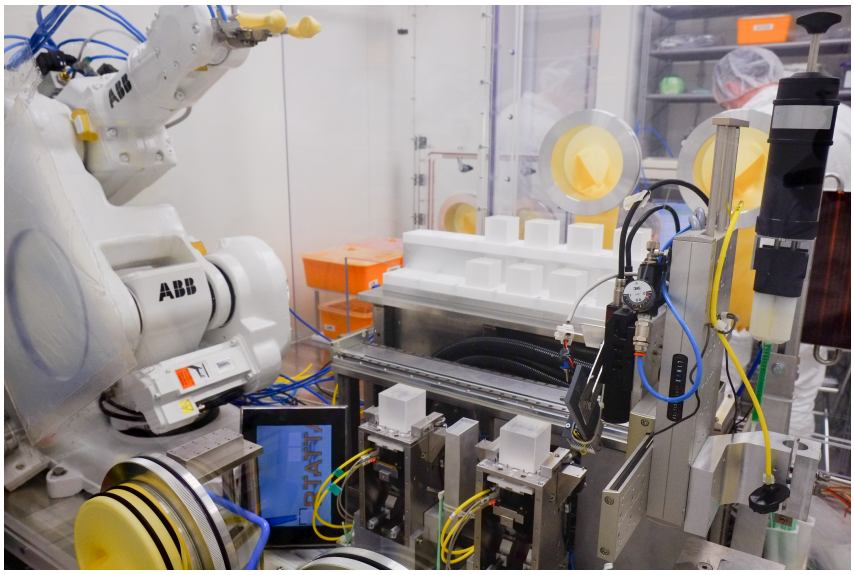


Figure 15: Front view of the CUORE semi-automatic gluing tool, with the robotic arm for crystal handling, the crystal and sensor staging, the two z-positioners (hosting a crystal each), and the robotic arm for the glue deposition.





Figure 16: Left: A CUORE tower under construction into the Mech Box. Right: People working at the End Of the World Glove Box.

3.7.4 Mechanical assembly

The mechanical assembly of the glued crystals and copper frames into towers took place in CR3 and CR4. We performed all steps in specially designed, task-specific, nitrogen-flushed gloveboxes [45] (the C-TAL). The operations include:

- unpacking and quality checking of all copper and PTFE pieces, running-in of all threaded components to avoid gauling during the assembly;
- assembly of copper frames, PTFE holders, and crystal into towers;
- gluing the left and right pack of CuPEN strips to their respective backing copper frame and allowing the glue to cure;
- attaching the CuPEN strip assemblies to the tower.

These operations involved three different glove boxes (Fig. 16): one for the mechanical assembly, one for the preparation of the wirings on related cable trays, and one for the installation of the cable trays on the tower. The main workstation was mounted on a stainless steel air-tight nitrogen flushed chamber equipped with an automated system able to lift and rotate the tower under-construction, as needed. After the tower was assembled, it was removed and stored in a nitrogen-flushed PMMA chamber, and parked inside dedicated racks equipped with nitrogen lines (Fig. 18). The assembly of one tower required a team of four technicians and one week of time.

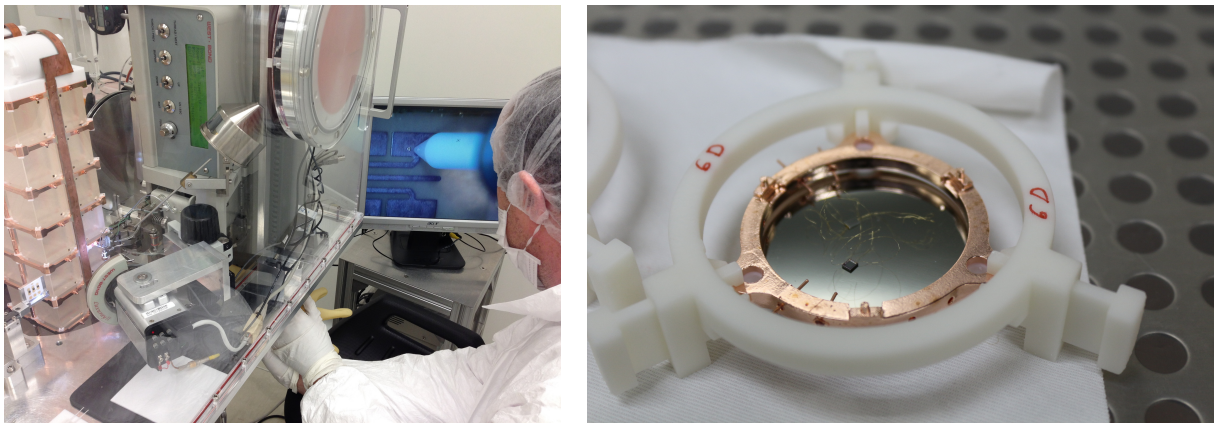


Figure 17: Left: bonding of a CUORE tower. Right: a CUPID-0 light detector pre-assembled in its 3D printed housing.

3.7.5 Wire bonding

In CUORE, the tower design was such that all bonding pads on the sensors and CuPEN strips were accessible from the side of the tower after mechanical assembly. This allowed wirebonds connecting the sensor pads to the readout to be formed at any time. We modified the wire bonding machine to work in a horizontal mode rather than the typical vertical mode and mounted it on travelling rails to increase its range of motion. This allowed for course-positioning of the bonding head relative to the target pad. The final fine-positioning was achieved in the standard way using the integrated manipulator of the bonding machine. The entire setup was enclosed in a nitrogen flushed glovebox to avoid radon contamination of the tower (Fig. 17). Each sensor was instrumented with four $\sim$ 1 cm long wires. The operation was performed in 12 hours shifts by two operators: one operating the wirebonder, and one controlling the course positioning of the tower and bonding machine. The time required to bond a full tower was about one week. Assembled towers were typically bonded in batches of three.

At this stage of the conceptual design, is unlikely that the same bonding protocol can be followed for CUPID; technical R&D on a new protocol is needed. The Li_2MoO_4 crystals will have a cylindrical geometry and the curved outer surface will be wrapped in light-reflecting foil. This constrains the sensors to be attached on one of the flat faces of the crystal. Sensors will not be accessible for bonding once assembled into a tower. Similar considerations apply to the Ge wafer light detectors, which will be interposed between adjacent floors of the tower. A possible approach is to build stand-alone 4-crystal floors or modules and 4-wafer floors that can be stacked together into a tower. Each module could be instrumented with a set of readout strips that connect bonding pads near the sensor location to other bonding pads accessible from the side of the tower. The sensors could be bonded after assembly of the module, and bonded modules could be stacked into towers later. Once the floors are stacked into towers, the externally accessible pads could be wirebonded to the final readout. This would allow most of the wire bonding to proceed in parallel with gluing. The tower assembly protocol would need to include measures to protect delicate wire bonds on each module during assembly.

This approach of having stand alone modules of pre-assembled light detectors was successfully used for the construction of the towers of the CUPID-0 detector. In particular, thanks to dedicated 3D printed holding tools (see Fig. 17), it was possible to avoid the introduction of an additional copper support frame to complete the light detector modules. This allowed adjacent floors to share a single frame as it was for the CUORE towers [30] .

3.7.6 Closing and storage

The final step of CUORE assembly after wirebonding was to place protective copper covers over the CuPEN strip assemblies (Fig. 18). These covers held to strip assemblies tightly against the frame so that they could not freely vibrate. The completed towers were then removed from the workstation and stored in individual nitrogen-flushed boxes in CR4 (see Fig. 18). We anticipate similar storage arrangement will be adequate for CUPID.

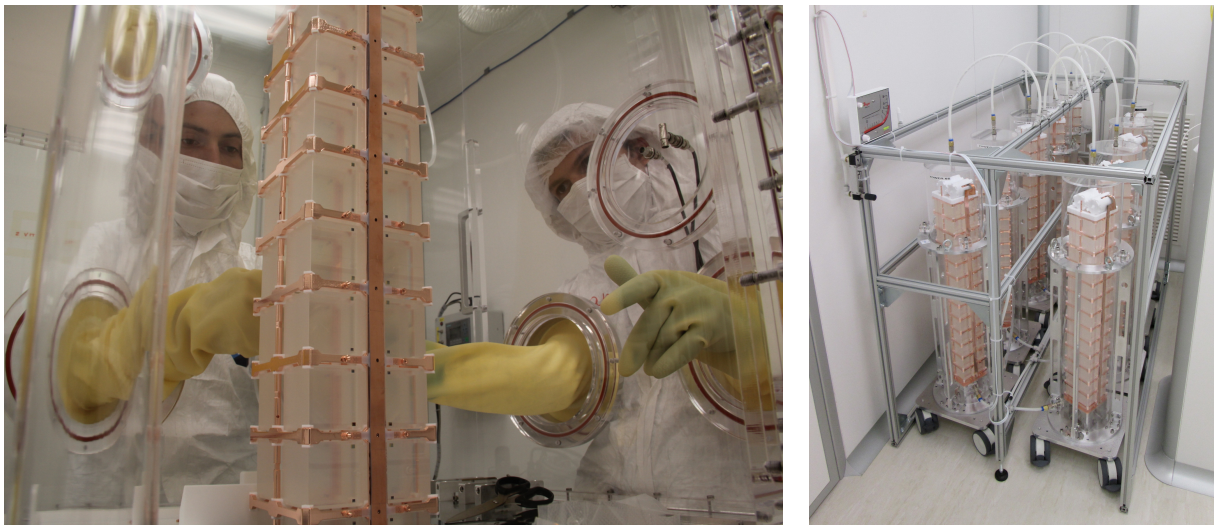


Figure 18: Left: tower cabling. Right: CUORE towers inside their LN_2 storage box.



Figure 19: Installation of the CUORE towers. The top part of the plastic radon bag is visible around the tower support plate. Left: an operator positions a tower using the cart. Right: tower installation completed.

3.7.7 Detector installation

In CUORE, the detectors hang from the TSP, which is in thermal contact with the 10 mK stage. We used a custom-designed cart, which provided fine adjustment of the XYZ position and tilt of the tower, to position the tower under the assigned spot beneath the TSP and raise it into position (Fig. 19, left). The tower was then fixed to the TSP and the readout strips connected. The operations were carried out in a specially designed soft-walled cleanroom (CR6), which was supplied with radon-free air. The towers were installed by a team of three people at a rate of one per day. For redundancy, a cylindrical plastic barrier could be quickly positioned around the bottom of the cryostat, covering the mounted towers. This bag was put in place and continuously flushed with nitrogen when personnel were not working in CR6. and when personnel entered or exited the room. The pace of installation was set by several factors: the time needed for the radon level in CR6 to reduce to acceptable levels after entering or exiting the area; the time needed to re-clean the working area and tools before the next operation; and the desire not to overexert the operators performing the critical and stressful installation task. We anticipate a similar setup and protocol will be adequate for CUPID.

3.7.8 Radon abatement

The storage and assembly procedures for CUPID envision that parts will not be exposed to air, and consequently radon, following their final surface cleaning. This will be achieved by packing and storing parts in a pure nitrogen environment and subsequently assembling parts into detectors in nitrogen-flushed

glove boxes. However, for the safety of personnel carrying out the operation, the attachment of detector towers to the 10 mK stage of the cryostat will be done in air. To reduce the radon in the air to an acceptable level during this installation step, we will reuse the radon abatement system developed for and used by CUORE [46]. The system process is as follows. Intake air is pressurized ~ 9 atm, passed through an oil vapor separator and microfilters, and dried so that the dew point is below ~ -70°C. The air is filtered again to remove liquid and dust after which it is cooled to ~ -55°C, and flushed through two large activated carbon filters (in series) to trap radon. The cooling is necessary to increase the radon absorption efficiency of the charcoal. The output (radon-free) air is then past through a series of HEPA filters and heated to room temperature. The ^{222}Rn activity at the output is reduced to < 5 mBq/m^3 (from ~ 30 Bq/m^3 ambient at LNGS), and the system can produce ~ 120 m^3/h. In the current conceptual design, we envision that the CUPID tower installation will be very similar to our experience in CUORE, and the existing radon abatement system, with standard maintenance, will be adequate for the needs of CUPID installation.

3.8 Front-end electronics

In view of CUPID, we are developing several improvements to the front-end system, aimed at obtaining higher channel density, lower noise for light detectors, and improved DAQ resolution and sampling speed. These upgrades regard the back-end electronics and DAQ system, the very front-end, the power supply, and the stabilization pulser.

3.8.1 The back-end electronics system stage: anti-aliasing and DAQ

The back-end electronics of CUORE performs analog filtering and digitization. It is based on a custom anti-aliasing board with four cut-off frequency settings (15, 35, 100, and 120 Hz) [47] and commercial DAQ boards from National Instruments, operating at a sample rate of 1 kHz per channel [48]. If the present configuration used in CUORE were to be adopted for CUPID without modifications, a channel increase of at least a factor 3 would be necessary, leading to high power consumption, occupied space, and cost. Apart from the increased number of channels, there will also be the necessity to operate at higher sampling rate for optimal pile-up rejection. This will require the re-design or modification of the anti-aliasing filters to allow a wider bandwidth of both the heat and light channels.

For the CUPID back-end we will adopt an upgraded anti-aliasing filter with integrated digitization circuitry. The new anti-aliasing board will offer the capability to digitally select the cut-off frequency in a range from 24 Hz to 2.5 kHz, with a resolution of 10 bits. This will allow independently tuned cut-off frequencies for heat and light channels, and a larger degree of flexibility in the arrangement and customization of each channel. The digitization will be performed by 24-bit delta-sigma ADCs, with a maximum sampling rate of 25 kHz per channel. The data transfer from the board to the DAQ storage will be managed by an FPGA through UDP protocol on inexpensive 1 Gbit/s Ethernet interfaces. The power consumption of this solution is up to a factor 5 lower than the previous solution adopted for CUORE, while the space occupied is half. Another advantage of this configuration is that the storage infrastructure can be placed farther from the DAQ (either above ground or in a less crowded underground space).

A photograph of the first prototype of the board is shown in Fig. 20. The figure also shows the transfer function of the board at different cut-off frequency settings.

Another important feature foreseen for the new anti-aliasing filter is a Programmable Gain Amplifier (PGA). Moving the PGA stage away from the very front-end boards allows to save space at the top of the cryostat, where the very front-end boards reside.

As a backup solution, the newly designed anti-aliasing board can be operated in a fully analog mode with an external DAQ system, making it compatible with the present CUORE readout scheme.

3.8.2 Very front-end and Faraday room

We intend to operate the very front-end at room temperature, and locate it on the top of the cryostat, as in CUORE. In the CUORE scheme, the front-end of each channel consists of an input preamplifier, a second stage PGA, and the detector biasing system [47]. The Faraday room, already in place, has shown the expected shielding performances [49]. In order to save space inside the Faraday room, the PGA stage will be moved outside, at the input of the anti-aliasing filter.

Power dissipation inside the Faraday room is a sensitive quantity to be considered in the design phase. For CUPID, we intend to minimize it in two ways. First, we selected a new family of low noise commercial operational amplifiers with lower supply current; this will be used in most of the analog

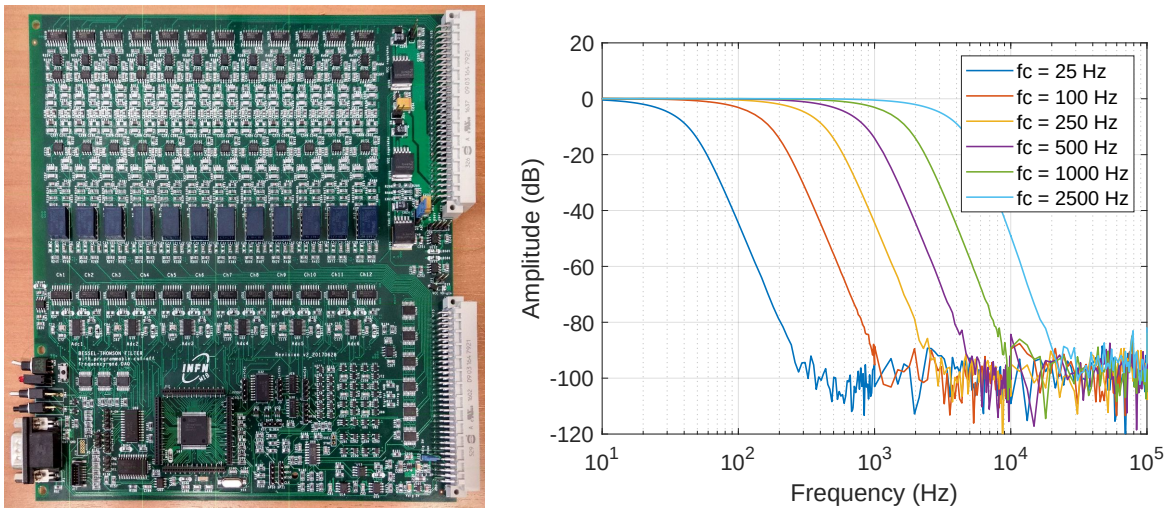


Figure 20: Left: photo of a prototype of the new anti-aliasing filter with integrated DAQ. Right: transfer function of the filter at different cut-off frequency settings (from 25 Hz to 2.5 kHz).

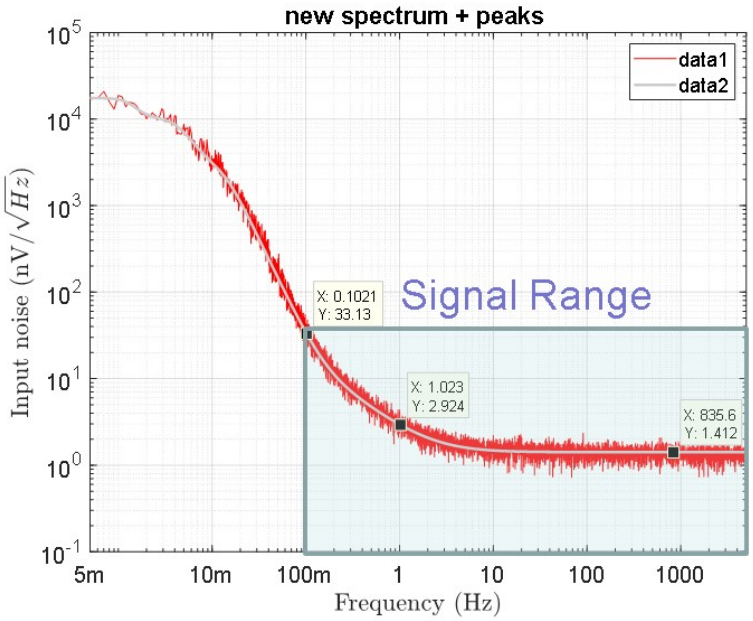


Figure 21: Series input noise of the new pre-amplifier in the low series noise and high power configuration.

circuitry. Furthermore, we intend to consider different preamplifiers for light and thermal channels, characterized by a different level of series input noise and inversely proportional to their operating current. When operated at about 150 mW, the preamplifiers show an input series noise below 1.4 nV/$\sqrt{\text{Hz}}$, (see Fig. 21). If the power is reduced to 70 mW, their input series noise increases to about 3 nV/$\sqrt{\text{Hz}}$. The total expected power dissipated by the front-end electronics, which will be up to 3000 channels, inside the Faraday room (dimensions $6\times6\times2.5$ m^3), is about 600 W, or 6.7 W/m^3 on average. No additional cooling system is foreseen with respect to CUORE. The differential voltage-sensitive front-end preamplifiers show also small parallel noise and, with the new generation of JFETs we recently selected, the expected current at each input gate is about 100 fA, or 0.13 fA/$\sqrt{\text{Hz}}$. The input capacitance is below 20 pF.

The general scheme of the biasing circuitry for the detectors will be maintained as in CUORE, i.e. the detectors will be biased with a constant current injected through very large value resistors (tens of GΩ range). The value of the resistors will be optimized depending on the expected impedance of the detectors at their optimal working temperatures.

3.8.3 Power supply and stabilization pulser

The power supply of CUORE was designed with 3 stages: AC/DC, DC/DC [50], and linear [51] regulators. By design, it is floating with respect to earth and to shows exceptionally low thermal drift and noise. The AC/DC and DC/DC regulators are located outside the Faraday room, while the linear regulators are located inside the front-end racks. We intend to maintain the same approach in CUPID.

The periodic calibration of the detector array with known radioactive sources is expected between physics runs. However, to stabilize the operation of the detectors during each physics run, two techniques are used. First, since the front-end amplifiers are DC-coupled to the detectors, and are designed to show a negligible temperature drift, the baseline of each detector is proportional to its temperature. The baseline can therefore be monitored and used to stabilize the detector response over long data collection periods. Second, for CUORE we developed a series of pulsers having a stability $\lesssim 1$ ppm/°C [52], which are used to simulate particle hits by sending short voltage pulses on heating resistors glued to each detector crystal (see Sec. 5.2). The height of the pulser signals, which are triggered periodically by the DAQ system and properly tagged, is used to track any temperature or gain variation of the detectors during each run. The same strategy and design will also be used for CUPID.

3.9 Computing infrastructure: data acquisition, storage, online processing, and monitoring

The CUPID experiment will handle an amount of data about a factor of ∼10 larger than in CUORE. This rough estimate comes from considering a larger signal bandwidth, about 3000 channels instead of 1000, and a further factor of ∼2 for a conservative estimation. CUORE is producing about 100 GB/day of raw data, so a reasonable estimation for CUPID is 1 TB/day. In this section we briefly summarize how we plan to manage these data in terms of data acquisition and storage, and of the overall computing infrastructure of CUPID.

As already stated in Sec. 3.8, a simplification of the data acquisition hardware is foreseen for CUPID. It consists in replacing the commercial digitizers used in CUORE with custom boards featuring a higher channel density, serving both as anti-aliasing filters and digitizers. This improvement will make the readout system significantly more compact and will remove the limitations on the operating system of the readout computers, imposed in CUORE by the commercial drivers of the digitizer boards. The CUORE data acquisition system [48] has a modular structure, so it can be easily adapted to the different digitizer hardware and to the larger number of channels of CUPID. Another simplification in the data acquisition system is likely to take place in CUPID. The CUORE DAQ system not only took care of acquiring and saving the continuous bolometer waveforms, but also of searching for signal triggers and building the corresponding events. However, in CUPID the larger amount of data will make it preferable to move the process of triggering and event-building offline. This change of paradigm will make the data acquisition system simpler and more scalable, and will allow more sophisticated trigger algoritms as long as enough computing resources are available.

In CUORE, a multi-site approach is being pursued for storing the acquired and processed data. The primary storage site is located above ground at the LNGS, with two other mirror storage sites at CNAF (Italy) and NERSC (USA). This approach proved to be robust against data losses and we plan to replicate it for CUPID. Some care must be taken to make sure that the bandwidth of the data links between underground and above-ground sites at LNGS, and from LNGS to the secondary storage sites, are still large enough to deal with the larger amount of data expected in CUPID.

Apart from some minor upgrades, we plan to use the same computing infrastructure that we are using in CUORE. It consists of services and resources distributed over several physical sites. The core services, whose availability is compulsory for the operation of the data acquisition system, are located underground at LNGS in order to minimize the downtime due to malfunctioning of the network. The other non-critical services required for the operation of the experiment are located above-ground at the LNGS. The day-by-day data processing, whose main purpose is to assess the quality of the acquired data, is performed on a small-size computing cluster above ground at the LNGS [53]. Monte Carlo simulations and heavier data processing, usually performed with longer latency (on the month to a few months timescale), are carried out at remote clusters (mostly CNAF but also NERSC) where more computing resources are available. The amount of computing resources used in CUORE, which involved a few hundred parallel cores, is small compared to the typical needs of high energy physics experiments, and it is unlikely that the transition to CUPID will have a significant impact in this regard. However, in the event that more parallel and efficient data processing algorithms will be exploited in CUPID, the migration to a more efficient computing paradigm (e.g. GRID-based) will be considered.

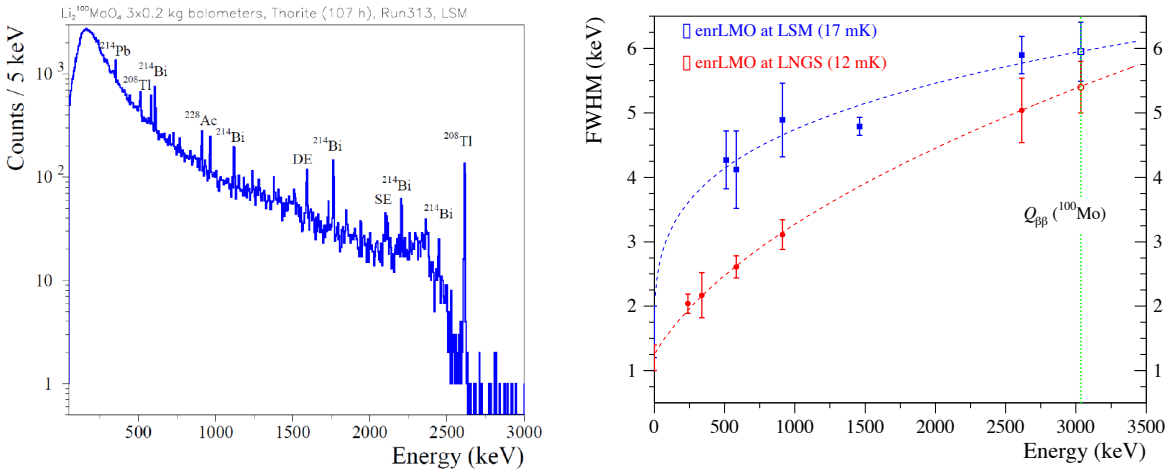


Figure 22: Left – Energy spectrum of CUPID-Mo towers for 2.7 kg·d exposure calibrated with a ^{232}Th source. Right – FWHM resolution scaling and extrapolation to the ROI (hollow markers) at different working points at LSM (blue) and LNGS (red).

In summary, the data acquisition, storage, and computing model of CUPID will be heavily based on what was already put in place for CUORE. None of the planned upgrades is expected to imply significant risks for the successful outcome of the experiment.

3.10 Calibration systems

3.10.1 Li_2MoO_4 calibration

An accurate calibration is mandatory for CUPID, in particular in the 3 MeV region where the $0\nu\beta\beta$ signal of ^{100}Mo is expected. A ^{232}Th source emits a γ line at 2615 keV and is an obvious choice since this natural radionucleide is present in many common materials. A ^{56}Co source emits γ lines up to 3612 keV, offering the possibility to calibrate at 3 MeV and above. Due to the relatively short half-life (77 days) the ^{56}Co source can only be used for a few months after its production.

Currently the CUORE detector can be calibrated by an internal calibration system, which deploys low-activity thoriated strings from room temperature into the cryogenic volume, and by an external calibration system that deploys high activity ^{232}Th and ^{60}Co sources in the volume between the outside of the OVC and inside of the external lead shield. The activities of the internal and external calibration sources are optimized by Monte-Carlo simulations in order to avoid a large number of pile-up events while also maintaining a reasonable duration of the calibration run. Figure 22 (left) shows the calibration of the CUPID-Mo towers using a ^{232}Th source.

3.10.2 Light detector calibration

A calibration of the light detectors is impossible using γ sources of the kind used for the calibration of massive detectors. Thus, it is common to use an X-ray ^{55}Fe source to calibrate light detectors (Fig. 23, left). The use of a ^{55}Fe source might be problematic in an ultra-low background environment. Hoever, the light detector calibration is optional because it does not strongly affect the α/γ separation capability. In order to overcome the issue, we can use a high intensity γ source (e.g. $\sim$100 Bq ^{60}Co source [54]) to stimulate X-ray fluorescent of materials (mainly, Li_2MoO_4 crystal), which are close to light detectors. An example of such calibration is illustrated in Fig. 23, right [27].

3.11 Muon tagger

Atmospheric muons produce two types of backgrounds in a bolometric detector: direct energy deposits by muons passing through the crystals, and muon-induced spallation. Interactions from the muons in the rock or the external lead shield cause spallation products that can lead to fast neutron backgrounds. Muons can be effectively tagged in CUPID if they go directly through multiple crystals; however, they can cause irreducible backgrounds if they clip corners or interact in the surrounding materials to create

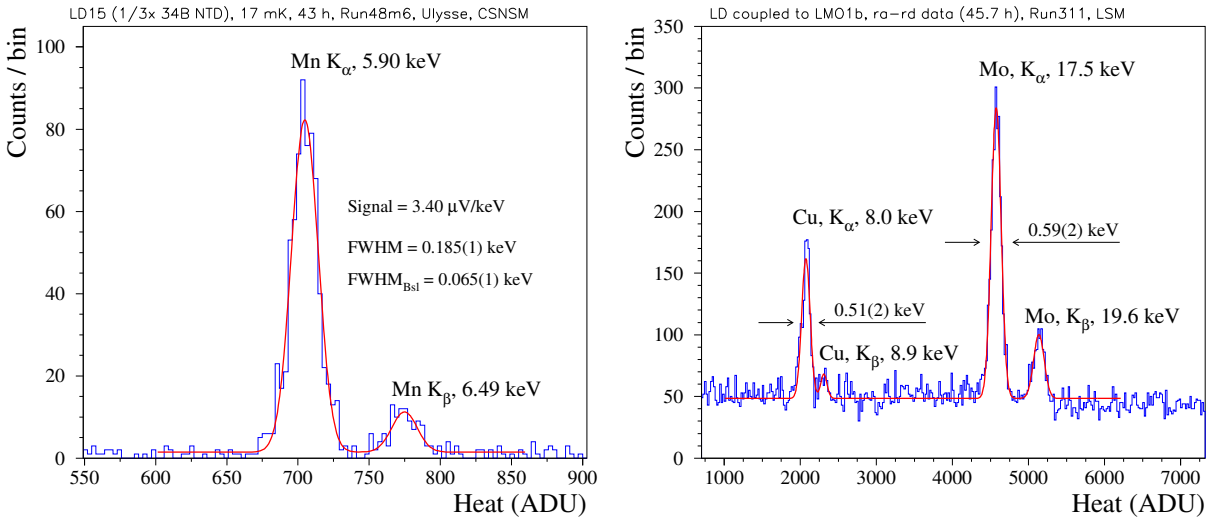


Figure 23: Left – Energy spectra of X-rays accumulated by 44.5 mm diameter Ge light detectors instrumented with NTDs (see Sec. 5). Right – The measurements were performed in the above-ground cryogenic laboratory of CSNSM (left) and at LSM. The energy scale is given in analog-to-digit units (ADU).

secondaries that can produce particles mimicking $0\nu\beta\beta$-like signal. Neutrons produced by cosmic rays are energetic and difficult to shield. Photons emitted in (n, n'γ) or (n, γ) reactions can appear near $Q_{\beta\beta}$.

The muon flux at Gran Sasso National Laboratory is $\sim 2.6 \cdot 10^{-8}$ cm^{-2}s^{-1}, as reported by MACRO and BOREXINO [55–57]. The muon-induced backgrounds in Cuoricino have also been measured and projected onto what we expect in CUORE and CUPID [58, 59]. As summarized in Sec. 7.4, the total background rate expected from muons in the CUPID detector is $\sim 10^{-4}$counts/(keV·kg·yr). This background can be reduced by at least an order of magnitude by a dedicated muon tagger/veto system. The system to be developed for CUPID will use the design of the muon tagger system developed for CUORE (Fig. 24) and the experience of the similar systems built for Cuoricino and CUPID-0.

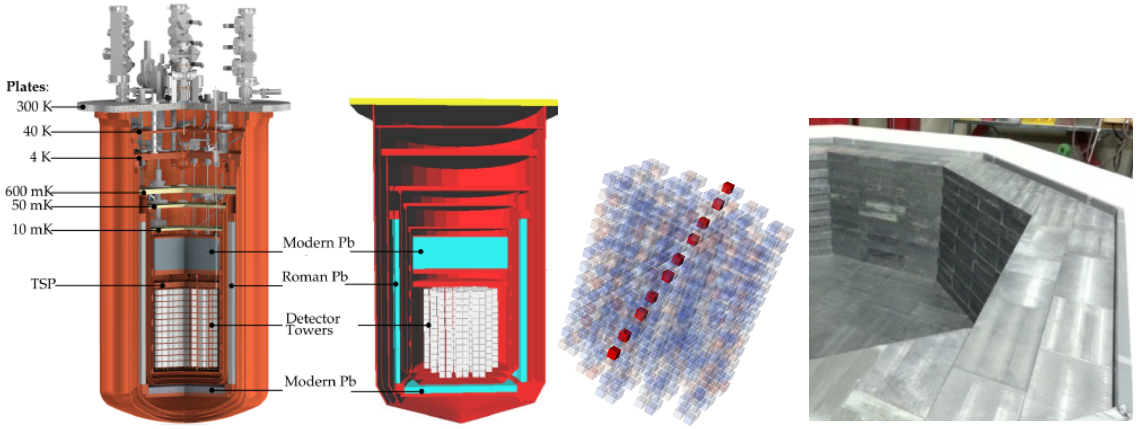


Figure 24: Left: 3D view of the CUORE apparatus and geometry implemented in Monte Carlo simulations. Center: Simulated muon event in CUORE. The solid red color indicates crystals hit by muons, the transparent colors indicate the simulated base temperature of each crystal. Muons that go through multiple crystals will be easy to tag. Right: CUORE Pb and polyethylene shielding outside the cryostat.

The muon tagger consists of a set of vertical scintillator panels to be arranged around the CUPID cryostat and a set of horizontal panels above or below the cryostat. The large scintillator panels will be read out with optical fibers arranged in an x-y grid over the panels to provide good coverage and x-y positioning at economical costs. The dimensions and segmentation of the tagger is being optimized to provide tagging and crude tracking capabilities. The tagger will allow us to identify muons that produce

single-site energy deposits in the CUPID crystals, or miss the inner crystal array but enter the nearby lead shielding. The geometry of the system will be customized to fit the available space around the cryostat.

Simulations provide estimates for the the expected event rates: 1.8 muons/hour in the CUPID crystals, 7.0 muons/hour in lead shield. With the preliminary tagger design, we estimate that for the muons leaving a single-site energy deposit near the $Q_{\beta\beta}$ ROI (2950 − 3100 keV), $(77 \pm 1)\%$ would be detected in the vertical tagger panels, and $(62 \pm 1)\%$ would be detected in the tagged by the horizontal panel. Combined, the two panels provide over 99% rejection of the single-site muon-induced events.

3.12 Cryogenic testing infrastructure

Even if CUPID is not in an R&D phase, there are still some issues that need to be tested in order to define the final layout of the detector (e.g. the mechanical structure) as well as to assure the quality of its components (crystals, sensors, etc.). In this section we briefly describe the underground and above-ground facilities where those measurements can be conducted.

3.12.1 Underground cryostats at LNGS

INFN has several test cryostats located deep underground in the LNGS. All of them are already equipped with electronics and DAQs in order to operate large arrays of scintillating bolometers.

The largest one is the one in the Hall-A of the LNGS that hosted Cuoricino [41], CUORE-0 [6], and is presently hosting the CUPID-0 [15] experiment. It consists of a completely custom wet Oxford 1000 dilution unit, able to reach a base temperature of ∼6.5 mK with a cooling power of 1 mW @ 100 mK. The available experimental volume is approximately a cylinder of 178 mm diameter and a length of 880 mm, resulting in a total experimental volume of ∼ 22 L. This volume is surrounded by a 1.4-cm-thick Roman lead cylindrical shield. A Roman lead disc, 10-cm-thick and 17 cm in diameter, is placed below the Mixing Chamber to shield against the intrinsic radioactivity of the dilution refrigerator. The cryostat is externally shielded by two layers of lead with a minimum thickness of 20 cm. The external lead shielding is surrounded by an acrylic glass anti-radon box flushed with nitrogen gas to reduce Rn contamination. Finally, a 10-cm-thick layer of borated polyethylene is used as neutron shielding. The entire apparatus is enclosed in a Faraday cage to minimize electromagnetic interference. The cryostat is instrumented with 136 twisted pairs of NbTi wires from room temperature down to the Mixing Chamber. Presently we have 66 acquisition channels, the same type of electronics used in CUORE. The detectors can be mounted into the cryostat within a dedicated cleanroom, located just above the cryostat, in which the dilution unit can be raised. This guarantees a clean environment with a relatively low radon content (∼ 5 Bq/m^3). Due to its peculiar characteristics, this facility is dedicated to large scale demonstrators that need a very low γ background environment. The present achieved background level at 3 MeV is of the order of $\sim 3.6\times10^{-3}$ counts/(keV·kg·yr). The cryostat needs a ^{4}He liquid Helium refill (∼ 60 L) every two days, that takes roughly 40 minutes to complete. The total mean dead time induced by the refilling procedure is about 90 minutes. The time needed to reach the base operational temperature, starting from room temperature, is ∼10-12 days.

The Hall-C CUPID-0 R&D test facility consists of custom Oxford TL 200 wet dilution cryostat. The base temperature is 7.5 mK with a cooling power of 0.2 mW at 100 mK. The experimental volume is smaller with respect to the one in Hall-A: a cylinder of 182 mm in diameter and a height of 310 mm, totaling ∼ 8 L. The radioactive shielding is less effective with respect to the Hall-A cryostat, consisting of a Roman lead disc, 5-cm-thick and 17.5 cm in diameter, placed just below the Mixing Chamber. The cryostat is then externally shielded by two layers of lead with a minimum thickness of 15 cm. The external lead shielding is surrounded by an acrylic glass anti-radon box flushed with nitrogen gas to reduce Rn contamination. Just outside, a 1-cm-thick shield of CB_4 acts as neutron catcher. The neutrons are thermalized by an 8-cm-thick layer of polyethylene. The entire apparatus is enclosed in a Faraday cage to minimize electromagnetic interference. Using the 2615 keV γ-line of ^{208}Tl as an evaluation metric, the background level that can be achieved in this cryostat is about 6 times larger with respect to the one in Hall-A. The cryostat is equipped with different type of readout electronics:

- 10 COLD electronics channels [60] framed *inside* the cryostat with Load Resistor of 27+27 GΩ;
- 10 COLD electronics channels framed *inside* the cryostat with Load Resistor of 2+2 GΩ;
- 12 standard electronic channels, similar to the CUORE ones;
- 24 additional twisted wires from room temperature down to the Mixing Chamber;

– 2 400 kHz DC squids (anchored at the 1.2 K thermal stage).

A Helium re-liquefier continuously fills the cryostat, keeping the He level constant, resulting in an almost 100% duty cycle. The time needed to reach the base operational temperature, starting from room temperature, is roughly 5-6 days.

The IETI test-cryostat [61] is a Pulse Tube dry dilution refrigerator, located in the same hut as the CUPID-0 R&D facility, just few meters away. This is a completely custom cryostat based on a MKN-CF-500 dilution unit produced by Leiden Cryogenic, with a cooling power of 0.5 mW at 120 mK and a base temperature of the order of 7 mK. The experimental volume is a cylinder of 32 cm in diameter and a height of 17 cm totalling 13 L.

The cryostat is equipped with 12 standard electronic channels, similar to the one of CUORE, and 52 twisted pairs of NbTi wires from room temperature to the Mixing Chamber. This cryostat can be shielded with an outside layer of 10 cm of lead, while the internal shielding is of 3 cm of lead below the MC. This facility is, therefore, mainly devoted for testing the performances of the detectors, thermometry, and NTD characterization. The time needed to reach the base operational temperature, starting from room temperature is, about 3-4 days.

3.12.2 Cryostats outside LNGS

Beside the LNGS underground cryostats, there are several above-ground cryostats available among the various institution of the CUPID interest group (e.g. at Berkeley, CEA, Milano-Bicocca, MIT, and Rome). These can be used for all the measurements that don't require a low-background environment, such as sensors characterization, test of detectors performances, thermometry, etc. Underground facilities are also available.

3.12.3 Edelweiss-II cryostat at LSM

CUPID-Mo is presently installed in the EDELWEISS-II cryostat located in the Laboratoire Souterrain de Modane (LSM) where the rock overburden of 4800 m w.e. reduces the cosmic muon flux down to 4 $\mu/m^2/day$. The detectors are placed in the 10 mK chamber and arranged on plates supported by three vertical bars. Below the 10 mK plate, at 1K, a 14 cm thick lead plate shields the detectors from the gamma-rays induced by the radioactivity in the cold electronics, the dilution unit, and other cryogenic parts. Five thermal copper screens at 1 K, 4.2 K, 40 K, 100 K, and 300 K complete the cryostat. Resistors together with electrical connectors are installed at the 1K stage below the lead shielding. At the 100K stage the cold JFETs are connected on an extractable panel. The electronics to bias the JFETs, the DACs to bias the detectors, the final amplification, the anti-aliasing filter, and the digitization are all integrated in a single room-temperature module, called the Bolometer Box, which is attached to the cryostat.

An 18-cm-thick outer layer of modern lead shields the cryostat against ambient gamma background. A 2-cm-thick inner Roman lead layer has been cast directly on the modern lead. An outer 50-cm-thick polyethylene shielding protects the detector against ambient neutrons. The lead and polyethylene shielding is mounted on a mild steel structure with rails allowing the opening of the two halves of the shielding structure. In addition, a 100 m^2 plastic scintillator active muon veto surrounds the polyethylene.

3.12.4 CROSS cryostat at LSC

The CROSS cryostat was installed in April 2019 at the Laboratorio Subterraneo de Canfranc, at 2500 m.w.e. The cryostat was fabricated by Cryoconcept and has a unique method to reject vibrations induced by the Pulse Tube: it utilizes a thermal machine, which guarantees the precooling down to 4 K of the 3 He- 4 He mixture employed in the dilution refrigeration. This method avoids a direct mechanical coupling between the cold stages of the Pulse Tube and the refrigerator and it is not available in systems produced by other companies. The experimental volume (a cylinder d= 300 mm, h= 605 mm) is limited upwards by a copper floating plate (at 10 mK) that is suspended by a system of wires and springs to reduce further vibrations. The detectors are connected to this plate and are surrounded by a thin copper screen at 10 mK as well. The experimental volume is shielded from above by a fixed 13-cm-thick low-radioactivity internal lead shield. Laterally and downwards, the experimental volume is surrounded by the aforementioned copper screens and then by the external lead shield of 25 cm.

4 Enrichment, purification, and crystallization

The success of CUPID will strongly depend on the of the $Li_2{}^{100}MoO_4$ crystals quality in terms of energy resolution, light output, and radioactive contamination. In this section, we describe the available sources of ^{100}Moenriched Mo, the material purification process, and the available crystal growth techniques.

4.1 Procurement of ^{100}Mo-enriched molybdenum

^{100}Mo-enriched molybdenum is produced using gas centrifuges. First, molybdenum is converted to MoF_6 gas by fluorinating natural molybdenum:

$$^{\rm nat}{\rm Mo} + 3{\rm F}_2 \rightarrow {}^{\rm nat}{\rm MoF}_6,$$

and then enriched with a cascade of centrifuges. At the next stage, the $^{100}MoF_6$ gas is converted into $^{100}MoO_3$ using the wet chemistry processes:

$$^{100}{\rm MoF}_6 + {\rm H}_2{\rm O} + {\rm HNO}_3 \rightarrow (\text{precipitation and calcination}) \rightarrow {}^{100}{\rm MoO}_3 \quad ,$$
$$^{100}{\rm MoO}_3 + {\rm H}_2{\rm O} + {\rm NH}_3 \rightarrow (\text{precipitation and calcination}) \rightarrow {}^{100}{\rm MoO}_3 \quad ,$$

which produces $^{100}MoO_3$ in the form of a fine powder. If necessary, $^{100}MoO_3$ is reduced to metallic powder ^{100}Mo. Thus, enriched molybdenum is supplied to the customer in the form of MoO_3 powder, or metal powder. Enrichment is usually in the 90–99% range.

Several Russian companies can produce stable isotopes by centrifuging. In order to successfully enrich molybdenum, a company must master a procedure for converting molybdenum to the gaseous phase and vice versa. Due to the difficulty of these processes, enriched molybdenum is currently produced by only one enterprise, the Electro-Chemical Plant (ECP) in Zelenogorsk, Russia [62], although the ^{100}Mo production can in principle be organized at other companies too. ECP is mainly engaged in the production of enriched uranium for nuclear power plants. The production of stable isotopes at this company started in the 1970s. Eventually, a dedicated production line was set for the extraction of stable isotopes using the SVETLANA plant with an independent gas centrifuge complex. Currently, a large number of isotopes are produced here for medicine, electronics, biology, chemistry, and physics. In recent years, the interest in ^{98}Mo has increased, from which ^{99}Mo is then obtained. This is due to the widespread use of the ^{99}Mo isotope in medicine (more precisely, ^{99m}Tc, which is the product of ^{99}Mo β decay). In this case, ^{99}Mo can be obtained from ^{100}Mo on accelerators. In this regard, we can expect an increased request of significant quantities (tens of kg) of ^{98}Mo and ^{100}Mo from nuclear medicine in the near future.

In the Soviet Union, and then in Russia, ^{100}Mo had been produced in large quantities (> 1 kg) since the 1980s. The production was mainly associated with $0\nu\beta\beta$ decay experiments. A summary of the main ^{100}Mo production batches is reported in Table 2. To date, ∼145 kg of ^{100}Mo has been produced in the world. The first contacts with ECP representatives showed that the production of 300 kg of ^{100}Mo with $> 95\%$ enrichment is feasible in a 3–5 year framework.

Table 2: ^{100}Mo production history. The last three columns report the measured contamination levels of the material after enrichment and prior to crystal growth.

Date	Amount [kg]	Enrichment [%]	Current Owner	Contamination [mBq/kg] ^{228}Th	^{226}Ra	^{40}K
1980s	~ 1	99.5	INR, Kiev (Ukraine)	~ 2.5	~ 10	~ 100
1980s	~ 1	98.5	ITEP, Moskow (Russia)	~ 2.5	~ 10	~ 100
1990s	~ 12	95–99	NEMO-3 collaboration	1–5	1–6	50–140
2016-19	~ 120	96	AMoRE collaboration	< 2	< 4	

4.2 Purification of materials for crystal growth

4.2.1 Enriched ^{100}Mo purification

The purity level of commercially available molybdenum does not satisfy the radiopurity requirements for the growth of high quality Li_2MoO_4 crystals. Indeed, the scintillation performance of $ZnMoO_4$ crystals, which are very similar to Li_2MoO_4, was substantially improved after some additional molybdenum purification [10, 63–65]. Table 3 reports impurity values for commercial 5N grade molybdenum oxide

and enriched ^{100}Mo. Roughly, the purity level of the enriched molybdenum after production should be improved by one order of magnitude in order to obtain high quality scintillating crystals. The purity levels of the enriched isotope ^{100}Mo as delivered by the producer are even worse.

Table 3: Purity level of commercial 5N grade molybdenum oxide and of enriched ^{100}Mo.

Material	Impurity concentration [ppm]					
	Na	Si	K	Ca	Fe	W
Commercial 5N grade MoO_3 used for $ZnMoO_4$ crystals [66, 67]	24	9	67	15	< 18	96
Samples of enriched ^{100}Mo used in [68] (values after production)	10	50–360	< 30	40–50	10–80	200

The NEMO-3 collaboration observed high radioactive contamination of enriched ^{100}Mo samples using low-background HPGe γ spectroscopy. The radioactive contamination of the samples was on the level of ~ 0.1 Bq/kg for ^{40}K, ^{234}Th, and ^{235}U, and of a few mBq/kg for ^{208}Tl, ^{228}Ac and ^{214}Bi [69]. Similarly, the poor optical quality and high radioactive contamination of $ZnMoO_4$ and Li_2MoO_4 crystals produced from commercially available high purity grade molybdenum [11, 66, 67, 70, 71] with natural isotopic composition confirms the need for additional material purification prior to Li_2MoO_4 crystal growth.

We developed a two stage technique for molybdenum purification [64]. The procedure consists of a two-stage sublimation with addition of zinc molybdate, and a double recrystallization from aqueous solutions of ammonium para-molybdate by co-precipitation of impurities on zinc molybdate sediment. The addition of high purity $ZnMoO_4$ (up to 1%) substantially reduces the tungsten contamination, whose impurity is hard to remove because of its chemical affinity to molybdenum. During the sublimation at high temperature the following exchange reaction occurs:

$$ZnMoO_4 + WO_3 \rightarrow ZnWO_4 + MoO_3.$$

In addition to inducing a substantial decrease of tungsten, the sublimation reduces the concentration of radioactive impurities (K, Th, U, Ra, Pb) and other contaminants, e.g. transition metals that affect the Li_2MoO_4 crystals optical quality (Ca, Cu, Fe, Mg, Na, Si, Zn, etc.). The sublimate is annealed in air atmosphere to obtain yellow color stoichiometric MoO_3. The analysis of the obtained sublimate by atomic emission spectrometry showed an improvement of the MoO_3 purity level by at least one order of magnitude. The efficiency of molybdenum purification by sublimation is presented in Table 4.

Table 4: Efficiency of molybdenum oxide purification by sublimation.

Material	Impurity concentration (ppm)			
	Si	K	Fe	W
Initial MoO_3	600	$100 - 500$	6	$200 - 500$
After 1st sublimation	$100 - 500$	$10 - 50$	$2 - 6$	$100 - 200$
After 2nd sublimation	70	$1 - 8$	< 1	$30 - 40$

After the sublimation process, the molybdenum is further purified by double recrystallization of ammonium molybdate in aqueous solutions. Molybdenum oxide is dissolved in ammonia solution at room temperature. To improve the recrystallization process efficiency, zinc oxide is dissolve at the level of $1 - 2$ g/L in the ammonium para-molybdate solution at a pH> 6 to initiate precipitation. Ammonia is then added to the solution to reach a pH$= 7 - 8$. The precipitation of zinc molybdate occurs after several hours. The $ZnMoO_4$ sediment absorbs the impurities from the solution. A further pH increase leads to the precipitation of contaminants in the form of hydroxides. It should be stressed that the basic solution with a pH$\sim 8 - 9$ provides the most favorable conditions for Th and U precipitation. After the separation of the sediment, the solution is evaporated to 70% at a temperature near its boiling point. Ammonium oxalate is then added to the solution as a scavenger for the residual iron impurities which are thus bound together and removed from MoO_3.

The purity levels of the so-obtained MoO_3 (Table 5) fully satisfy the CUPID requirements. Natural and enriched Li_2MoO_4 crystal tested at LSM and LNGS were characterized by ^{228}Th and ^{226}Ra contamination levels < 10 μBq/kg [39].

Table 5: MoO_3 purity levels before and after the purification by sublimation and recrystallization.

Material	Impurity concentration (ppm)			
	Si	K	Fe	W
Initial MoO_3	60	50	8	200
Recrystallization from aqueous solutions	30	20	6	220
Sublimation and recrystallization from aqueous solutions	30	10	5	130
Double sublimation and recrystalizzation from aqueous solutions	–	< 10	< 5	< 50

4.2.2 Lithium purification

The chemical affinity of lithium with potassium resulted in a considerably high ^{40}K contamination of $\sim$ 0.1 Bq/kg in one of the first Li_2MoO_4 crystals tested [72]. Similarly, the affinity of lithium with radium and the observation of ^{226}Ra in some Li_2MoO_4 samples [13], imposes strict requirements on the purity of lithium carbonate (Li_2CO_3) employed for the Li_2MoO_4 crystal growth. The 99.99% purity level of the commercially available high purity Li_2CO_3 is high enough to produce high quality, radiopure Li_2MoO_4 crystals [39, 73]. Nevertheless, an R&D for additional Li_2CO_3 purification based on the washing of precipitate and recrystallization is underway.

4.3 Chemical processing and synthesis of Li_2MoO_4

The production of Li_2MoO_4 crystals can be performed starting from molybdenum of different forms – e.g. metal ingots, metal foils, or oxide – according to the following procedure. The highly purified molybdenum oxide and commercial high purity lithium carbonate is annealed at temperature $\sim$ (350–400)℃, weighted in the required stoichiometry ratio, and mixed. The powder is then placed directly into the platinum crucible used for the crystal growth, where the following reaction of Li_2MoO_4 solid-state synthesis takes place:

$$MoO_3 + Li_2CO_3 \rightarrow Li_2MoO_4 + CO_2.$$

The synthesis is carried out in three stages:

- fast heating until the synthesis begins;
- slow heating for 5–10 hours at $\sim$ 450℃, until the release of CO_2 gas has terminated;
- fast heating to the melting temperature.

4.4 Crystal growth by the low-thermal-gradient Czochralski technique

Typically, Li_2MoO_4 crystals are grown in air atmosphere from the synthesized powder with the low-thermal-gradient Czochralski technique [74, 75] using a platinum crucible of 70 mm diameter and 130 mm height. The platinum crucible is placed into a three-zone resistance furnace with low thermal conductivity bottom and top thermal insulation. The scheme of the growing set-up is shown in Fig. 25. The crucible is covered by a platinum lid with a pipe socket through which the pull rode with the crystal holder is introduced into the inner space. During the entire growth process the crystal remains inside the crucible. The heater and control system allow to keep the axial and radial thermal gradients within $0.05 - 1.0$ ℃/cm. This crystal growth technique is fully controlled by the weighing method at all stages including the seeding, as any visual inspection is impossible.

The growth rate varies from 0.5 mm/h to 0.75 mm/h. The rotation velocity is about 3 rounds/min. A typical duration of the growth process is 10–12 days.

A second-crystallization crystal growth is applied in order to have better quality crystals (higher crystal perfection and lower level of impurities). The second-crystallization crystal growth is carried starting from the crystals grown in the first crystallization, and from the scraps obtained from the scintillation elements production. The following materials are used in a typical second-crystallization process:

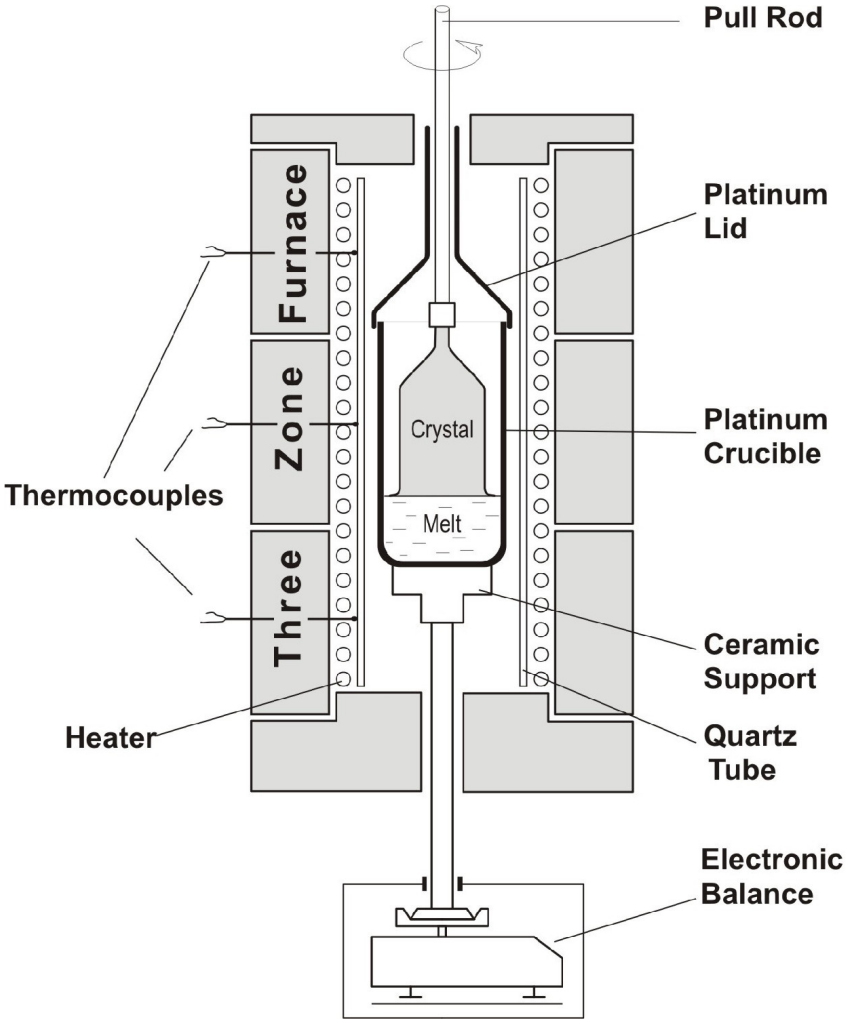


Figure 25: Scheme of the furnace for crystal growth with thelow thermal gradient Czochralski technique.

– larger parts of the crystals after the first crystallization;
– scraps of the second crystallization crystals after the cuts to produce the scintillation elements (see Sec. 4.5). The scraps are etched by ultra-pure water to a ≥ 10 μm thick remove surface layer.

Tens of Li_2MoO_4 and $Li_2{}^{100}MoO_4$ crystals have been grown by the described technique [73].

4.5 Scintillation elements production and surface treatment

Grown crystal boules are subject to a visual inspection performed in a dark room using a collimated light source (laser pointer) to localize scattering centers. With the goal of minimizing the presence of scattering defects, this allows evaluation of the geometry and position of the scintillation element that can be cut from the ingot.

As a first step of crystal processing, the crystal boule is fixed mechanically on a holder without using any resin or other gluing material in order to avoid dissolving the resin or the glue in the organic liquids used in the cutting process. This also minimizes the pollution of the scraps after the cutting process.

Crystal boules are cut with strip tape with a diamond layer applied at its end using high purity kerosene as a coolant. The coolant liquid with crystal sludge is collected in a plastic tub to save as much of the enriched material as possible.

The obtained crystal bars are glued on a glass plate with a thin layer of organic resin. Cylindrical shapes are obtained by cutting the crystal with a tubular drill with a < 1 mm thick diamond tip, while parallelepiped shapes are cut with a wire-saw. In all cases, kerosene is used as a coolant liquid.

The shaped crystals are further polished using an emulsion of silicon carbide powder and vacuum oil as a slurry. The sludge produced at this stage is highly contaminated, but of limited amount. Therefore, it is not reprocessed.

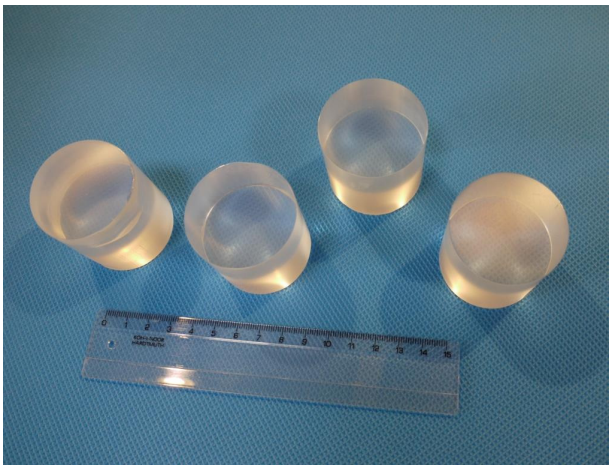


Figure 26: $Li_2{}^{100}MoO_4$ crystal produced for the CUPID-Mo pilot experiment.

The final polishing is carried out using radiopure silicon oxide abrasive powder and vacuum oil. Polishing is carried out on synthetic fabric. A layer of several tens of micrometers is removed. Losses at this stage are almost negligible. Nevertheless, even in this case residuals could be collected for the recovery of enriched Mo.

An example of $Li_2{}^{100}MoO_4$ crystals produced for CUPID-Mo is shown in Fig. 26.

4.6 Enriched ^{100}Mo recycling

Some methods for the recovery of isotopically enriched molybdenum both from the crystal growth residues and the mechanical treatment scraps have been developed in the last few years. Large crystal residues and trimmings are grinded before being placed into the crucible of the growing set-up. The scraps obtained from machining are fired to remove traces of organic compounds (kerosene, resin, etc), and then dissolved and filtered. The solution is evaporated to obtain a solid precipitate. The obtained Li_2MoO_4 powder is decomposed by acid to molybdic acid (H_2MoO_4). Molybdic acid is then annealed to molybdenum oxide (MoO_3). The molybdenum oxide is purified with the procedure described in Sec. 4.2.1. The sublimation process is repeated two-three times depending on the MoO_3 contamination level. The recycling process recovers $> 90\%$ of the molybdenum from scraps of different origin.

4.7 Other possible crystal growth methods

Alternative crystal growth techniques are under investigation for the large scale production of Li_2MoO_4 crystals for CUPID. These include the ordinary Czochralski crystal growth and the Bridgman method.

4.7.1 Ordinary Czochralski crystal growth

The French ANR-funded R&D project CLYMENE aims at exploiting the ordinary Czochralski crystal growth for the production of scintillating crystals to be operated as bolometers in rare events searches. A Li_2MoO_4 crystal with a mass of 230 g was successfully grown with this method in a platinum crucible under an air atmosphere. The crystal characterization demonstrates promising radiopurity levels (Table 6) an optical transmission $\alpha_{ABS}(589nm) \sim 0.05$ cm^{-1}), and good thermal properties, with $\theta_D \sim 765$ K and no phase transition down to 2 K [76]. Above-ground low temperature tests of the material as a scintillating bolometer [76, 77] showed an energy resolution of few keV and a relative light yield of ~ 0.97 keV/MeV, possibly yielding a highly efficient α/γ separation. The R&D is continuing with the goal of developing crystal boules of > 1 kg with improved properties by means of combined numerical simulations and well-designed implementations of the Li_2MoO_4 crystals Czochralski growth process [78]. A 820 g Li_2MoO_4 crystal has already been pulled at a rate of ~ 2 mm/h and will be operated as a bolometer in the near future.

In addition, Li_2MoO_4 crystals of up to 2" in diameter, grown by the Czochralski technique, were produced by Radiation Monitoring Devices Inc. (Watertown, MA, USA). The crystal compounds were synthesized in a separate step prior to crystal growth. Transparent, colorless crystals were produced when materials of suitable purity were used. The bolometric test of the material will be realized soon at CSNSM (France).

Isotope	Contamination [mBq/kg]
^{40}K	< 40
^{226}Ra	< 0.37
^{232}Th	< 0.21
^{228}Th	< 0.27

Table 6: Radioactive contamination levels of the first Li_2MoO_4 crystal grown with the ordinary Czochralski method.

4.7.2 Crystal production by Bridgman method

Large-size Li_2MoO_4 single crystals have been recently grown with the vertical Bridgman method in the Ningbo University (China) [79] in Shanghai SICCAS High Technology Corporation (China). Commercial compounds with 3N purity of both Li_2CO_3 and MoO_3 powders were used without additional purification for the crystals production. The grown crystal boules exhibit some residual green-yellow coloration, which is most probably due to a high contamination level of transient metals. We investigated the transmittance spectra, scattering spectra, laser-stimulated luminescence spectra, and luminescence decay time of these Li_2MoO_4 crystals, and performed an above-ground bolometric test of a 20×20 mm-diameter sample at CSNSM (France), obtaining satisfactory results in terms of the performance and radiopurity. A low temperature test of a $45 \times 45 \times 45$ mm sample is also foreseen. Further R&D for the growth of radiopure Li_2MoO_4 crystals using the Bridgman method is ongoing.

4.8 Quality assurance: detector prototypes and tests

Given the CUPID background goals, the Li_2MoO_4 crystal radiopurity is crucial. Even if a dedicated protocol is defined for the quality control of the crystal production process, only a cryogenic test can determine if the final crystals are suitable for the experiment. Therefore, following the CUORE example [80], cryogenic measurements will be perform to test random samples from each batch of the Li_2MoO_4 crystal production. Each test will be performed using a mounting scheme as similar as possible to a floor of the final CUPID detector, and operated for several weeks in order to test both the bolometric performance and the compliance of the crystals to the required radiopurity specifications.

5 Phonon and light sensors

In this section we discuss the sensors for both the heat and light detection. In CUPID, the signals consists of a phonon pulse induced in either the Li_2MoO_4 crystal or the Light Detector (LD) adsorber, and read-out by dedicated sensor. The most mature sensor technology is represented by Neutron Transmutation Doped (NTD) germanium thermistors, consisting of a small Ge crystal whose resistance rises sharply as the temperature decreases. Possible alternatives are Transition Edge Sensors (TES), in which a superconductive film is kept within the normal-to-superconducting transition, or microwave Kinetic Inductance Detectors (KID), which measure the change of the kinetic inductance of a superconductive element following the absorptions of athermal phonons.

The sensor baseline for CUPID, both for the Li_2MoO_4 crystals and the light detectors, consists of Ge thermistors, although TESs and KIDs are under study as possible light detectors for their superior signal-to-noise ratio and speed.

Based on the experience gained in the framework of the CUPID R&D projects, we selected NTDs for the readout of both the heat and light channel. The LDs consist of a thin Ge wafer acting as an absorber, coupled to an NTD. The features and the performances of such LDs satisfy the requirements for CUPID, with the advantage of exploiting the same electronics and the wiring system already implemented in CUORE. Several lines of R&D are still underway to develop NTDs with Neganov-Luke amplification, TES, and KIDS, for their higher sensitivity and faster response. To complement the light detectors, R&D on the optimization of the light collection and of the mechanical supports are being carried out.

In this section we first describe the NTDs and the heaters used for the offline stabilization of the recorded data. Second, we detail the various LD technologies. Finally, we illustrate the optimization of the light collection and of the LD coupling to the thermal bath.

5.1 Neutron transmutation doped Ge thermistors

NTDs have resistance values in the 1–100 MΩ range at their operation point, which is tuned in the 10–20 mK range for CUPID. They are biased at constant current and respond with a voltage pulse to a temperature change.

Nuclear transmutation induced by a thermal neutron flux is the best technique to achieve uniform doping in the bulk of a semiconductor. The target neutron dose for the CUPID bolometers is about 4.3×10^{18} n/cm^2. We envision a specific NTD production for CUPID, which will exploit the experience developed in CUORE and its precursors. We will irradiate several Ge wafers in a nuclear reactor using slightly different doses to fine tune the NTD response. Hundreds of individual thermistors can be typically extracted from each wafer. We will select the NTDs with the correct resistance-temperature behavior through a campaign of low-temperature characterization. This can be performed in several above-ground facilities available to the CUPID collaboration. The baseline geometry for the heat-channel NTDs is $3 \times 3 \times 1$ mm, with two metalized 3×1 sides separated by 3 mm for wire bonding. The mass of this sensors is about 50 mg. NTDs with these dimensions were already adopted in CUORE, CUORE-0, and Cuoricino. As for the LDs, smaller NTDs are required to increase the sensitivity. In fact, the heat capacity of the Li_2MoO_4 crystal dominates that of the NTD, while the opposite is true in the case of LDs, due to the small mass ($\sim$1 g) of the Ge wafer. In this case, therefore, the mass of the NTD plays an important role. Based on the lessons learned in CUPID-0, CUPID-Mo, and related R&D, we plan to employ NTD sensor for the LDs with a mass of about 5-10 mg and the same contact distance as the NTDs for the heat channel, but the contact cross section modified accordingly.

5.2 Heaters

A critical issue in operating bolometric detectors over long periods of time is keeping their response stable despite the unavoidable temperature fluctuations of the cryogenic setup. In CUORE, CUPID-0, and CUPID-Mo this is achieved using a pulser that periodically delivers a fixed amount of energy (through the Joule effect) into the bolometer by means of a resistor thermally coupled to it, generating a pulse as similar as possible to a signal due to particle interactions [81]. The off-line study of the variation of the detector response for the same energy deposition, due to the cryogenic instabilities, can be used to correct their effects.

In CUORE the heating element used to deliver the Joule heat pulses consists of a resistive device, called simply a heater. It is made up of heavily doped semiconductor material (well above the metal-to-insulator transition). Square voltage pulses are injected into the devices with a programmable pulse generator, tuning the amplitude and the time width so as to develop a few MeV thermal energy in the

Table 7: Performances of NTD Ge-instrumented LDs based on 44.5×0.175 mm Ge wafers. The results are from CUPID-0 (currently running), LUMINEU (completed), and CUPID-Mo (recently started). The most recent results achieved in the framework of the CUPID R&D program are quoted as well. All values correspond to the harmonic mean. The volume of all NTDs is comprised between 0.5 and 2.8 mm^3, and their maximum length between 2.2 and 3 mm.

	CUPID-0		**LUMINEU**	**CUPID-Mo**		**CUPID R&D**
	[86]	[30]	[27]	commissioning	upgraded	[87]
SiO coating	Single side		Single side	Double side		None
Operated detectors	6	31	4[a]	17[b]	17[c]	1
Measurement time [yr]	0.1	2	0.3	0.2	0.3	0.1
Temperature [mK]	20.0	17.5	17.0	20.5	20.0	15
NTD R_{work} [MΩ]	0.8	4.2	0.7	1.2	0.8	1.5
Rise time [ms]	1.8	3.5	2.0	0.8	1.2	0.8
Decay time [ms]	5	7	13	6	13	1.6
Signal [μV/keV]	1.3	–[d]	1.5[e]	1.2	0.96	3.9
Baseline RMS [eV]	41	–[d]	35[e]	167[f]	58	20

heater (see Section 3.8.3). The details of the fabrication and characterization of the CUORE heaters can be found in Ref. [82]. We envisage a similar production for the CUPID experiment.

5.3 Baseline technology: Ge light absorbers with NTD sensors

Germanium wafers instrumented with NTDs are one of the most well-established technologies for the detection of scintillation light in cryogenic experiments [36, 83, 84]. The NTD readout of the LDs allows us to take advantage of the electronics and the wiring system already implemented in CUORE. The long-standing experience acquired in the framework of the bolometric $0\nu\beta\beta$ decay experiments LUCIFER [85], which is now renamed as CUPID-0 [30, 86], LUMINEU [27, 39], and its extension CUPID-Mo [17], allows us to reach very high performance in terms of energy resolution, stability, reproducibility, and reliability. The performance of the LDs developed by the mentioned collaborations are summarized in Table 7. The recent CUPID R&D results on development of a fast Ge-based optical bolometer [87] are also listed in Table 7 and illustrated in Fig. 27.

The baseline design for the CUPID light detectors is a disk-shaped pure Ge wafer with double-sided SiO anti-reflecting coating, instrumented with NTDs. Ge substrates, provided by UMICORE Electro-Optic Material (Geel, Belgium), are double side polished wafers with a 50 mm diameter and an average thickness of 175 µm, with an impurity concentration below 2×10^{10} atoms/cm^3. Prior to the light detectors construction, each wafer will be coated on both sides with a 70 nm SiO anti-reflecting layer [30, 88], which enhances the light collection by a factor of ~ 2 [88]. A small NTD, with a mass of 10 mg or less, will be glued on the Ge surface using the same gluing tools as the main Li_2MoO_4crystals. To minimize the $1/f$ noise in sliced NTDs faced over the CUPID-Mo commissioning, it will be necessary to perform a dedicated polishing of thermistors as done in CUPID-0. The use of ~ 1 mg NTDs would yield a faster response, further increase the signal amplitude, and reduce the baseline noise [39, 89]. The baseline design for the Ge wafer holder consists of PTFE clamps and a copper housing. The thermal link to the heat sink is provided by 25-µm-diameter gold bonding wires, which also provide the electrical connection with the NTD.

5.4 Alternative Options

5.4.1 Neganov-Luke-assisted NTDs

Standard NTD-equipped Ge or Si-absorber-based light detectors can be upgraded to exploit the so-called Neganov-Luke amplification mechanism [90] by adding a set of electrodes on the absorber surface(s)(NL-NTD, Fig. 28), in order to apply a static electric filed to the semiconductor. The realization relies on well-assessed evaporation, sputtering, and ion implantation techniques.

Using this amplification mechanism, typical performances reached are of 10-20 μV/keV responsivity and 10-20 eV FWHM baseline resolution under grid bias up to 70 V (300 V), corresponding to a factor $\sim$10

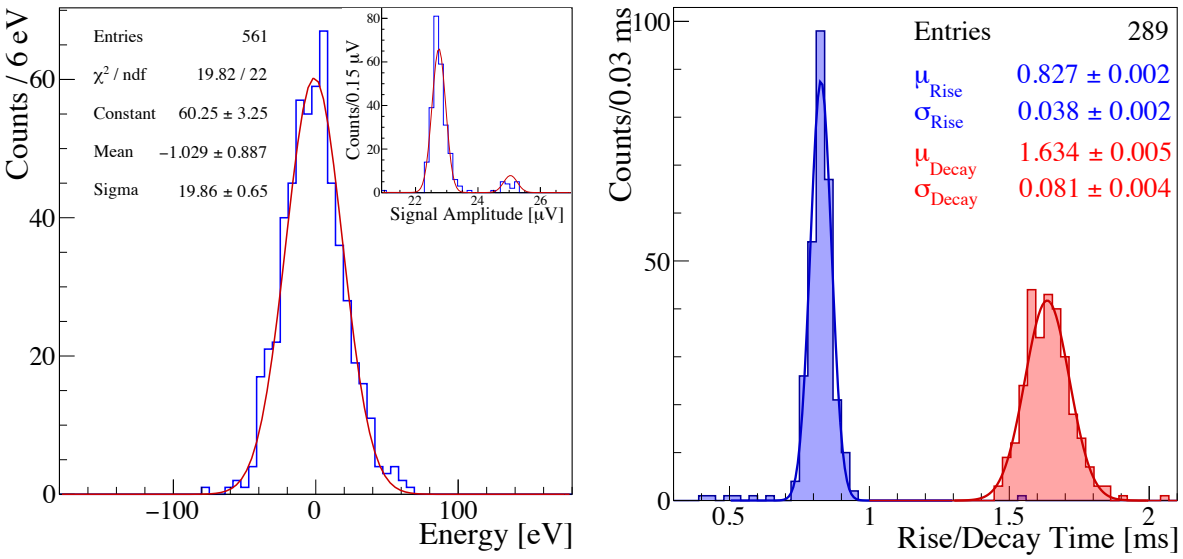


Figure 27: Performance of a Ge-LD tested at LNGS in the framework of the CUPID R&D program [87]. Left: energy distribution of the random sampled noise. The width of the distribution (σ = 20 eV) represents the baseline energy resolution of the Ge-LD. The upper inset shows a ^{55}Fe calibration spectrum. The x-axis unit is in absolute voltage drop across the thermistor. The RMS resolution on the 5.9 keV and 6.5 keV X-ray peaks is 59 eV. Right: rise and decay times distributions for the ^{55}Fe X-rays.

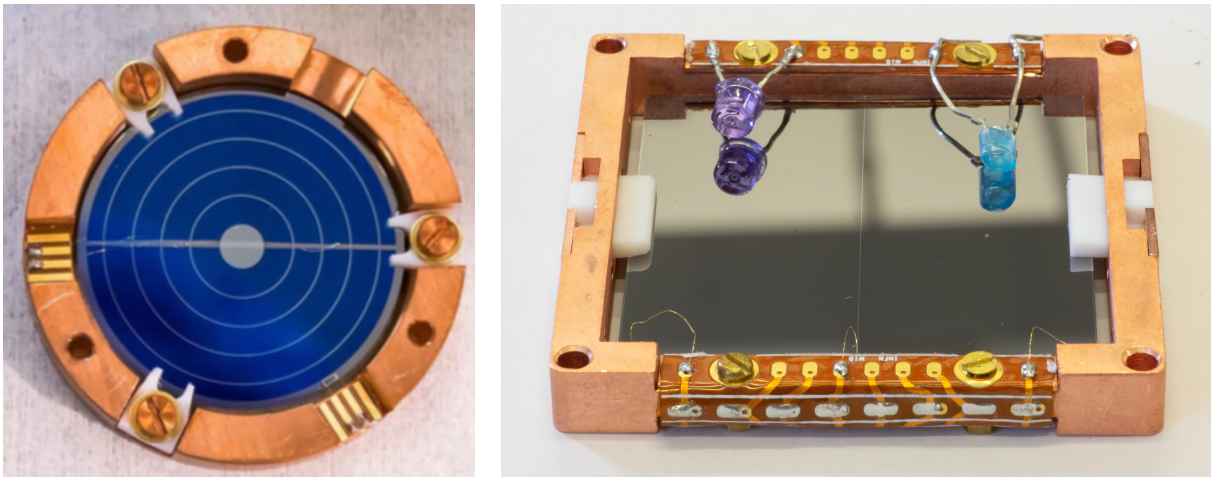


Figure 28: Left – picture of a NL-NTD base germanium light detector. The absorber is realized with a 44 mm-diameter, 175 μm-thickness high purity germanium wafer. Concentric annular electrodes are deposited on the surface, which is then coated with a thin SiO (blue-ish) layer to enhance the photon absorption in the visible wavelength. Right – a picture of a NL-NTD base silicon light detector. The absorber is realized with a 50×50 mm, 625 μ, high-resistivity silicon. Electrodes of different geometries can be realized by ion implantation to realize ohmic contacts.

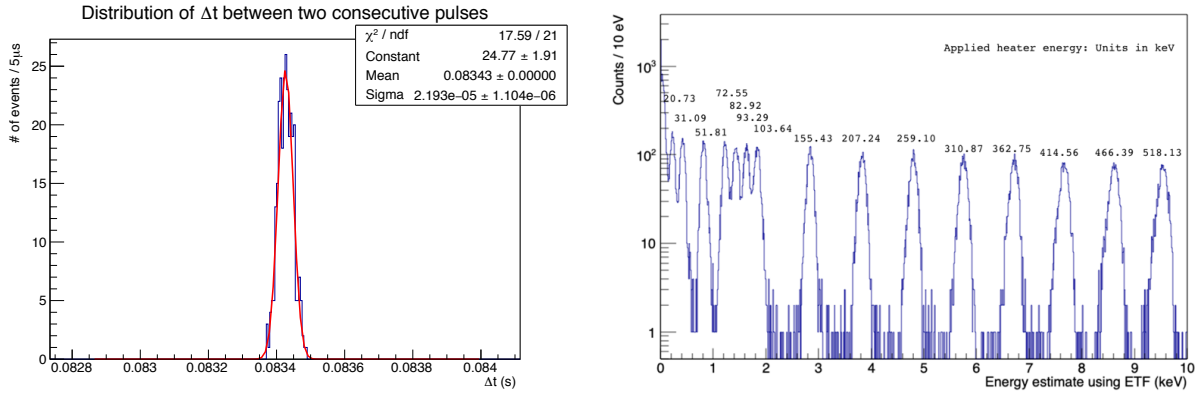


Figure 29: Left – timing resolution of an IrPt sensor at $T = 32\,\mathrm{mK}$. Using the deposited Pt resistor, pulses of constant energy with a fixed separation time are deposited into the Si wafer. A reconstruction of the time between the pulses shows a timing resolution of $\Delta T \sim 22\,\mu\mathrm{s}$. Right – reconstructed energy response by computing the energy removed through the TES via electrothermal feedback. This is proportional to the integral of the TES pulse. Each peak is labeled with the corresponding energy deposited into the Si wafer by the Pt resistor.

(50) improvement in the signal-to-noise ratio with respect to the standard Ge (Si) detectors. Several NL-NTD prototypes of about 15 cm^2 (up to 25 cm^2 with Si) detection surface have been realized and operated several time in above-ground experiments and in underground facilities to perform R&D measurements where a specific low energy detection was required, well beyond the limit one could get with standard NTDs equipped light detectors.

The technique of the NL-NTD light detectors is now mature enough to be deployed in a large-scale experiment, allowing us to reach detection thresholds of about 10 times smaller than the standard NTD light detector. This comes with a minimal price to pay of 2 additional wires, required to bias the electrode sets.

5.4.2 Transition edge sensors

A TES is a superconducting sensor that has been used in multiple experiments since their development [91–93]. This technology is a mature option that can be used in cryogenic experiments with requirements for low noise, fast rise-times, and good energy resolution. TES devices have very small footprints compared to NTD thermistors and as a result have a significantly lower heat capacity, which leads to a shorter thermal time constant. TES time constants are further enhanced by negative electrothermal feedback [94], making these devices quite capable of meeting pile-up rejection requirements for a Mo-based CUPID design. In particular IrPt bi-layer TESes, utilizing the proximity effect [95], have shown reproducible and controllable transition temperatures [96].

Unlike NTDs, TES devices are low-impedance ($R_n \sim 540\,\mathrm{m\Omega}$), allowing for a complete electrothermal characterization of the TES by measurement of the complex impedance using varying AC input signals. This is useful for determining the TES heat capacities, thermal conductances, thermal response, and theoretical energy resolution. For the test TES devices at present, we observe rise times at 33 mK of $\sim 100\,\mu s$ with decay times of $\sim 5\,\mathrm{ms}$. The current energy threshold of these devices is ~ 10 eV. By sending $20\,\mu s$ voltage pulses across the Pt resistor we can deposit a known amount of energy into the Si wafer and observe the TES response. We can use the observed TES response to compute the energy dissipated through the TES via electrothermal feedback and compare to the known energy deposition. At present there appears to be a factor of ~ 50 discrepancy between these two. A possible reason for this is that the TES is not thermalized to the Si wafer strongly; this is an ongoing area of investigation. This can perhaps be corrected via the addition of small amounts of Au to thermally anchor the TES more strongly to the Si substrate and will be investigated. If this is found to be the case, it will lead to an improved energy threshold and energy resolution for the device.

TES devices require cold-stage amplifiers, with SQUIDs being the preferred devices to use for this purpose. SQUIDs introduce an extra heat load via the power dissipation during their operation ($\sim 1\,\mathrm{nW}$ per SQUID) along with associated cabling. In order to minimize the total cooling power required, frequency division multiplexing of the TES devices can be implemented. This requires the addition of an inductor and capacitor in series with a TES (as close as possible to avoid parasitic inductance). By tuning

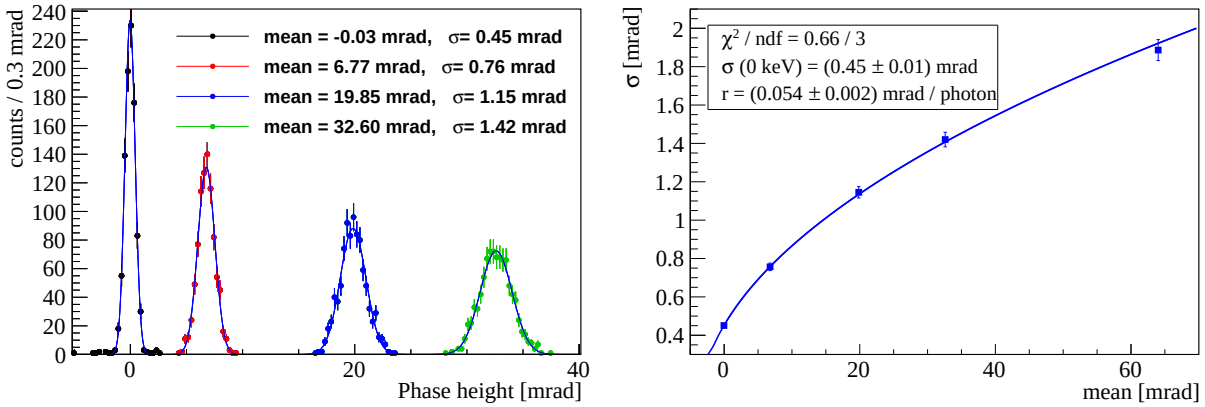


Figure 30: Left: histograms of pulse heights in the phase readout for light signals of different energies. Right: standard deviation σ versus mean m of the Gaussian distributions shown in the left panel. The plot includes one more point at 65 mrad not shown in the left panel to not compress the scale for the other distributions. The curve is well described by the Poisson statistics of photons. The resolution at zero amplitude corresponds to 25 eV RMS. See Ref. [101] for more details.

the values of L and C for each TES, a network of RLC filters is formed with each particular RLC filter allowing only a specific AC bias frequency through. This technique has been employed successfully with CMB experiments with active R&D to implement multiplexing factors > 100 [97]. For CUPID, a more modest multiplexing factor of ~ 10 is enough. At present the development of both operating and readout electronics for the frequency division multiplexing are proceeding. TES devices are a mature technology used in rare event searches for dark matter and in CMB experiments. Additionally, high multiplexing factors are already demonstrated in CMB experiments. This, combined with the intrinsically fast time constants, low noise, and good energy resolution, make TES an appealing alternative.

5.4.3 Kinetic inductance detectors

KIDs have been successfully applied in astrophysics searches providing superb energy resolution and natural multiplexed readout [98]. Because the active surface of these devices is limited to few mm^2 they can be operated as cryogenic light detector in $0\nu\beta\beta$ search only exploiting the phonon-mediated approach, proposed by Swenson et al. [99] and Moore et al. [100].

In such an approach, KIDs are deposited on a large insulating substrate featuring a surface of several cm^2. Then, the light emitted by cryogenic calorimeters interact with the substrate producing phonons, which travel within the material until a small fraction of them (5-10 %) are absorbed by a KID.

Exploiting the phonon-mediated technique, the CALDER project [102] realized a cryogenic light detector using a 2×2 cm^2 Si substrate 300 μm thick monitored with one aluminum KID. The detector showed a baseline energy resolution of about 80 eV RMS, constant in a temperature range starting from 10 mK up to 200 mK [103]. Moving from Al to more sensitive superconductors, such as AlTiAl multilayer, the baseline energy resolution has improved up to 25 eV RMS [101]. The high energy resolution of this prototype allowed us to obtain a solid estimation of the detector performance exploiting an absolute energy calibration based on the Poisson statistics of the photons absorbed into the substrate as shown in Fig. 30.

A very important feature of KIDs is their fast time response as shown in Fig. 31. The typical rise and decay time are $\sim 10^2$ times faster than NTD Ge thermistors, substantially increasing the capability to reject pile-up events. This would allow us to further suppress the background coming from the $2\nu\beta\beta$ pile-up events in ^{100}Mo-enriched cryogenic calorimeters. Furthermore, exploiting sapphire substrates instead of silicon, KIDs results are barely affected by the mechanical vibrations induced by pulse tube refrigerator. This is shown in Fig. 32 where an increase of the detector noise at low frequency is visible when the pulse tube is operating only for Si substrates. Although this effect was observed in all the sapphire substrates measured, a clear explanation of this experimental evidence has not been yet formulated. In summary, in addition to offering a sensitivity competitive with the NTDs, KIDs provide a stronger reduction of the background events coming from pile-up thanks to the faster time response and overcome the problems caused by the mechanical vibrations induced by pulse tube refrigerators that, in NTD- and TES-based detectors, could lead to a worsening of the baseline energy resolution.

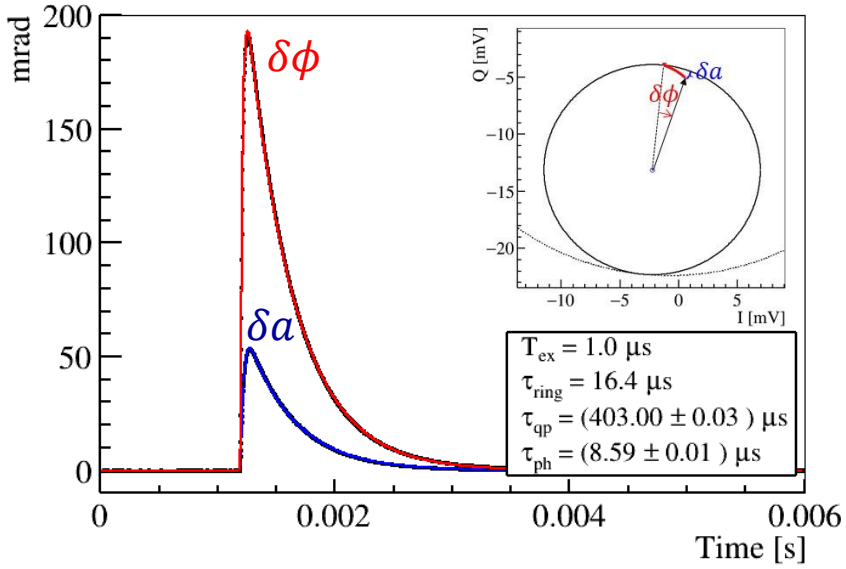


Figure 31: Phase (red) and amplitude (blue) variation measured from the center of the resonance loop induced by optical pulses produced with a 400 nm LED lamp located at room temperature and routed inside the cryostat by an optical fiber. The photon burst had a time duration of 1 μs.

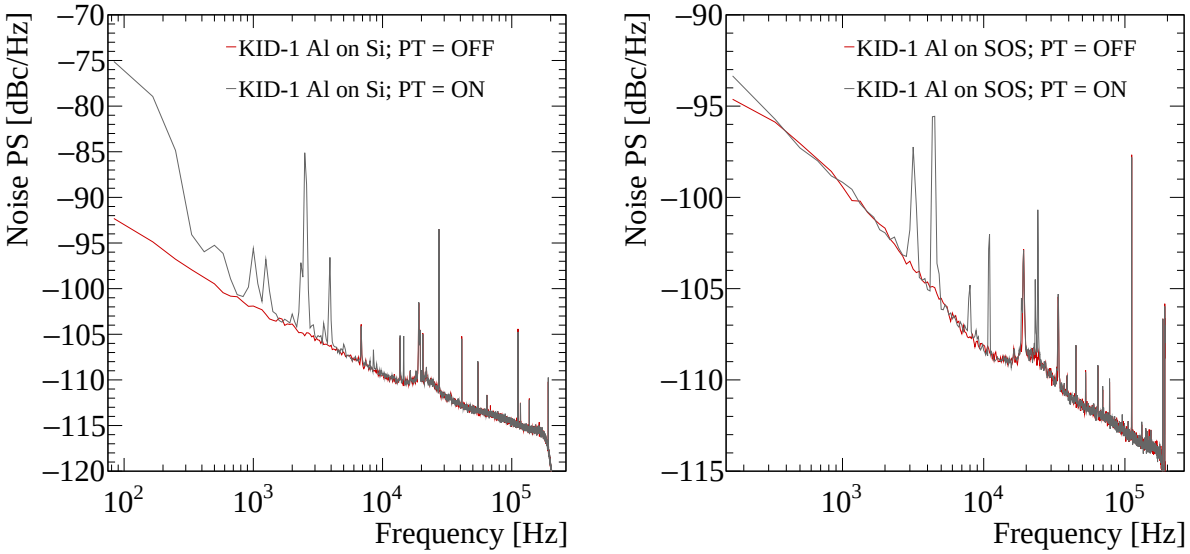


Figure 32: Noise power spectra measured for the same Al resonator evaporated on Si (left) and silicon on sapphire, i.e. SOS, (right) substrates with pulse tube off (red line) and on (black line). The noise increase at low frequency caused by the vibrations induced by the pulse tube is visible only for Si substrates.

5.5 Light collection optimization

In order to relax the constraints on the light sensors, there is an active R&D program for the improvement of the light collection efficiency by means of geometry [104], reflective housing [105], and anti-reflective coatings of the light detectors [106, 107]. The R&D also focuses on careful study of the optical characteristics of the crystals [108]. In general, the bolometric technique poses a stringent constraint on the detector design since a bolometer can only be coupled by a weak thermal link and one cannot employ refractive index matching to guide the light to its detector. Hence, with the interface between the cryostat vacuum and the crystal, light trapping due to total internal reflection can lead to a significant fraction of signal loss. Furthermore, an improvement of the light collection has to be weighed against drawbacks like the loss of coincidence information for short-range particles with a passive reflective foil between the crystals or the possibility of extra backgrounds from radioactive contamination in the additional passive material.

The light yield of large size Li_2MoO_4 crystals (⌀ 44 mm × h 40 mm) with 3M RMF VM2000/VM2002 or Enhanced Specular Reflector Films and a SiO antireflective coating on the Ge light detectors has been measured in several single crystal and few crystal prototype experiments [13, 109–111]. The light yields obtained for events around the Q-value of ^{100}Mo range from 0.7-1 keV/MeV, and are expected to be of similar magnitude for the CUPID baseline design of (⌀ 50 mm × h 50 mm) Li_2MoO_4 crystals. Preliminary results from twenty detectors (⌀ 44 mm × h 45 mm, but one of ⌀ 44 mm × h 40 mm) currently operated in the CUIPD-Mo demonstrator at LSM confirm and exceed these previously achieved light yields. As the light yield of 1 keV/MeV is at a very comfortable level for particle discrimination, current R&D is focused on evaluating if sufficient particle discrimination can be maintained while simplifying the detector design for CUPID. A cryogenic test with 45 mm cubic crystals with and without reflective foil is in preparation for mounting and underground operation at the LNGS. An additional effort to complement existing measurements of the optical properties of Li_2MoO_4 [12, 112, 113] with an absorption length measurement at cryogenic temperature is in preparation. Monte Carlo simulation codes to simulate the expected light yield of Li_2MoO_4 have been adapted from previous studies [114] and have already been used successfully for the simulation of the light yield in TeO_2.

5.6 Thermal and mechanical support

The baseline energy resolutions achieved by massive low temperature calorimeters are a few orders of magnitude worse than theoretical predictions. It has been pointed out in previous work [115] that this effect can occur when there is a mismatch between the signal and sensor bandwidths. If the coupling between the photon absorber and the thermal bath is larger than the thermal coupling between the absorber and the sensor, this can lead to sub-optimal collection of signal phonons in the sensor. This, in turn, leads to degradation of the energy resolution.

An ideal weak link should have an extremely low heat capacity and thermal conductance. While polytetrafluoroethene (PTFE) has been extensively and reliably used over the last decade as the weak thermal link between the absorber and the thermal bath, it does add a non-negligible parasitic heat capacity to the device, affecting its performance. We are currently working towards developing suitable alternatives that can offer better bandwidth matching for next generation detectors. A single crystal sapphire (Al_2O_3) seems to be the most ideal due to its extremely low heat capacity. One can also utilize the thermal boundary resistance between sapphire and copper (thermal bath) to further reduce the thermal coupling between the absorber and thermal bath. On the other hand, increasing the thermal coupling between sensor and the absorber using suitable number of gold wire bonds can also help tune the signal bandwidth.

However, unlike PTFE, sapphire is not easily machinable. We are looking at the feasibility of using sapphire as a support structure for the light detectors. Further testing to optimize the mounting arrangement and device characterization is underway.

6 Material selection and treatment

Materials prescreening for radiopurity and strict effective handling and storage protocols are essential to achieve the near zero background goal of CUPID. In this section we describe the treatment and handling of passive materials after selection for use in the experiment, the storage protocols to be followed for all parts, and the radioassay techniques and facilities currently available to the collaboration.

6.0.1 Surface cleaning

The aggressive cleaning procedures applied to the CUORE copper parts have proven effective in reducing the degraded α background to the target level [6, 7, 116]. At this stage of the CUPID conceptual design, we plan to maintain the same aggressive surface cleaning procedure to achieve the lowest attainable α background and minimize potential surface β background.

The copper surface cleaning procedures for CUORE were developed and executed at the Laboratori Nazionali di Legnaro of INFN, Italy. We implemented three levels of cleaning, which we designate as chemical low, chemical high, and standard CUORE protocol. The applied protocol depends on the distance of the considered copper surface to the bolometer and can be summarized as follows.

- The chemical low protocol consists of precleaning plus cold chemical etching;
- The chemical high protocol consists of precleaning plus cold chemical etching followed by hot chemical etching (Fig. 33);
- The standard CUORE protocol consists of pre-cleaning, tumbling, electropolishing, and plasma cleaning. It is the highest standard of cleaning (Fig. 33).

The steps of the standard CUORE protocol were adapted from procedures for resonant cavity production [117, 118]. The parts were extracted from the final cleaning stage in a cleanroom ISO 6 and packaged to prevent recontamination of the treated surfaces. Ultra clean reagents were not employed since the expense of supplying the large volumes needed for CUORE cryostat components was deemed unsustainable. The procedure was designed for zero-deposition of contaminant material on the treated pieces, therefore special attention was given to the manipulation of all the components in order to prevent re-contamination. The chemical plant employed for cleaning more than 7700 CUORE copper components remains in place and can be reactivated for CUPID with only a partial refurbishing. The different dimensions and structure of the CUPID copper components involve a new areas of research and development of the PTFE characteristics used during cleaning (Fig. 33). For example, care must be taken to guarantee the pieces' tolerances and the established erosion rates during the electro-chemical treatment. We envision two possible methods for PTFE cleaning:

- chemical cleaning followed by an atmospheric plasma cleaning immediately before the installation in cleanroom;
- chemical cleaning followed by an RF plasma cleaning in vacuum at Laboratori Nazionali di Legnaro.

To ensure adequate quality control, the CUPID cleaning protocol will be supported by Inductively Coupled Plasma Mass Spectrometry (ICP-MS) to obtain an immediate response on the process quality and efficacy.

6.0.2 Material handling and critical storage

The storage facilities for the experiment must provide: (i) a reduced cosmic ray flux to minimize activation of long-lived isotopes, such as ^{60}Co; (ii) a clean, radon-free environment to prevent surface recontamination of critically cleaned parts; (iii) a chemically compatible environment, e.g. a low-humidity environment for hygroscopic parts. A parts database will be maintained as was done for CUORE to track the history of each component.

Storage facilities were available for CUORE at the LNGS and at a shallower depth at Baradello, Como, in Italy. We plan to reuse these for CUPID. Underground storage will be reserved for raw materials, in particular copper, tellurium, and molybdenum. The material will be transported to above ground facilities for machining, crystal growth, and cleaning according to the need, but particular attention will be paid to minimizing the exposure to cosmic rays. Where international transportation is required, surface shipping will be used.

A dedicated Parts Storage Area (PSA) at the LNGS is needed for cleaned parts. Such a facility already exists from CUORE, and consists of a hut supplied with standard lab air. The hut has two rooms: an



Figure 33: Left – CUORE TSP plate cleaned with the chemical high protocol. Middle – CUORE tiles screws cleaned with standard cleaning protocol after plasma cleaning. Right – rendering of the sample holder used for the CUORE columns electro polishing, with the PTFE protection.

insertion/extraction work area with barcode scanner and a workstation to interface to the parts storage database. The user can scan the barcode of the incoming/outgoing part and note all relevant information. The timestamp is automatically logged by the computer. The second room consists of a bank of air-tight, nitrogen-flushed storage lockers that provide a low-humidity environment compatible with the needs of the slightly hygroscopic Li_2MoO_4. Crystal shipping will be performed using multi-bagging and silica-gel-sealing to ensure adequate protection against humidity.

We developed and followed this protocol for handling cleaned parts for CUORE. TeO_2 crystals and ultra-cleaned copper parts were stored in a triple layer of vacuum-sealed polyethylene bags. Oil-free vacuum pumps were used to prevent oil or grease from diffusing back into the bags. The bags were radio-assayed to prevent contamination of the enclosed components, leading us to choose polyethylene as it forms a good radon barrier. The triple protection provided redundant outer layers that could be removed without exposing the enclosed part. The external layer was removed after transporting the part from the PSA to the anteroom of the cleanroom. The second layer was removed when the part was transferred from the cleanroom to the assembly glove box, where the part was to be used. The final innermost layer was removed when the part was used in assembly. A unique bar code identifying the part was fixed to the outside of each layer of plastic so that its history could be tracked.

The storage area was flushed with boil-off nitrogen from a large liquid nitrogen dewar in Hall C of the LNGS. The level in this dewar was monitored by the vendor, with redundant monitoring by the CUORE collaboration, and refilled once the level reached a predefined minimum. This system has worked continuosly and reliably for several years.

For CUPID, we will reuse this storage infrastructure. Additional nitrogen-flushed storage, conceptually similar to the existing lockers, may be added to the cleanrooms for intermediate storage of partially assembled parts.

6.1 Radiopurity assessment

To contain the background counts at the levels required by the CUPID sensitivity goal, the material selection will be a crucial effort of the construction phase. In this respect, the collaboration will take advantage of the intense radiopurity campaigns already established for CUORE and CUPID-0 experiments. The infrastructures owned by the collaborating institutions will constitute the basis for the needed assay programs, while new detecting systems will be developed when the existing apparatuses do not reach the required sensitivity. The measurement campaigns will be organized into four main areas: γ ray spectroscopy to inspect contaminants in the bulk of the construction materials; Neutron Activation Analysis (NAA) for high sensitivity measurement of trace elements in the samples; ICP-MS to assess the concentration of long lived isotopes in the materials; and surface measurements to verify cleaning protocols and eventual radon progenies implantation. Details are given in the following sections.

6.1.1 HPGe γ ray spectroscopy

Several High-Purity Germanium (HPGe) detectors for γ ray spectroscopy with different sensitivities are available for material screening at the LNGS, Milano, and LSM. Many of them can be used to screen and certify the materials that will be installed relatively far away from the CUPID bolometrics, while only few of them have the required sensitivities to measure and select the most critical materials

to be mounted next to the crystals. In particular, the detectors installed in the underground low-level activity laboratory at the LNGS can achieve very high performances for ultra-low background measurements. At the radioactivity laboratories of LMS and Milano-Bicocca, very sensitive detectors for γ rays measurements are also available.

At LSM, one coaxial HPGe from Mirion Technologies is shared with the Edelweiss dark matter experiment. The integrated background between in the 40–3000 keV range is 178 counts/day and the sensitivity is of the order of 1 mBq/kg.

At Milano Bicocca, two high efficiency n-type detectors with around 100% relative efficiency realized by ORTEC are available for sensitive measurements. The experimental setup is designed to permit the use of the two detectors as a single spectrometer, increasing the detection efficiency, as well as the use of the two detectors in coincidence, allowing a high background rejection. The sample volume can be as large as 600 cm^3 without efficiency loss. The sensitivities of this spectrometer are in the range of 0.5 mBq/kg for the U and Th chains.

Additionally, one detector of BEGe type, with 50% relative efficiency and specifically configured for low energy measurements in low background conditions is also available at Milano Bicocca. Its sensitivity is in the range of few mBq/kg for the U and Th chains, with sample volumes up to 250 cm^3. The sensitivity performances can be greatly increased by coupling this detector with NAA, as detailed later.

6.1.2 Neutron activation analysis

The Milano Bicocca research group has considerable experience in NAA measurements. NAA was applied in the past to various materials like plastics and metals. An instrumental NAA allowed determination of the limits on the high-purity copper used for CUORE at a level $< 10^{-12}$ g/g for U and Th radioactive contaminants. In contrast, the actual achieved sensitivities on the plastic or organic materials are $< 10^{-13}$ g/g for U and Th, and of 10^{-14} g/g for ^{40}K. The irradiation facility uses the TRIGA Mark II research reactor located in the LENA laboratory of the University of Pavia. The reactor is sufficiently close to the Milano Bicocca laboratory where the spectrometric measurements are performed. The Bicocca radioactivity laboratory is equipped with several HPGe detectors specifically suited for such measurements. In particular, there is one HPGe configured for high sensitivity measurements on small samples. There are two very low thresholds detectors with high energy resolution for the precise measurements of the low energy γ's emitted by the activated U and Th nuclei. Finally, there is one system with an HPGe detector coupled to a liquid scintillator detector that, by means of a coincidence technique, allows a high background rejection for measurements in which many activated interference nuclei are involved.

6.1.3 ICP mass spectrometry

CUPID has access to mass spectrometry laboratories located at the LNGS and Milano Bicocca for the identification of U and Th contamination. Both labs are equipped with two magnetic sector mass spectrometers (Element XR at Milano Bicocca and Element 2 at LNGS, both from Thermo Fisher) with an ultimate sensitivity of $\sim 10^{-15}$ g/g, and two quadrupole spectrometers with a sensitivity of $\sim 10^{-12}$ g/g. Both are also equipped with all the facilities (chemical labs, distillation, and purification machines, etc) necessary to guarantee these sensitivities.

6.1.4 Surface measurements

Surface contamination on materials close to the detectors could be extremely dangerous. To certify cleaning and handling protocols of such materials, different measurement approaches are available, such as the BiPo-3 detector [119] and a few optimized large area silicon barrier detectors.

Measurements of thin materials will be performed with the BiPo-3 detector, initially developed in the framework of the SuperNEMO experiment to evaluate the radiopurity of the SuperNEMO sources [120]. BiPo-3, running since 2013 in the Canfranc Underground Laboratory in Spain, can reach sensitivities of the order of 10μBq/kg for ^{208}Tl, and 100μBq/kg for ^{214}Bi. The underlying concept of the BiPo-3 detector is to observe the ^{214}Bi-^{214}Po and ^{212}Bi-^{212}Po cascades, which emit an electron followed by a delayed α particle. The material under investigation is sandwiched between two low-radioactivity thin polystyrene scintillators, which provide a very clear time-topology signature (see Fig. 34).

Surface barrier detectors at Milano Bicocca, specifically selected for low background measurement during the CUORE construction, will be available for the certification of the surface radiopurity. The sensitivities of those detectors are of the order of 10^{-7} Bq/cm^2 for the αemitting isotopes contributing to the lower part of the U and Th radioactive chains, and of the order of 10^{-6} Bq/cm^2 for the upper

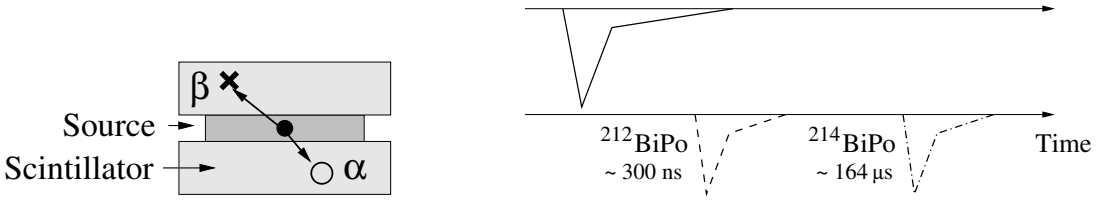


Figure 34: Schematic view of the BiPo detection principle with plastic scintillators and the time signals seen with PMTs for a BiPo event. Left – the dot represents the contamination, while the cross and open circle represent energy depositions in the scintillators by the prompt beta and the delayed signal, respectively. Right – the prompt β and the delayed α signals observed by the two scintillators surrounding the thin source.

part of the same chains. Dedicated R&D developments are under study in order to further increase the achieved specific sensitivities.

7 Background sources and suppression

7.1 Background sources and their mitigation

The $0\nu\beta\beta$ decay signature in CUPID will be a monochromatic line centered at $Q_{\beta\beta}$=3035 keV. We group sources that may produce events in the same energy region, hiding the expected peak, in the following categories:

- **External sources**: mainly environmental μs (that can't be shielded) and to a minor extent γs and neutrons (that are already efficiently shielded in the CUORE set-up);
- **Far sources**: radioactive contaminants in the cryostat (that is a system of nested copper vessel acting as thermal shields) or in the radiation shields installed inside (made of lead) and outside (made of lead and of polyethylene) the cryostat. In the following we will refer to these elements as the "shields." Only γs emitted by the shields can reach the bolometers. The condition to mimic a $0\nu\beta\beta$ signal is that the sum energies of the γs produced in the decay are larger than $Q_{\beta\beta}$. This takes into account the possibility of the simultaneous detection in a bolometer of two or more γs emitted in the same cascade. In the ^{238}U and ^{232}Th chains only two isotopes satisfy this condition: ^{214}Bi that has few γs with energy larger than $Q_{\beta\beta}$ and ^{208}Tl that contributes only through the cascade 583+2615 keV;
- **Near sources**: radioactive isotopes with Q>$Q_{\beta\beta}$ contaminating the "detector" (comprising the Li_2MoO_4 crystals, the light detectors, the light reflecting foils, the copper holder, the PTFE stands, and the 10 mK shield containing the detector array). All the particles emitted by these radionuclei can reach the bolometers, even the short range αs produced by ^{238}U and ^{232}Th and their daughters or the βs produced by ^{214}Bi and ^{208}Tl decays (Fig. 35).

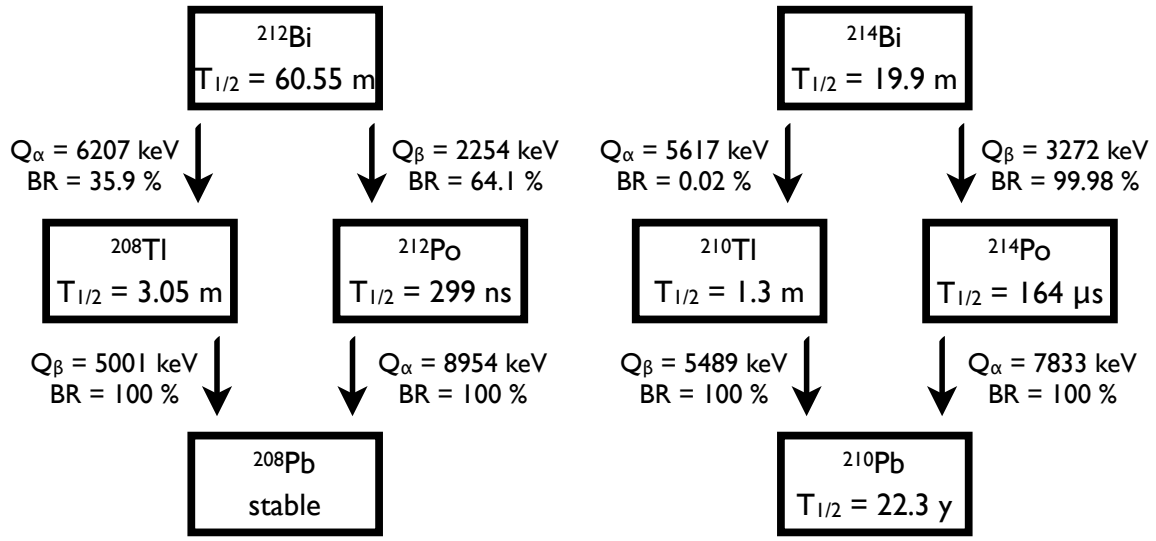


Figure 35: Decay scheme of ^{208}Tl (left) and ^{214}Bi (right). Both of these isotopes decay with the emission of high energy βs.

The CUPID detector will offer several passive and active technologies to reduce the background in the region of interest. Passive techniques involve the use of copper and lead shields. It also includes the selection, cleaning, and storage of all the materials involved in the detector construction.

Active techniques, successfully exploited in CUORE (Sec. 7.2.1) and CUPID-0 (Sec. 7.2.2), involves the capability of operating the detector in anti-coincidence, the implementation of a time-veto, and the use of particle identification. Additionally, we anticipate the installation of plastic scintillators to act as a μ veto.

Operating the array in anti-coincidence allows us to exploit the high granularity of the device to reject multi-site events, such as μs either crossing the detector or inducing showers in the shields or, again, multi-Compton interactions induced by γ rays. This technique applies, with different efficiency, to any contaminant or environmental flux, while the time-veto technique described below can be used only

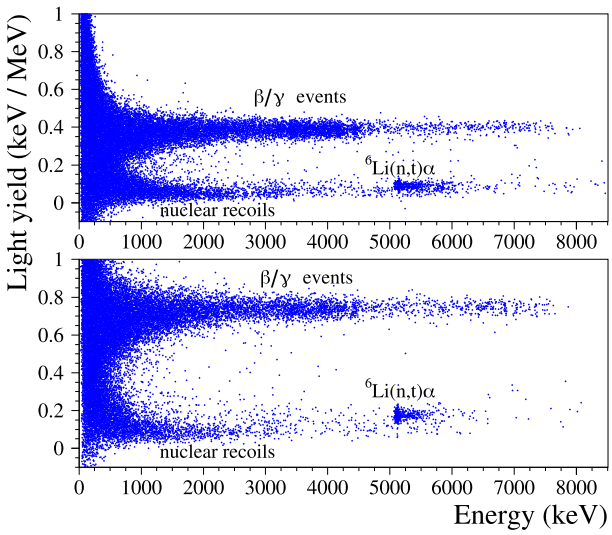


Figure 36: Light yield reported as a function of the energy released in Li_2MoO_4 crystals measured without (top) and with (bottom) reflecting foil [109]. The events shown in the plot are produced by an Am:Be neutron source.

in the case of ^{214}Bi and ^{208}Tl contaminants in the detector (since it requires one to be able to detect the α decay of the mother or the daughter).

The time-veto allows us to reduce the background produced by the β/γ decays of ^{208}Tl (Q ~5 MeV) by first detecting its mother, ^{212}Bi. This isotope decays via α emission to ^{208}Tl, which subsequently decays with a short half-life of 3.05 minutes (Fig. 35). As a consequence, the β/γ interactions produced by ^{208}Tl decay can be efficiently suppressed by opening a time-veto of few minutes after the detection of an α particle [121]. Another example of application of a time-veto is for ^{214}Bi. This isotope decays with a branching ratio of 99.98% to ^{214}Po, which subsequently α-decays with a short half-life of 163 μs (Fig. 35). Given the slow time-development of bolometric signals, these events sum up in a single pulse with energy well above the region of interest. Despite the low branching ratio of this decay mode (0.02%), ^{214}Bi can also decay via α emission to ^{210}Tl, a β emitter with a high Q-value of 5.4 MeV. In this case, it is possible to exploit the fast decay of ^{210}Tl (1.3 minutes) to reject its interactions with a time-veto. This analysis technique has not been exploited in CUORE, as the background of this experiment is dominated by α interactions. In CUPID-0, on the contrary, the background is dominated by β/γ interactions, as the α contribution can be rejected by exploiting the light yield. Thus, the implementation of the time-veto has allowed us to suppress the background by a factor 3.7 with a negligible dead-time increase.

While the described techniques are available for all the arrays of cryogenic calorimeters, CUPID will offer an additional tool for particle identification, i.e. the simultaneous readout of heat and light. The suppression of the α background via particle identification was successfully demonstrated by CUPID-0, one of the demonstrators of the CUPID technology. Furthermore, because the light signal is faster with respect to the heat signal, it will contribute to the abatement of pile-up in the region of interest (see Sec. 7.1.2).

7.1.1 α/β discrimination

The discrimination capability offered by the simultaneous readout of heat and light depends on the light output of the crystal, the light collection efficiency, and the performance of the light detector.

The CUPID experiment anticipates using cylindrical crystals surrounded by a reflecting foil and coupled to light detectors consisting of Ge disks (50 mm diameter). Even if we do not dispose of data in the final geometrical configuration, we can rely on the results obtained from past R&D activity with very similar devices: four cylindrical crystals with diameter of 44 mm and height ranging from 40 to 46 mm [109].

The crystals were measured with the reflecting foil, obtaining a comparable light yield of 0.73-0.77 keV/MeV. In a subsequent run the reflector was removed, resulting in a reduction of the light yield by a factor 2 (Fig. 36).

To understand the effect of this variation on the particle identification capability, it is useful to introduce the Discrimination Power (DP), defined as:

$$DP = \frac{|\mu_{\beta/\gamma} - \mu_\alpha|}{\sqrt{\sigma^2_{\beta/\gamma} + \sigma^2_\alpha}} \quad (1)$$

where μ and σ are the average value and RMS of the β/γ and α light distributions, respectively. Both these parameters depend on the energy and the DP in the ROI.

The requirement of a background induced by α particles lower than 10^{-4} counts/(keV·kg·yr) is satisfied for $DP(E = Q_{\beta\beta}) > 3.1$ [36].

The test-runs with four crystals without reflecting foil featured $DP = 9$, while adding the reflecting foil allowed us to reach $DP > 12$. As a consequence, in CUPID we expect the α background to be negligible in both cases.

The presence of the reflecting foil would be more conservative to guarantee a high discrimination capability: the CUPID light detectors have never been tested in the CUORE facility and in a pessimistic scenario they could perform more poorly than in other cryostats. Thus, the reflecting foil would ensure a higher light collection efficiency, compensating for potentially worse performance of the light detectors.

On the other hand, the reflecting foil would prevent the study of coincidences between adjacent crystals, which would help in background suppression. Moreover, according to the CUPID-0 background model, contaminations of the reflecting foils and holder surfaces contribute to the background in the region of interest for the double beta decay of ^{82}Se at the level of $2.1\pm0.3^{+2.2}_{-1.0}\times10^{-4}$ counts/(keV·kg·yr). This value would be similar in CUPID, pointing to an important source of background.

In view of CUPID, we are investigating possible alternatives for the reflecting foil in order to keep a high light collection while reducing the background produced by the reflector. The simplest solution consists of developing other reflecting materials, featuring contamination levels lower by about a factor 3 with respect to the one used by CUPID-0. Nevertheless, we are also considering another promising technology, in which the reflecting foil is replaced by a thin metallic coating of the crystal itself (for example, with tens of nm of ultra-pure aluminum). This technique optimizes the light collection while suppressing the background due to the presence of the reflecting foil. Furthermore, if the coating is thin enough, radioactive decays on the surface can interact in more than one crystal, enabling the study of coincidences between adjacent crystals and thus providing an additional tool for background suppression. The reproducibility and reliability of the Li_2MoO_4 coating will be tested in the next cryogenic runs in the LNGS. The merits of this solution will then be evaluated and the baseline detector design will be updated accordingly

Finally, it is worth mentioning that the Li_2MoO_4 prototypes tested in view of CUPID showed hints of particle identification using the heat channel alone (without light detectors). This feature has not yet been deeply investigated so it is not used in the background calculation presented in this document, but it could provide an additional tool for the suppression of α interactions.

7.1.2 Rejection of 2ν background

The generally slow response time of bolometers can cause accidental pile-up of $2\nu\beta\beta$ events and/or background events to contribute to the rate in the ROI at a detectable level, thus limiting the sensitivity of an experiment. This is especially true for Mo-based bolometers, given the fast $2\nu\beta\beta$ decay time of 7.1×10^{18}yr for molybdenum. Following plausible estimates [38, 122] we get for a 300g Li_2MoO_4 crystal with 100% enrichment a $2\nu\beta\beta$ pile-up rate of 3.5×10^{-4} counts/(keV·kg·yr) $\times\Delta t/[1\text{ms}]$, where Δt is the minimum resolving time of the heat channel. For $ZnMoO_4$ crystals [123], this background can be reduced to $\sim 10^{-4}$ counts/(keV·kg·yr) by using a high sampling rate of the data acquisition and by developing algorithms to find the origin of the signal with high accuracy. The discrimination capability is not only a function of Δt but also of the relative amplitudes among the two piled-up pulses and the S/N ratio of each pulse. Further improvements could be obtained by exploiting the faster time response of light detectors and the Neganov-Luke amplification that increases the S/N ratio.

The pile-up rejection efficiency is estimated using simulated light events and results about 86% for standard light detectors and 98% for Neganov-Luke ones [124]. Discrimination on the Neganov-Luke light channel can bring the $2\nu\beta\beta$ background to a level of 6×10^{-5} counts/(keV·kg·yr).

The pile-up among two radioactive background pulses or among a $2\nu\beta\beta$ decay and a radioactive decay can also contribute to the ROI, with an amount depending on the radioactive background rate. Assuming this to be 0.1 mHz, the resulting pile-up background in the ROI from radioactive sources and radioactive sources plus $2\nu\beta\beta$ is negligible [38]. Regarding cosmogenic isotopes, the global activation rates after 90 days of exposure at sea level plus one year of cool down, are below 0.1 nuclei/(kg day) (see sec. 7.4.3). This cannot give rise to significant pile-up.

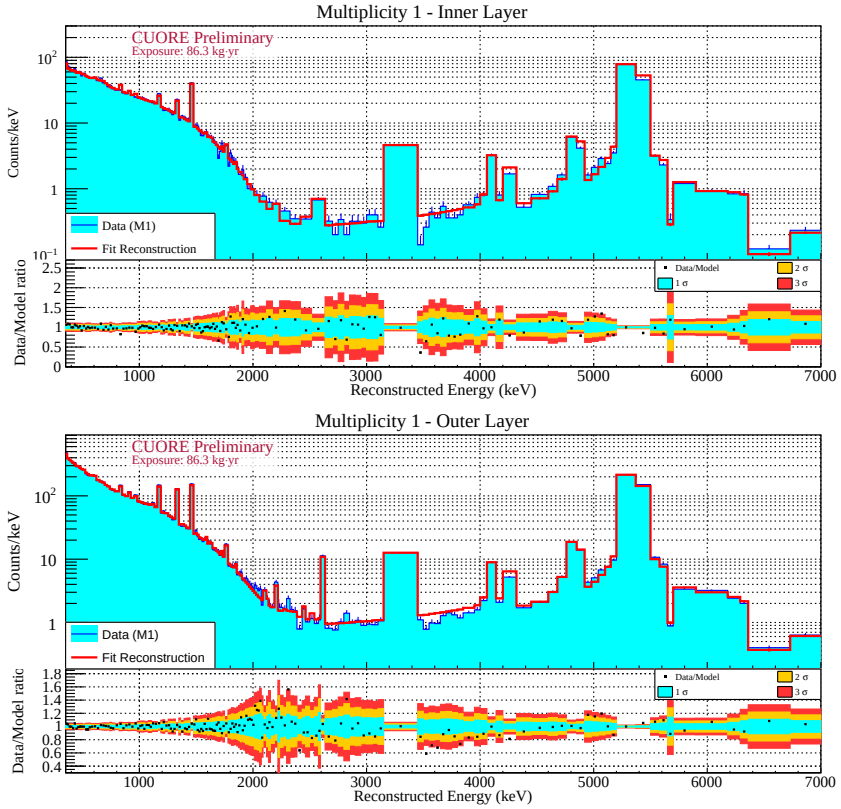


Figure 37: CUORE background reconstruction. The detectors are divided in two groups: detectors in the very core of the array (top panel) and detectors in an outer layer (bottom panel) with a "thickness" of about two crystals.

7.2 Background in CUORE and CUPID-0

Both the CUORE and CUPID-0 experiments have developed a background model (BM) able to describe their measured spectra in terms of 1) radioactive contamination coming from different parts of the detector and the experimental set-up and 2) the contribution of environmental muons (neutron and gamma contributions are negligible).

The model follows the procedure first developed for CUORE-0 [125]. A detailed description of the experimental set-up is the basis of a Monte Carlo simulation that adopts GEANT4 for particle interaction and propagation. Custom code is used to reproduce the detector, DAQ, and analysis features. Many simulations, describing all the possible (distinguishable) background sources, are generated with this code. They include surface contamination of the materials near the bolometers, bulk contamination of materials both near and far from the bolometers, and cosmogenic muons. A linear combination of these simulations is fitted to the data, having as free parameters the activity of each source. The quality of data reconstruction is illustrated in Fig. 37 for CUORE and Fig. 38 for CUPID.

Although still a work-in-progress for both experiments, the results obtained so far provide useful information for the construction of the CUPID background budget. It proves that there is a high degree of understanding of background sources. This is particularly important in the case of CUORE since we plan to host the CUPID detector in the same infrastructure.

7.2.1 CUORE background model

Here we summarize the CUORE BM results that are particularly relevant for CUPID. The left panel of Fig. 39 shows the summed contributions of the cryostat thermal shields with those of the radiation shields. This is a pure γ contribution since none of the shields directly faces the detector. CUPID will use this same infrastructure and the background counting rate will scale mainly with the detection and anti-coincidence cut efficiencies. The same is valid for the μ (induced) background.

The right panel of Fig. 39 shows the contribution due to the detector infrastructure, mainly the copper frames and the copper 10 mK shield surrounding the array. A cut on α-induced events is applied to show only the background that would be observed after α rejection (the experimental counting rate at 3 MeV is dominated by the surface contamination of copper). In CUPID this contribution will scale as the detection efficiency and the amount of copper directly facing the crystals. Fig. 40 (left panel) shows the breakdown of the CUORE counting rate predicted from the BM in the 2800-3200 keV region (only β/γ

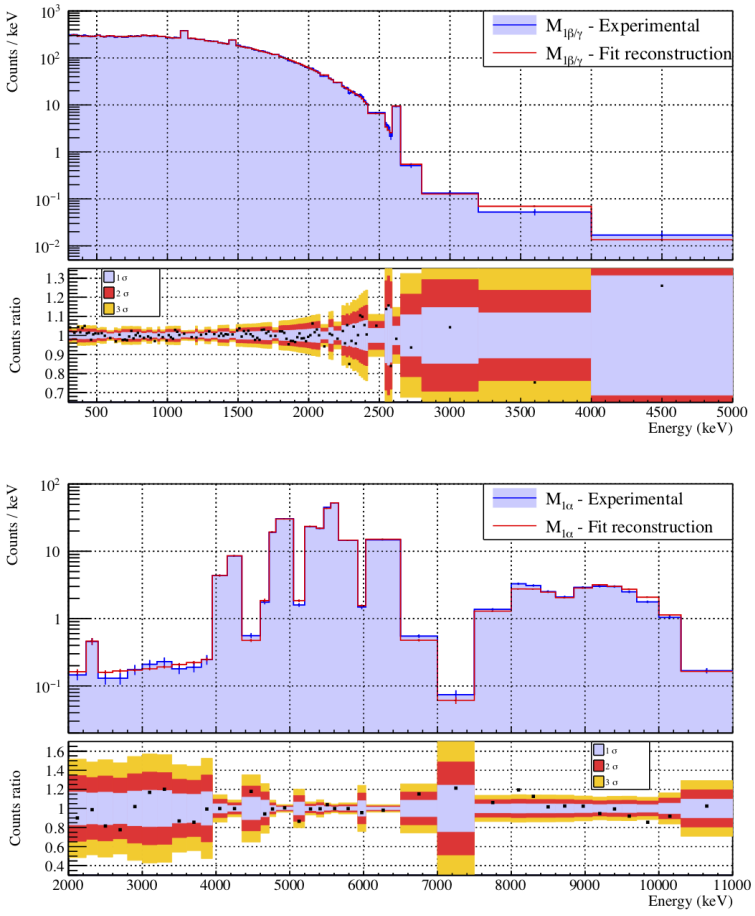


Figure 38: CUPID-0 background reconstruction. In the top panel, the spectrum of β/γ events. In the bottom panel, the spectrum of α events [121].

contribution).

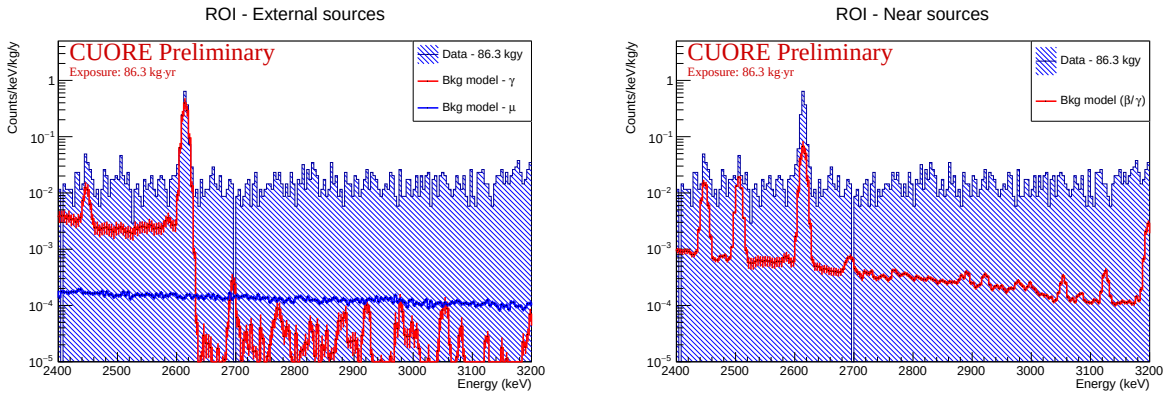


Figure 39: CUORE experimental data (filled histogram) and BM reconstructed contributions. Left – the cryostat/shields (red) and cosmogenic muons (blue) contribute only through their γ emission. Right – the reconstructed β/γ contribution of the detector, mainly due to the copper infrastructure.

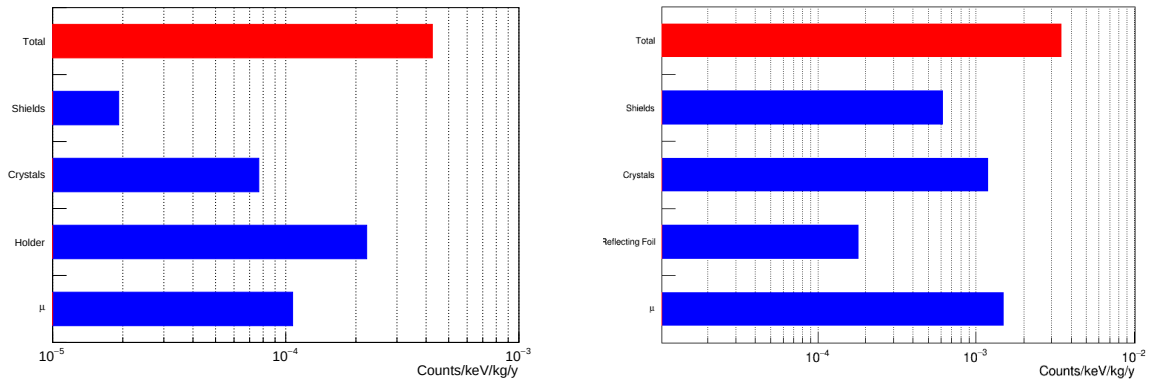


Figure 40: Breakdown of the β/γ count rate in the ^{100}Mo $0\nu\beta\beta$ region for CUORE (left) and for CUPID-0 (right). The main contributions identified by the respective BMs are shown. The integration region is 3000-3200 keV for CUORE and 2800-3200 keV for CUPID-0. In the case of CUPID-0, the $2\nu\beta\beta$ ^{82}Se contribution is not included in crystal contribution. A time-veto cut is applied both to data and to simulations in order to reject the ^{208}Tl induced background.

7.2.2 CUPID-0 background model

CUPID-0 detectors are ZnSe scintillating bolometers that allow particle identification. In the BM, the spectra due to pure α and pure β/γ events are separated both in the simulations and in the data. Particle identification becomes weaker below 2 MeV, a region dominated by β/γ and in particular by the $2\nu\beta\beta$ of ^{82}Se. Therefore all events below 2 MeV are included in the β/γ spectrum. The same kind of cut is applied on all the simulations used in the BM. Fig. 41 shows the reconstructed contribution of the α and β/γ component (left) and the effect of a delayed coincidence cut (right). This cut efficiently removes the β/γ contribution due to the ^{232}Th contamination of ZnSe crystals, which is particularly high in CUPID-0 (about 10 μBq/kg [30]). Details of the CUPID-0 background model can be found in [121].

Fig. 42 shows the CUPID-0 spectrum after α particle rejection and delayed coincidence cut as compared with the reconstructed contribution. Fig. 40 (right panel) shows the breakdown of the CUPID-0 counting rate predicted from the BM in the 2800-3200 keV region (only β/γ contribution). The delayed coincidence cut is applied both to the data and to the simulations.

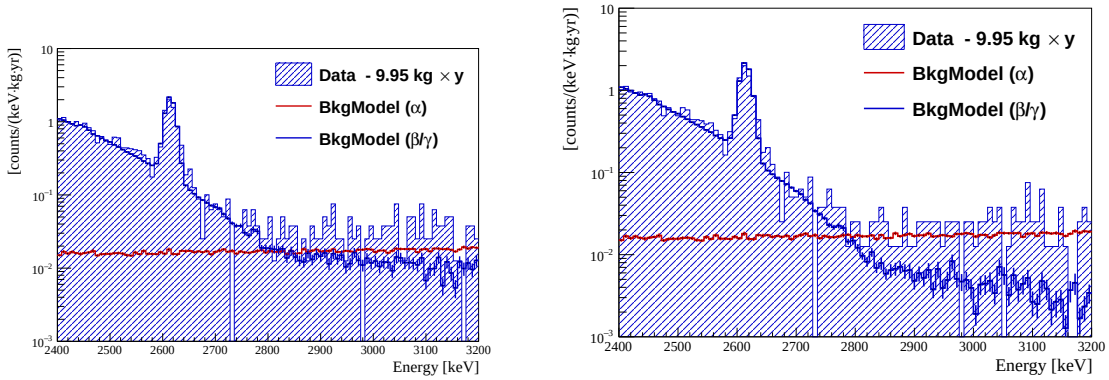


Figure 41: CUPID-0 BM reconstruction of the α and the β/γ components before (left panel) and after (right panel) the delayed coincidence cut. Figures reprinted from [121].

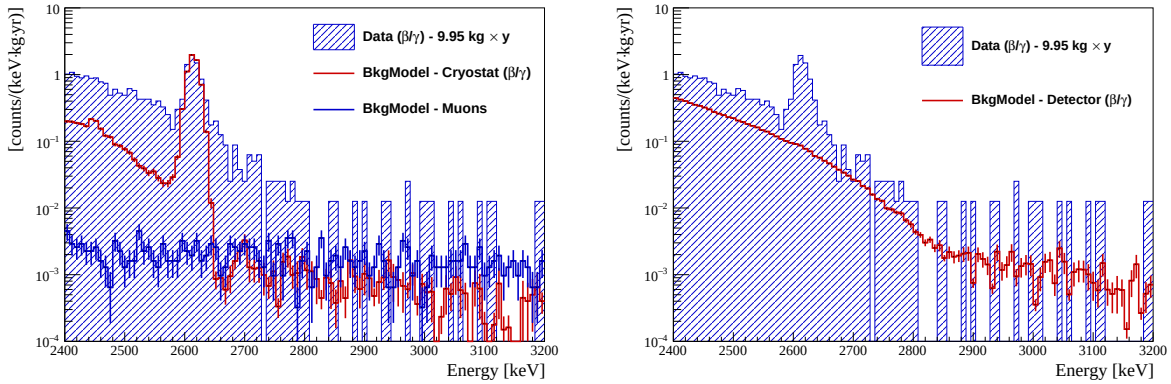


Figure 42: CUPID-0 experimental data (filled histogram) after α particle rejection and delayed coincidence cut The left panel shows the reconstructed contribution of the cryostat (red) and the cosmogenic muons (blue). The right panel shows the reconstructed contribution of the detector, mainly coming from the ZnSe crystals, reflecting foil, and holder.

7.3 Background in CUPID-Mo demonstrator

Multiple tests with enriched Li_2MoO_4 scintillating bolometers were performed at LSM and the LNGS. The tests allowed us to evaluate the background contribution of the crystals and set-up. At this stage, one of our top priorities is the evaluation of the radioactive contamination in the Li_2MoO_4 crystals and its expected contribution to the CUPID background.

We measured the radioactivity in the crystal bulk using the α spectra obtained in a measurement campaign with four enriched Li_2MoO_4 detectors (enrLMO-1, enrLMO-2, enrLMO-3, and enrLMO-4) and about 10 kg·d exposure [39] [109] [126]. Figure 43 shows the energy spectra in two enriched Li_2MoO_4 crystals

Only the peak from ^{210}Po is observed, therefore upper limits have been set for the other radionuclides in the ^{238}U and ^{232}Th decay chains. The measured activity of ^{210}Po is between 20 mBq/kg and 450 mBq/kg, depending on the crystal. However, ^{210}Po is not a potential source of background since it has no associated γs or βs with high enough energies to produce events in the ROI. Table 8 gives the measured radioactivity levels in the bulk of Li_2MoO_4 crystals.

7.4 Predicted CUPID backgrounds

In this section we discuss the CUPID background budget assuming the following geometry for the array: 118 towers with 13 Li_2MoO_4 crystals each. The crystals are cylinders with 5 cm height and diameter, face a Ge Light Detector (LD) on their top and bottom, and are surrounded by a 70 μm thick reflecting foil on the side. The array is enclosed in a copper vessel that, just as in CUORE, acts as 10 mK thermal shield. Crystals and LDs are held by ring-shaped copper frames as in CUPID-0 [30]. In the following we will refer to these copper parts as to the "holder." The cryogenic infrastructure and the radiation shield system is the same as in CUORE.

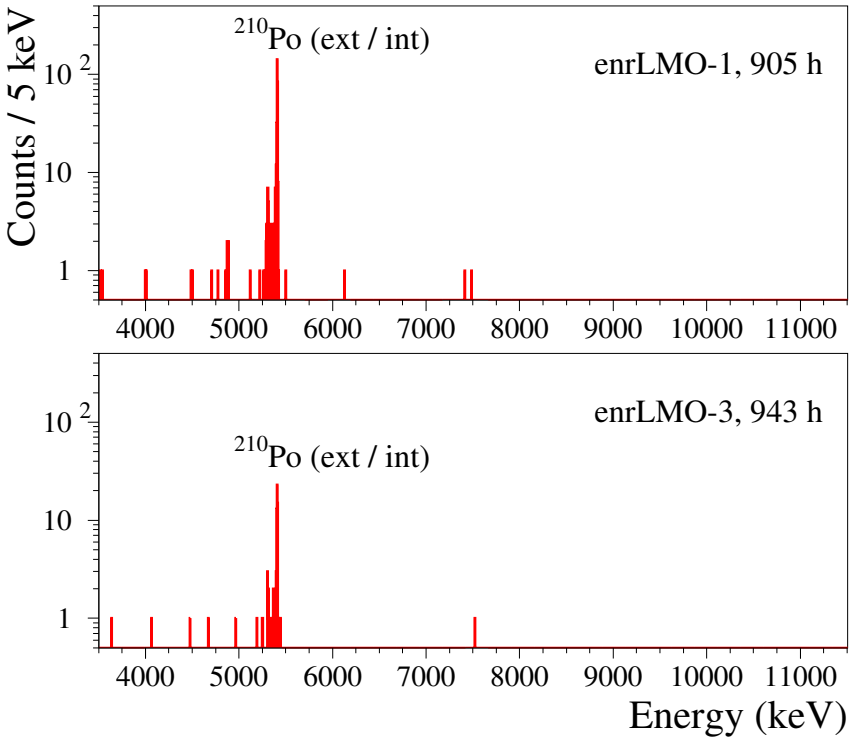


Figure 43: Energy spectrum of α events in the Li_2MoO_4 scintillating bolometers.

We implemented this detector geometry in the CUORE Geant4 simulation package, as shown in Fig. 44, and used it to evaluate the expected BI in the CUPID ROI.

We do not simulate the production and collection of scintillation light, but reconstruct the expected light signal as follows. In the simulation, we tag energy deposition in the Li_2MoO_4 crystals according to the kind of interacting particle. Therefore, for each event in a Li_2MoO_4 crystal, we know the fraction of energy deposited from β/γs, from αs, and from nuclear recoils. We use this information to evaluate the expected light signal associated to the event. In the simulations presented here, we assume a $LY_{\beta/\gamma}$ = 0.74 keV/MeV, a quenching for α of QF_α=0.209, and a quenching for nuclear recoils of QF_{recoil}=0.125. These parameters are obtained from the measurement shown in the lower panel of Fig. 36. From these same data, we extract the energy resolution of the light signal that we reproduce in the simulation applying a Gaussian smearing with an energy-dependent width. Finally, we apply a cut on the LY=Light/Energy ratio (to reject α particles) accepting only events with LY$>$ 0.5.

We note that the parameters adopted in the reproduction of the LY vs. Energy scatter plot, though extracted from a specific measurement, are representative of the average behaviour of the Li_2MoO_4 detectors. Slight changes of LY, QF, as well as of the cut adopted for α rejection do not imply relevant changes in the results discussed below. The quoted background rates refer to a 70 keV width ROI centered on the ^{100}Mo $Q_{\beta\beta}$. They are evaluated having applied the anti-coincidence cut, a time-cut that removes pile-up events occurring in a 5 sec window, and delayed coincidences occurring on the same crystal in a 900 sec window. This corresponds to about 5 half-lives of ^{208}Tl. There is no gain in using larger values since the residual background becomes dominated by the inefficiency in the parent detection.

In the following sections we discuss hypotheses and results obtained for the different background sources.

7.4.1 ^{238}U, ^{232}Th from close sources

We evaluate ^{238}U and ^{232}Th contribution from close sources simulating the chains in secular equilibrium and using the activities reported in Table 9. Since the isotopes responsible of the background rate in the ROI are mainly ^{214}Bi and ^{208}Tl, and since secular equilibrium is often broken at the ^{226}Ra or ^{228}Th level (respectively for the ^{238}U and ^{232}Th chains), it is important to keep in mind that activities bounds must be respected, not only by the progenitors of the chains, but also by their two long-lived daughters.

Below we briefly comment on the activities used for this study while in Fig. 45 we show the resulting BI.

– For the bulk of Li_2MoO_4 crystals, based on the results reported in Sec. 7.3, we have assumed a

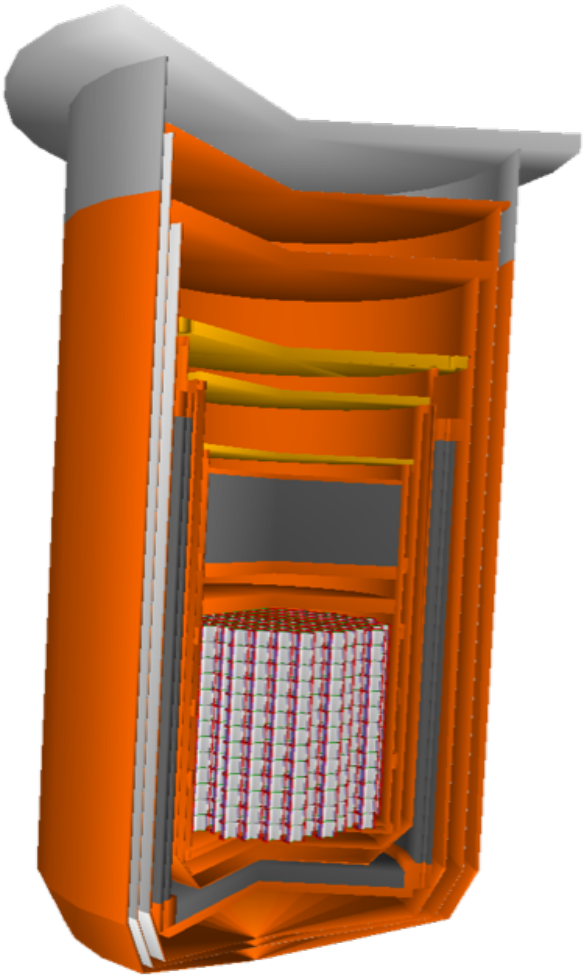


Figure 44: Geometry of the CUPID detector array with cylindrical crystals implemented in the CUORE Geant4 simulation software.

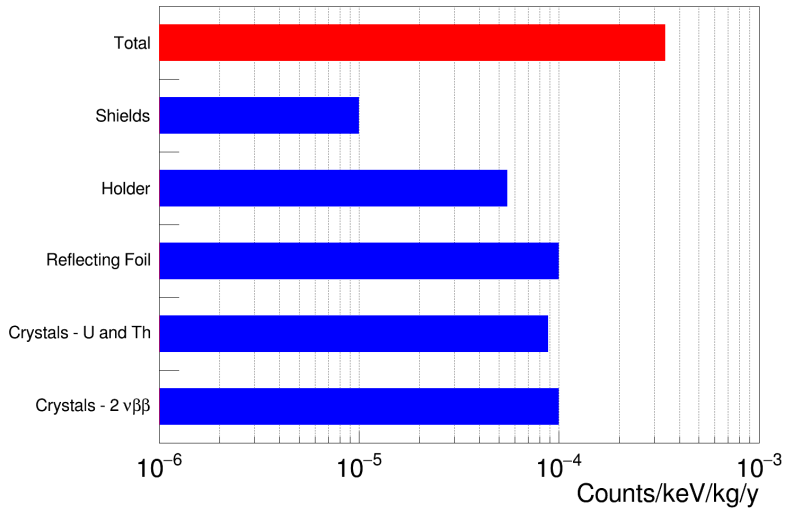


Figure 45: Breakdown of the CUPID β/γ counting rate predicted by the BM in the ^{100}Mo ROI. Here, the baseline configuration is considered. As discussed in the text, the substitution of the reflective foil with a reflective coating on Li_2MoO_4 crystals would dramatically reduce both the U and Th contributions of crystals (here dominated by surface contaminants) and that of the reflector itself.

Table 8: Radiopurity in the bulk of ^{100}Mo enriched Li_2MoO_4 crystals. Uncertainties are given at 68% CL and upper limits at 90% CL.

Activities [μ**Bq/kg**]	**enrLMO-1** 186 g	**enrLMO-2** 204 g	**enrLMO-3** 213 g	**enrLMO-4** 207 g	**Ref**
^{232}Th	<3	<11			[39]
^{228}Th	<4	<6	<3	<5	[109]
^{238}U	<5	<11			[39]
^{234}U	<7	<11			[39]
^{230}Th	<3	<11			[39]
^{226}Ra	<6	<11	<3	<9	[109]
^{210}Po	450±30	200±20	76±10	20±6	[109]
^{235}U	<5	<6			[39]
^{231}Pa	<3	<6			[39]
^{227}Ac	<5	<6			[39]
^{40}K	800±300	800±300	800±300	800±300	[126]
^{190}Pt	<3	<11			[39]

Table 9: Radiopurity levels assumed in the CUPID background model for close materials.

Material	^{238}U	^{232}Th	**Reference**
Li_2MoO_4 bulk [μBq/kg]	10	3	Sec. 7.3
Li_2MoO_4 surface 10 nm [nBq/cm^2]	3	2	[125]
Li_2MoO_4 surface 10 μm [nBq/cm^2]	0.8	<0.03	[125]
Reflecting foil surface 10 μm [nBq/cm^2]	8.7	<0.7	Sec. 7.2.2
Cu bulk [μBq/kg]	<10	<2	[125]
Cu surface 10 μm [nBq/cm^2]	14	5	[125]

contamination of 10 μBq/kg in ^{238}U and 3 μBq/kg in ^{232}Th.

- For the surface of the Li_2MoO_4 crystals, since we do not have a sensitive measurement on the Li_2MoO_4 crystals themselves, we assume the same activity measured in CUORE-0. A surface contamination is characterized not only by the contaminant concentration but also by the way the contaminant is distributed in the contaminated layer. As discussed in Ref. [125], a measurement of the density profile of surface contamination is not easy. However, experimental results in CUORE-0 (as well as in CUORE and in CUPID-0) can be satisfactorily reproduced assuming two different depths: 10 nm and 10 μm [125]. We do the same in our CUPID background model.
- For the reflecting foil, we use the results of CUPID-0 BM. Indeed, direct measurements (ICPMS and Bi-Po tracked in a scintillation detector) bound the activities of ^{238}U and ^{232}Th progenitors; the lowest part of the chain is bounded only in the case of ^{232}Th. CUPID-0 data proves the existence of contamination coming from the reflecting foil. This contamination is observed from its α emission. The BM attributes it to a ^{226}Ra (^{238}U chain) contamination. This is equally well represented by a bulk or by a surface contamination of the foil, as expected given the thickness of the material. The alternative hypotheses, namely that αs are due to a ^{210}Po contamination (therefore attributable to an excess in the ^{238}U chain of the ^{210}Pb isotopes and its daughters), is moderately rejected by the fit.
- For the copper holder, we use the surface and bulk contamination measured for the same material in CUORE-0 [125].

It is clear from Fig. 45 that the two most critical contribution are those coming from the reflecting foil and from the surfaces of crystals. Removing the reflecting foil will likely allow us to get rid of both these two contributions. In one case, it's because the background source is removed (the reflective foil). In the other, it's because the efficiency of coincidence cut will be improved (since crystals will face each other without an inert material interposed in between them).

7.4.2 ^{238}U, ^{232}Th in the cryostat and radiation shields

According to the CUORE BM, the only contaminants present in the infrastructure that may yield a background in the ^{100}Mo ROI are ^{214}Bi and ^{208}Tl in the shields and cryostat. As previously discussed, this is a pure γ contribution, since a minimum thickness of few cm of copper is assumed to shield the array from these elements. Despite the current uncertainty on the exact location of these contaminants, a safe upper limit on their contribution to CUPID BI can be set to about 10^{-5} counts/(keV·kg·yr) with the anti-coincidence cut.

7.4.3 Cosmogenic Isotopes in the crystals and materials

The interaction of cosmic rays with the crystals and holding structure leads to the production of radioactive nuclei that accumulate during the production, handling, and storage of the materials above ground [127, 128]. The amount of cosmogenic activation is the result of the properties of the target material, the cosmic ray flux and composition, the exposure time, and the cooling time (in case an underground storage follows the production). The cosmogenic activation of Li_2MoO_4 crystals was estimated using the ACTIVIA [129] code, assuming a sea level exposure of 90 days an underground cooling period of one year. Among all the materials present in the CUPID setup, only molybdenum contributes with cosmogenically activated isotopes emitting radiation with energy high enough to give events in the ROI. We assume the crystals to be 95% enriched in ^{100}Mo, with the remaining isotope being only ^{98}Mo. The only potentially dangerous activated isotopes in ^{100}Mo are ^{82}Rb, which is produced by the decay of the activated isotope ^{82}Sr, ^{56}Co, and ^{88}Y. These are also produced by the decay of the activated isotope ^{88}Zr. The activation rates after the cooldown period are of the order of 10^{-5} counts/(kg·day) for ^{82}Sr, 10^{-3} counts/(kg·day) for ^{56}Co, and 10^{-1} counts/(kg·day) for ^{88}Zr and Y. Monte Carlo simulations show that the contribution of such isotopes to the CUPID background do not exceed 5×10^{-5} counts/(kg·day). Although there are different assumptions, the results are consistent with previous calculations performed with both ACTIVIA and COSMO [130] codes [36, 131, 132].

7.4.4 Neutron-induced backgrounds

In a deep underground site like the LNGS, the dominant neutron flux is caused by the radioactivity in the surrounding rock. This consists of spontaneous fission (mainly of ^{238}U) and (α, n) reactions, with neutrons energies below ~10 MeV. The large rock overburden of the LNGS significantly reduces the cosmic ray muon flux. Therefore the muon-induced neutron flux is several orders of magnitude weaker than that attributed to the natural radioactivity, but its neutron energy distribution extends up to a few GeV [133]. The background in the ROI for a double-beta decay search may arise mainly from (n,γ) reactions or by inelastic scattering of high-energy neutrons. The (n,γ) reactions can produce γs with energies up to 10 MeV, while the neutron inelastic scattering off the elemental composition of a detector may induce several MeV, potentially populating the ROI.

CUORE features a massive external passive shield consisting of 18 cm of polyethylene to thermalize neutrons, 2 cm of H_3BO_3 powder to capture thermal neutrons, and at least 25 cm of lead to absorb γ rays. The neutron-induced background in the ROI of the $0\nu\beta\beta$ of ^{130}Te is estimated to be $(8 \pm 6) \times 10^{-6}$ counts/(keV·kg·yr) [37, 59]. The CUORE expectation could also be reasonably valid for the case of CUPID and the ROI of both ^{130}Te and ^{100}Mo.

The difference between the CUPID baseline option and CUORE in the material properties of the detector (i.e. lower density, effective Z, and crystal volume of Li_2MoO_4 than those of TeO_2), would result in a comparable neutron-induced gamma rate. Furthermore, the particle identification capability of a Li_2MoO_4 scintillating bolometer would improve the discrimination of inelastic neutron scattering-induced events. The latter are rejected in CUORE only by an anti-coincidence cut.

The difference in the detector elemental composition (i.e. the presence of ^{100}Mo and ^{nat}Li instead of ^{nat}Te or ^{130}Te), does not significantly impact the background originated from a neutron capture in a detector volume. The cross section energy dependence of (n,γ) reactions on ^{100}Mo is rather similar to that of ^{130}Te. The difference is mainly in a larger number of resonances for ^{100}Mo in the 0.2–20 keV energy range. These resonances can have up to a factor 10 larger cross section [134]. At the same time, the intensity of γs with energies above $Q_{\beta\beta}$ are about one order magnitude higher for ^{130}Te [135]. Regarding the lithium and oxygen, the dominant isotopes are ^{7}Li and ^{16}O, respectively. The intensity of their few broad resonances for fast neutron capture is about four orders of magnitude lower than those of ^{130}Te and ^{100}Mo. In all cases, the only potentially harmful daughter nucleus is ^{8}Li (Q_β = 16 MeV, $T_{1/2}$ = 0.84 s). The ^{8}Li decay occurs through a broad (Γ = 1.5 MeV) 3 MeV excited state of ^{8}B,

which disintegrates promptly into two α particles producing mixed β+α single events [136]. Considering the energy spectrum of such events [137], and the estimation of the thermal neutron flux even inside the CUPID R&D cryogenic set-up ($\leq 2.6\times10^{-8}$ neutrons/s/cm^2 [39]), the expected background in the ^{100}Mo ROI is 1.0×10^{-5} and 2.6×10^{-7} counts/(keV·kg·yr) for the 100% and 1% transition to the ^{8}B excited and ground states respectively. It is worth stressing that this background is expected to be significantly suppressed thanks to ^{6}Li(n,t)α reaction which is a factor of 1735 more probable than the ^{7}Li(n,γ)^{8}Li reaction for natural lithium (7.6% of ^{6}Li). Furthermore, a major part of the β+α events occurring in the ^{8}Li-^{8}B decays can be rejected with high efficiency using a scintillating bolometer approach [12, 39].

7.4.5 Muon-induced background

An additional background source is represented by muons interacting directly with the detectors. Most of the muons release energy in more than one crystal, thus a strong suppression of the muon background is obtained with the rejection of events with multiplicity > 1 (M1). Preliminary results from CUORE predict a background contribution of surviving M1 events at the level of 10^{-4} counts/(keV·kg·yr), as depicted in Fig. 39. These mainly come from muons interacting with peripheral crystals. We plan to further reduce this background by at least an order of magnitude with the installation of dedicated plastic scintillator panels around, above, or below the external lead shielding (Sec. 3.11). We are currently investigating the possible geometrical configurations that can fit in the CUORE setup without requiring modifications to the infrastructure. The exact suppression factor will be evaluated with dedicated Monte Carlo simulations that are currently under development. Preliminary results show that the required suppression factor is achievable even in the conservative scenario where only the sides of the shielding are instrumented.

7.4.6 Neutrino-induced background

The background induced by neutrino-electron elastic scattering (neutral current process) is estimated to be of the order of 10^{-7} counts/(keV·kg·yr) for all experiments investigating $\beta\beta$ isotope with $Q_{\beta\beta}$ above 2 MeV [138]. The charged current neutrino-nucleus interaction for the case of ^{100}Mo, characterized by the low energy threshold and the large neutrino capture cross-section [139], is expected to be on the level of 2×10^{-5} counts/(kg·yr) [140], assuming 0.4% energy resolution. This background can also be suppressed by tagging the charged current process thanks to a short half-life ($T_{1/2} = 16$ s) of the intermediate nucleus ^{100}Tc and/or multiple-hit events.

8 Phased Deployment

Bolometric experiments with a large number of individual crystals and towers are well suited for phased deployment, starting data taking with a fraction of the total isotopic mass. We foresee an option of deploying the first few towers assembled for CUPID early, while the rest of the crystals are being procured and the detectors assembled. Such phase "CUPID-I" could be deployed in a separate cryostat at LNGS, or in the CUORE cryostat if it is available. Similar to CUORE-0, which was developed as part of the CUORE project R&D and was invaluable in vetting the CUORE assembly procedures and the background model, CUPID-I phase would be an important step in the project execution plan. At the same time, a detector with mass of 50-70 kg and nearly zero background, deployed in the early 2020s, would be a leading NLDBD experiment in its own right.

The main phase of CUPID is a detector deployed in the CUORE cryostat. Its size is determined by the volume of the existing 10 mK vessel and is not limited by the available cooling power. The baseline CUPID design parameters are listed in Table 1. We assume a conservative background goal of 10^{-4}counts/(keV·kg·yr); as discussed in Section 7, this goal is readily achievable with the existing technology.

At the same time, it is instructive to consider the ultimate sensitivity of a bolometric detector not limited by the current technology and infrastructure. We consider two additional scenarios for the purposes of computing the ultimate sensitivity of the CUPID program. One is the detector deployed in the CUORE cryostat, but operating in the nearly zero-background mode, which corresponds to the background index of 2×10^{-5}counts/(keV·kg·yr). This is an optimistic "reach" goal for CUPID. As Section 7 demonstrates, reaching this background goal is possible with additional R&D: eliminating the reflective foil backgrounds, reducing the bulk and surface backgrounds from the crystals (e.g. by additional purification of Li_2MoO_4 crystals and elimination of surface backgrounds by pulse shape discrimination), and reducing the $2\nu\beta\beta$ pileup background to below 10^{-5}counts/(keV·kg·yr) level through the use of higher-bandwidth sensors.

Finally, we consider a strawman ultimate bolometric detector "CUPID-1T", consisting of 1.8 tons of Li_2MoO_4, or 1000 kg of ^{100}Mo. Such detector could be accommodated in a new cryostat approximately 4 times larger than CUORE, within the capabilities of the CUORE cryogenic systems. For optimal sensitivity, we assume that the backgrounds could be further reduced to the level of 5×10^{-6}counts/(keV·kg·yr). Such background levels are within the realm of possibility for the transition energy of 3034 keV, especially considering advances in material screening and radiopurity, and advanced high-speed, high-resolution sensors being developed within CUPID (Section 5.4.2). Such a detector would be the ultimate Phase III of the CUPID program, a bolometric detector with the sensitivity in the Normal Hierarchy of neutrino masses. In case of a discovery, such a detector could also explore other isotopes, e.g. ^{130}Te.

We summarize the parameters of the possible CUPID detector phases in Table 10. The sensitivity to various models of NLDBD are discussed in Section 9.

Table 10: Parameters of the CUPID detector in the baseline scenario, in the optimistic background scenario, and for a large bolometric detector with 1 metric ton of ^{100}Mo isotope.

Parameter	CUPID Baseline	CUPID-reach	CUPID-1T
Crystal	$Li_2{}^{100}MoO_4$	$Li_2{}^{100}MoO_4$	$Li_2{}^{100}MoO_4$
Detector mass (kg)	472	472	1871
^{100}Mo mass (kg)	253	253	1000
Energy resolution FWHM (keV)	5	5	5
Background index (counts/(keV·kg·yr))	10^{-4}	2×10^{-5}	5×10^{-6}
Containment efficiency	79%	79%	79%
Selection efficiency	90%	90%	90%
Livetime (years)	10	10	10
Half-life exclusion sensitivity (90% C.L.)	1.5×10^{27} y	2.3×10^{27} y	9.2×10^{27} y
Half-life discovery sensitivity (3σ)	1.1×10^{27} y	2×10^{27} y	8×10^{27} y
$m_{\beta\beta}$ exclusion sensitivity (90% C.L.)	10–17 meV	8.2–14 meV	4.1–6.8 MeV
$m_{\beta\beta}$ discovery sensitivity (3σ)	12–20 meV	8.8–15 meV	4.4–7.3 meV

9 Physics sensitivity and other measurements

9.1 Sensitivity to $0\nu\beta\beta$ decay

The main physics goal of CUPID is searching for $0\nu\beta\beta$ decay with a discovery sensitivity greater than 10^{27} yr in the half-life of the process, $T^{0\nu}_{1/2}$. The sensitivity scales linearly with the livetime of the measurement for an experiment with zero background, or as the square root of the live-time for a background-dominated experiment. In practice, the relevant parameters are 1) the sensitive exposure, defined as the product of the isotope mass, live-time, and total efficiency, and 2) the sensitive background, defined as the expected number of background events in the ROI normalized by the sensitive exposure. The sensitive background depends on the BI at $Q_{\beta\beta}$, measured in counts/(keV·kg·yr), and on energy resolution, which defines the ROI width. Fig. 46 shows the 3σ discovery sensitivity of CUPID for different values of the BI and energy resolutions. In order to maximize the sensitivity and make the most efficient use of the active material, the measurement has to be performed as close as possible to the zero background approximation. Fig. 46 also shows that the energy resolution is a somewhat less relevant parameter once the background is low enough.

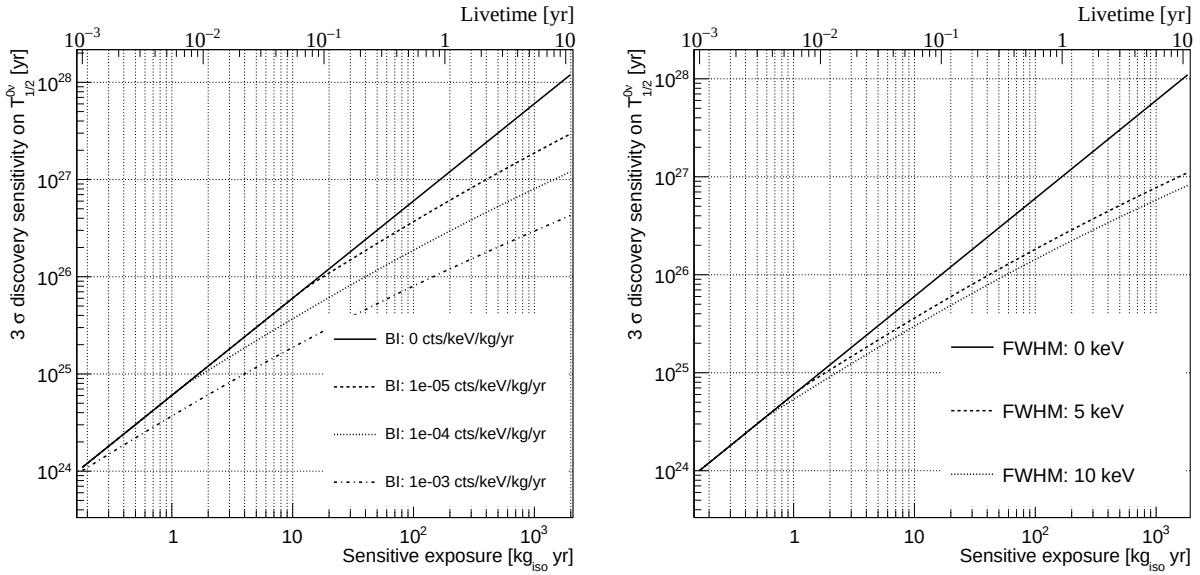


Figure 46: Left – Discovery sensitivity on the $0\nu\beta\beta$ decay half-life for an energy resolution of 5 keV FWHM and different background levels. Right – Discovery sensitivity for a BI of 10^{-4} counts/(keV·kg·yr) and different energy resolutions.

The $0\nu\beta\beta$ decay can be induced by several mechanisms [141], with the following relation between $T^{0\nu}_{1/2}$ and the parameter describing the new physics, $|f|$:

$$\frac{1}{T^{0\nu}_{1/2}} = G_{0\nu} g_A^4 \mathcal{M}^2 |f|^2 \quad , \tag{2}$$

where $G_{0\nu}$ is the phase space, g_A is the axial vector coupling constant, and $\mathcal{M}$ the nuclear matrix element (NME) relevant for the process. Under the minimal assumption that only the three known neutrinos are exchanged in the reaction, $|f|$ corresponds to the effective Majorana mass:

$$|f| = m_{\beta\beta} = \frac{\left|\sum_{i=1}^{3} U_{ei}^2 m_i\right|}{m_e} \quad , \tag{3}$$

where U is the PMNS mixing matrix, m_i the neutrino mass eigenvalues, and m_e the electron mass. The discovery sensitivities on $m_{\beta\beta}$ for several proposed next-generation experiments measuring $0\nu\beta\beta$ decay, including the CUPID phases described in Section 8, are shown in Fig. 47, assuming a livetime of 10 yr for each experiment. The final sensitive exposure of each experiment depends on its isotope mass and total efficiency. Experiments with a large isotope mass and/or high efficiency (e.g. nEXO and SNO+) have a larger sensitive exposure than experiments with a lower isotope mass, e.g. CUPID. For a given

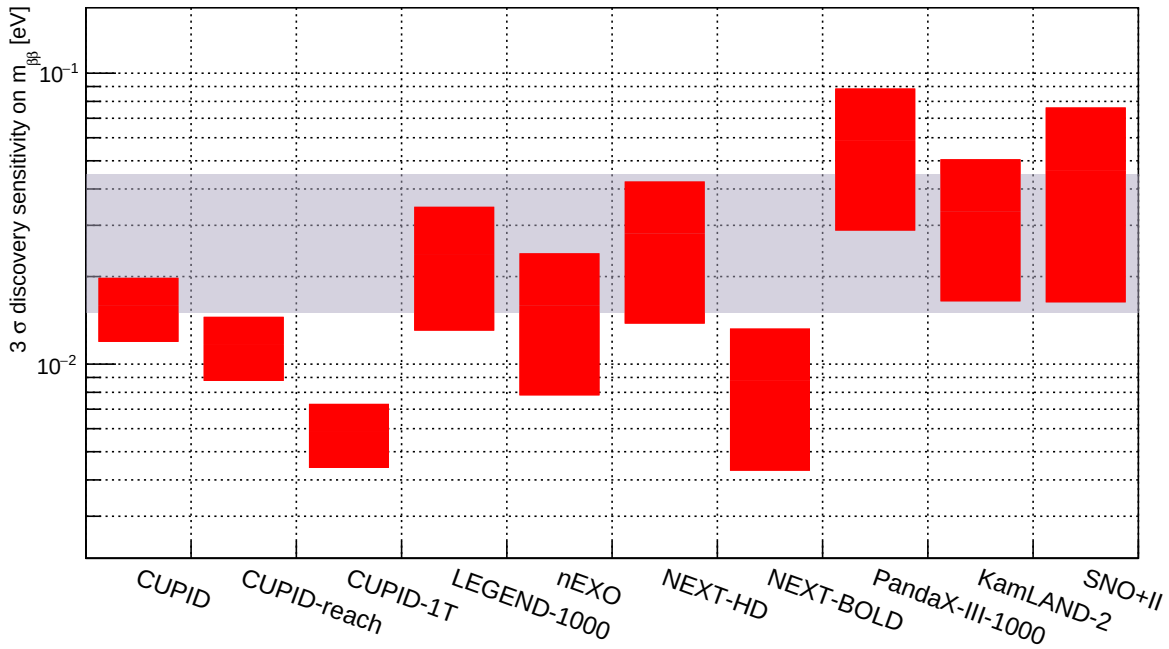


Figure 47: Discovery sensitivity for a selected set of next-generation ton-scale experiments. The grey shaded region corresponds to the parameter region allowed in the Inverted Hierarchy of the neutrino mass. The red error bars show the $m_{\beta\beta}$ values such that an experiment can make at least a 3σ discovery, within the range of the nuclear matrix elements for a given isotope. Parameters of the CUPID detector are listed in Table 10. The parameters of the other experiments are taken from Refs. [157–159].

sensitive exposure, the sensitivity on $m_{\beta\beta}$ of a given experiment has a width that depends on the NME for the corresponding isotope, which is represented by the two lines in the figure. For each isotope, we used the phase space factors from Ref. [142], and all NMEs available in literature [143–155]. The band for ^{100}Mo is narrower than for the other isotopes due to the lack of NMEs computed with the interacting shell model. A dedicated calculation was requested by the CUPID collaboration and is ongoing [156]. Fig. 47 immediately shows a viable strategy for CUPID: even with a relatively small isotope mass, we can cover most of the region allowed in the inverted ordering (IO) even for the largest NME values.

Alternatively, we can consider the case in which the $0\nu\beta\beta$ decay is mediated by currently unknown heavy neutrino(s) predicted by several extensions of the Standard Model (SM) [141]. These possibilities have an increasing appeal because they offer more natural explanations for the mass of the known neutrinos, which can be obtained within the SM only assuming an extremely small coupling to the Higgs boson. The common drawback of these models is the dependence on various assumptions and the presence of additional parameters in the theory. An additional motivation for the study of $0\nu\beta\beta$ decay mediated by heavy neutrinos is given by several independent measurements that favor the normal ordering. In parallel, the cosmological measurements are putting increasingly stronger bounds on the sum of neutrino masses, making the degenerate region unlikely. If this scenario is confirmed, the expected value of $m_{\beta\beta}$ can be considerably smaller than in the IO. On the other hand, if next generation experiments find $0\nu\beta\beta$ decay with half-lives shorter than predicted by light neutrino exchange and normal ordering, the exchange of heavy neutrinos must be involved. The new physics term of Eq. 2 is:

$$|f| = M_{\beta\beta} = \left| \frac{\sum_i V_{ei}^2 M_i}{p^2 - M_i^2} \right| \quad , \tag{4}$$

where the sum runs over the number of heavy neutrinos introduced by the SM extension under consideration, V is an extended version of the PMNS mixing matrix that comprises the heavy neutrino(s), M_i are the heavy neutrino mass eigenvalues, and p is the momentum exchanged in the reaction ($p \sim 200$ MeV).

We consider one of the several possible models as an example, which involves the exchange of an additional single heavy neutrino [160]. The discovery of $0\nu\beta\beta$ decay would give a measurement of the new term in Eq. 4, corresponding to a line in the (M_i, V_{ei}) plane shown in Fig. 48. In this hypothesis, CUPID has a discovery sensitivity superior by an order of magnitude to the current limit by GERDA.

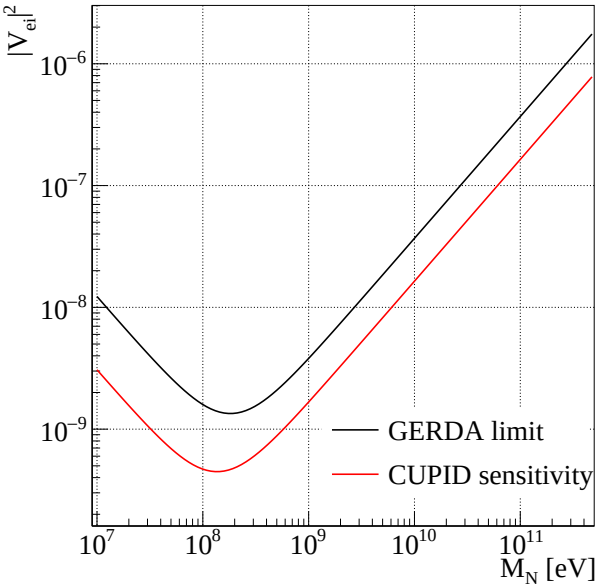


Figure 48: Sensitivity to $0\nu\beta\beta$ mediated by a single heavy neutrino exchange. The red line corresponds to a CUPID sensitivity of 10^{28} yr, the black is for the currently exclusion limit set by GERDA on ^{76}Ge [20].

9.2 Exotic processes

Although $0\nu\beta\beta$ is the main objective of CUPID, other processes are open to experimental investigation. The anticipated low background rate promises competitive sensitivities for many of them.

The accessible processes include alternative modes of double beta decay as well as more exotic processes predicted by some extensions of the Standard Model. The experimental investigation of the validity limits of fundamental physics principles like charge conservation or CPT/Lorentz invariance deserves particular attention since most of our theoretical framework is based on them. Finally, the search for dark matter candidates, a project pursued by the first experiments on $0\nu\beta\beta$, is still one of the most appealing objectives of CUPID.

9.2.1 Other double beta decays

The best double beta decay experimental sensitivity is generally for the transition to the ground state of the daughter nucleus. However, double beta decay (in both 2ν and 0ν modes) may also occur to an excited state of the daughter nucleus. In the case of $0\nu\beta\beta$, these transitions can disclose the exotic mechanisms (e.g. right-handed currents) which mediate the decay [161, 162], while for $2\nu\beta\beta$ they can provide unique insight to the details of the mechanisms responsible for the nuclear transition [163, 164]. From the experimental point of view, most of the interest is motivated by the fact that in a close-packed array like CUPID, the strong signature provided by the simultaneous detection of one or two gammas can lead to an almost background-free search. In this respect, the transitions to 0+ states are favoured while states with larger spin (e.g. 2+) are generally suppressed by angular momentum conservation. The adopted strategy exploits multiple coincidence patterns to select topological configurations characterized by a lower background contribution [165]. A number of 0+ and 2+ excited states of ^{100}Mo are accessible to CUPID with unprecedented sensitivity [166].

Exotic modes such as $\beta^+\beta^+$, $\epsilon\beta^+$ and $\epsilon\epsilon$ are generally less appealing because of the lower available energy. However, they can only be mediated by peculiar mechanisms and can therefore provide unique information on the decay details [167, 168]. With a transition energy of 1649.1 keV, ^{92}Mo is an excellent candidate, with sensitivities close to theoretical expectations for the $2\nu\beta\beta$ channel.

^{100}Mo is certainly the most favourable isotope for $0\nu\beta\beta$ searches. However, another possible $0\nu\beta\beta$ candidate is ^{98}Mo. Its large natural isotopic abundance (24.13 %) could be appealing, but the very low transition energy (112 keV), and the fact that we will work with material isotopically enriched in ^{100}Mo, ultimately leads to a very poor sensitivity for CUPID.

Exotic $0\nu\beta\beta$ decays characterized by the emission of a massless Goldstone boson, called a Majoron, are predicted by some theoretical models [169]. The precise measurements of the invisible Z width at LEP has greatly disfavoured the original Majoron triplet and pure doublet. However, several new models have been developed [170, 171]. All these models predict different (continuous) spectral shapes for the

sum energies of the emitted electrons, which extend from zero to the transition energy $Q_{\beta\beta}$:

$$\frac{dN}{dT} \sim (Q_{\beta\beta} - T)^n, \tag{5}$$

where T is the electron summed kinetic energy and the spectral index, n, depends on the decay details. Single Majoron emissions are characterized by n values between 1 and 3, while double Majoron decays can have either $n = 3$ or $n = 7$. The precise measurement of n allows one to discriminate between the Majoron processes and $2\nu\beta\beta$ ($n = 5$). As for any process characterized by continuous spectra, the experimental sensitivity is mainly limited by the background contributions and the detector mass [172–174]. Because of this, we anticipate excellent CUPID sensitivity to these processes.

9.2.2 Violations of fundamental principles

The decay of an atomic electron is probably the most sensitive test of electric charge conservation. Charge non-conservation (CNC) can be obtained by including additional interactions of leptons and photons which lead to the decay of the electron: $e \to \gamma\nu$ or $e \to \nu_e\nu_X\bar{\nu}_X$. These modes conserve all known quantities apart from electric charge. In addition, CNC can also involve interactions with nucleons. Discussions of CNC in the context of gauge theories can be found in a number of BSM gauge models [175–177].

While the signature of the neutrino mode for CNC is quite poor, the coincidence between the decayed gamma and the X-rays from atomic de-excitations can give rise to interesting topological configurations that can help to lower the background contributions. The most stringent limits on CNC have been obtained as secondary results in experiments characterized by large masses and very low backgrounds [178, 179]. Indeed, the large detection efficiency, low threshold, and excellent energy resolution expected for CUPID are crucial to detect the low energy de-ectitation X-rays or Auger electrons. This, in combination with the ton-size scale of the experiment, makes us believe we can anticipate competitive results for these processes.

Lorentz invariance and CPT violations arising from the spontaneous breaking of the underlying space-time symmetry are interesting theoretical features that can be parmeterized within the so-called Standard Model Extension (SME) [180–182]. Lorentz-violating effects in the neutrino sector can appear both in the two-neutrino and in the neutrino-less decay mode [183]. Indeed, a distortion of the two-electron summed energy is expected for $2\nu\beta\beta$ due to an extra term in the phase space factor, while $0\nu\beta\beta$ could be directly induced by a Lorentz violating term. The signature is therefore very similar to the one expected for Majoron searches with a deformation of the upper part of the $2\nu\beta\beta$ spectrum. The dominant contribution from $2\nu\beta\beta$ of ^{100}Mo, and the extremely low background expected above 2 MeV, make CUPID particularly sensitive to these effects.

The Pauli exclusion principle (PEP) is one of the basic principles of physics upon which modern atomic and nuclear physics are built. Despite its well known success, the exact validity of PEP is still an open question and experimental verification is therefore extremely important [184]. Indeed, a number of experimental investigations have been carried out both in the nuclear and atomic sector [185–187]. In all the cases, the signature is a transition between already-occupied (atomic or nuclear) levels, which is clearly prohibited by PEP. Most of the low activity experiments exploit large masses and/or low background rates to search for the emission of specific electromagnetic or nuclear radiation from atoms or nuclei. In contrast, dedicated PEP-violation searches aim at improving the sensitivity by filling already complete atomic levels with fresh electrons and measuring the corresponding X-ray transitions. Unfortunately, a model linking the two experimental observations is still missing and a comparison of the sensitivities is impossible. CUPID belongs to the first category and will exploit the excellent energy resolution and the very low background to search for the emission of X-rays, γs, or nucleons from the detector atoms and/or nuclei. PEP-prohibited nuclear decays are also possible, although a lower experimental sensitivity is anticipated for CUPID.

9.2.3 Tri-nucleon decays

Baryon number (B) conservation is an empirical symmetry of the SM. Its violation is predicted by a number of SM extensions. Furthermore, it is expected that quantum gravity theories violate B and that theories with extra dimensions permit nucleon decay via interactions with dark matter [188]. In particular, some SM extensions, which allow for small neutrino masses, anticipate ΔB=3 transitions in which three baryons can simultaneously disappear from the nucleus, frequently leaving an unstable isotope [189]. The coincidence between the tri-nucleon decay and the radioactive decay of the daughter

nuclei is then a robust signature which can help mitigate the backgrounds. The dominant ΔB=3 decay modes are $ppp \rightarrow e^+\pi^+\pi^+$, $ppn \rightarrow e^+\pi^+$, $pnn \rightarrow e^+\pi^0$, and $nnn \rightarrow \bar{\nu}\pi^0$. The decay-mode-specific signatures (charged fragments) include an initial saturated event followed by one or more radioactive decays. The invisible decay-mode signatures are composed of two successive decays and hence have two energy constraints and one time constraint.

9.2.4 Dark Matter

Although its existence is strongly suggested by several gravitational effects [190], dark matter (DM) represents one of the deepest mysteries in modern physics and its nature still remains unknown. The WIMP hypothesis is the most attractive and simplest scenario to explain DM. However, the absence of an observed signal has led to very stringent constraints on WIMP properties, encouraging physicists to look for alternatives and stronger signatures [191, 192]. In this framework, the possibility of observing a time-varying signal related to the relative motion of the earth with respect to the DM halo of the galaxy has attracted considerable interest [193]. A low energy threshold and a large mass are the most appealing features for experiments hoping to observe these effects. With the possibility of separating nuclear recoils (characterized by a lower light yield) from the dominant electron-based background, CUPID's technology is particularly well-suited for searches of this kind. We anticipate excellent sensitivity for observing the WIMP seasonal modulation generated by the motion of the Earth.

Non-WIMP DM candidates have also been explored extensively in the literature [194]. Among them, ultralight axions, which emerge as solutions to the strong CP problem in QCD, are a valid candidate for (cold) DM [195]. They are expected to couple with the electromagnetic field and directly to leptons and quarks. A comparatively large production yield is therefore expected in dense, hot matter like the sun's core. In particular, the ^{57}Fe 14.4 keV nuclear transition, which can be populated in the inner region of the sun via thermal excitation, is a good candidate for the production of a monochromatic axion, whose observation in CUPID will be based on the axio-electric effect [196]. Here, the most relevant experimental parameters are the energy threshold and the background level at very low energies. CUPID will contribute to significantly restricting the axion parameter space. A particularly promising process for the observation of solar axions in Li_2MoO_4 is the resonant absorption on ^{7}Li nuclei [197], which is accompanied by the excitation of the first nuclear level of lithium with the corresponding emission of a 477.6 keV γ-ray: $a+^7\text{Li}\rightarrow^7\text{Li}^* \rightarrow^7\text{Li}+\gamma$.

10 Alternative configuration: enriched TeO_2 detectors

Tellurium (^{130}Te isotope) has been chosen as an alternative $0\nu\beta\beta$ emitter along with ^{100}Mo for the CUPID experiment. The selection of TeO_2 has been made for two main reasons:

- TeO_2 bolometers are very well known detectors, thanks to the overall CUORE experience (material procurement, crystal handling, and detector optimization);
- The high isotopic abundance of ^{130}Te (about 33%) significantly reduces enrichment costs.

The main disadvantage of this choice relies in the fact that tellurium-based bolometers are not scintillating. Nevertheless α/β discrimination can be obtained exploiting the emission of Cherenkov light in TeO_2 crystals [42]. In TeO_2 crystals, the threshold for Cherenkov light emission is about 50 keV for electrons and about 400 MeV for α particles. Therefore, in the $0\nu\beta\beta$ region of interest, the α particle energies are below the Cherenkov emission threshold, thus emitting no light signal. It is noteworthy that the Cherenkov light emitted by the crystals steeply decreases with increasing crystal size [105], corresponding to about 100 eV for β particles in the ROI in TeO_2 crystals with CUORE's size ($5\times5\times5$ cm^3). Therefore, the detection of such low energy light requires light detectors with a RMS noise of about 20 eV.

During past few years, the light detector technology has improved to the level that "standard" Ge-based light detectors with NTD readout that can reach baseline values of few tens of eV (see Section 5.3) are now available. Even better results have been recently achieved using NTD Ge-based light detectors with Neganov-Luke amplification (see Section 5.4.1). This demonstrates that an event-by-event active particle identification is possible for full-size CUORE TeO_2 bolometers [54]. The latter light detection technique has been recently applied to two $^{130}TeO_2$ enriched crystals of 92% ^{130}Te, having a mass of 435 g compared to the 750 g CUORE crystals [198]. In this case, excellent event-by-event particle discrimination was obtained (95% acceptance level). Moreover, the two crystals showed performances in terms of baseline noise and energy resolution of 4.3 and 6.5 keV FWHM respectively, fully compatible with the CUPID baseline.

The R&D on enriched TeO_2 thus far clearly demonstrates two main issues. First, significant raw material purification will be required to eliminate radioactive Th and U, as well as the non-radioactive elements, mainly Na, Si, Fe, Cu, Sn, and Sb, which can degrade the quality of the crystals as bolometers. The second issue involves the altered isotopic concentration of enriched TeO_2 crystals if the Bridgman crystal growth technique is used, as it was for the CUORE crystals. The other problem, general for all enriched crystals, consists in finding methods for the highest possible raw material utilization coefficient (possibly 100%). In the following, we describe proposed research and development to address these issues.

10.1 Enriched $^{130}TeO_2$ raw material for crystal growth

The synthesis of TeO_2 powder and general chemical processing of raw material for crystal growth is well mastered. The crystal growth process at the Shanghai Institute of Ceramics of the Chinese Academy of Science (SICCAS) was proven to be acceptable as far as radio-contamination is concerned [199]. Nevertheless, our experiments with the small crystals [198] demonstrated that the enriched detectors had excessive radioactive backgrounds of Th and U coming from the isotopic enrichment process of natural tellurium. Accordingly, the enriched Te or TeO_2 must be purified to reduce the Th and U content. To achieve the purification of the input material, we propose an experimental effort to develop a technique to zone-refine TeO_2. If successful, this could also be used to recycle the scrap material from the crystal fabrication. In a first attempt, our team has explored chemical purification with the help of the Brookhaven National Laboratory, and we concluded that it was cost-prohibitive to reach our required levels. For a deeper, cost-effective study of possible TeO_2 purification schemes by zone-refinement, the University of South Carolina purchased a 1250 °C, computer-controlled zone-furnace from MELLEN, Inc., in Concord, NH. At the time of this writing, the zone refining facility is nearing completion. Funds are available to complete the installation, including: the platinum zone boats, natural TeO_2 powder for the trials, and some evaluation of the results by ICP-MS.

The ICP-MS tests are being explored in cooperation with the Pacific Northwest National Laboratory. A possible side effect of this activity is that the equipment used for the purification of TeO_2 (with a melting point 733 °C) could be used for the purification of Li_2MoO_4 (melting point 705 °C) or of MoO_3 (melting point 795 °C). The latter is a principal precursor of the raw material used for Li_2MoO_4crystal growth. Because all these materials have close melting points, the same type of crucible (e.g. platinum)

can be used for all. Accordingly, the R&D to explore the purification of input and scrap TeO_2 can also serve as R&D for the Li_2MoO_4 option for CUPID. In any case, a strong case can be made to develop the zone refining technique for TeO_2 and to attempt a similar technique for Li_2MoO_4. To start in this direction, MELLEN Inc. was contacted to learn about zone refining TeO_2 with the MELLEN Series EDG12.5-Sunfire, 1250 °C Programmable Multi-Zone Furnace. It has a 6-inch bore, with 24 one-inch zones. Delivery of the apparatus was in late August 2018 and commissioning ended in Spring 2019. The purification of input and scrap TeO_2 will be possible in this furnace. Note, the CUPID group from the University of South Carolina has past experience with these methods and were able to achieve 70% overall yield in detector mass from Ge enriched to 88% in ^{76}Ge for the MAJORANA DEMONSTRATOR. This required continuous zone refining of scrap material, where the yield is 98%, rather than chemical reprocessing. The cost of the TeO_2 enriched in ^{130}Te will be significantly less expensive than enriched Ge (15-20 K$/kg).

10.2 Enriched $^{130}TeO_2$ crystal growth

Preliminary crystal growth tests have shown that the method used for the production of CUORE crystals at SICCAS is not applicable when creating enriched $^{130}TeO_2$ crystals. Two trial enriched detectors were produced for feasibility tests and the ^{130}Te fraction was reduced from 93% in the starting material (metallic powder) to 73% in the final crystal due to the migration of the material from the natural seed throughout the crystal ingot during the growth process. This is because the growth method applied (modified Bridgman technique) requires the use of a large seed, which is partially melted in the initial phase of the crystal growth with consequent alteration of the isotopic concentration of the resulting crystal. There are two solutions to this problem: (i) maintain the same method of growth, but use an enriched seed, possibly obtained through the Czochralski method; (ii) use the Czochralski technique for the entire crystal production process.

Note that in the Czochralski method, a very tiny seed is used with a mass negligible compared to that of the crystal. Therefore, diluting the isotopic concentration is not an issue in this case. If we apply the Czochralski method, this would most likely have to be done in the US since this technology is not well mastered at SICCAS. Early communications have begun with Gooch and Housego Inc. in Cleveland, Ohio, to determine if producing the enriched TeO_2 CUORE crystals by the Czochralski technique would be cost-competitive. Moreover, since we still want to do purification in the US, one advantage of growing the crystals with Gooch and Housego Inc. would be to avoid the expense and complications of shipping scrap back to the US and then returning reprocessed material back to China. While the cost per crystal could be higher, the savings in the complex import/export logistics could be substantial. Moreover, the additional cost and complication of providing enriched seeds might well make the US production of the crystals, as well as the US purchase, purification, and recycling of the TeO_2, possibly cost-competitive.

10.3 Recovery and recycling

Our experience with CUORE demonstrated that only 30% to 35% of the input material ended up in crystals. This implies that a large amount of tellurium oxide must be re-processed for each crystal pulled. If the crystals were produced at SICCAS, the many shipments of scrap material for reprocessing, and its return to SICCAS, would be very complicated, costly and time consuming. In addition, SICCAS does not grow crystals by the Czochralski method, so large crystal seeds would have to be grown in the US and shipped to China periodically.

As described above, we have identified one possible scenario for enriched crystal production, which includes an optimized efficiency in the purification of the input TeO_2, as well as the recycling of the scrap material from the crystal fabrication. This option would have the TeO_2 crystals grown by the Czochralski method in the U.S. where zone-refinement would be used for both primary and recycling purification.

11 Implementation and Timeline

The most time-sensitive, critical path task is the procurement of the enriched ^{100}Mo isotope and production of the crystals. Given the relatively conservative baseline design of the CUPID detector, and the strategy of deploying CUPID in the existing CUORE cryostat as soon as CUORE finishes data taking, the commissioning and the scientific operations of the detector could start approximately five years after the start of the project.

12 CUPID Group of Interest

The CUPID Interest group is a robust international collaboration that brings together an array of experts that will contribute to a successful program.

Argonne National Laboratory, Argonne, IL, USA
W.R. Armstrong, C. Chang, K. Hafidi, M. Lisovenko, V. Novosad, J. Pearson, T. Polakovic, G. Wang, V. Yefremenko, J. Zhang

INFN Laboratori Nazionali del Gran Sasso, Assergi (AQ) Italy
C. Bucci, L. Canonica, L. Cappelli, V. Caracciolo, S. Copello, A. D'Addabbo, P. Gorla, S. Nisi, D. Orlandi, C. E. Pagliarone, L. Pattavina, S. Pirro, C. Rusconi, K. Schaffner

Lawrence Berkeley National Laboratory and University of California, Berkeley, CA, USA
G. Benato, A. Drobizhev , B. K. Fujikawa, R. Huang, Yu. G. Kolomensky, L. Marini, E. Norman, M. Sakai, B. Schmidt, V. Singh, K. Vetter, S. Wagaarachchi, J. Wallig, B. Welliver

Virginia Tech, Blacksburg, VA, USA
S. Dell'Oro, T. O'Donnell

INFN Sezione di Bologna and University of Bologna, Bologna, Italy
S. Zucchelli, N. Moggi

INFN Sezione di Bologna and CNR-IMM, Bologna, Italy
V.Boldrini, F. Mancarella, R.Rizzi

Massachusetts Institute of Technology, Cambrige, MA, USA
J. Johnston, J. Ouellet, J. Formaggio, L. Winslow

University of South Carolina, Columbia, SC, USA
F. Avignone, C. Rusconi, R. Creswick and K. Wilson

INFN Laboratori Nazionali di Frascati, Frascati, Italy
A. Franceschi, T. Napolitano

INFN Sezione di Genova and University of Genova, Genova, Italy
A. Caminata, S. Di Domizio, M. Pallavicni

SIMAP Grenoble, France
M. Velazquez

University of Science and Technology of China, Hefei, China
H. Peng, M. Xue

KINR Kiev, Ukraine
F. Danevich, V. Kobychev, O. Polischuk, V. Tretyak

INFN Laboratori Nazionali di Legnaro, Italy
O. Azzolini, G. Keppel, C. Pira

INFN Sezione di Roma and Gran Sasso Science Institute, L'Aquila, Italy
F. Ferroni

INFN Laboratori Nazionali del Gran Sasso and Gran Sasso Science Institute, L'Aquila, Italy
V. Dompè, G. Fantini

University of California Los Angeles, Los Angeles, CA, USA
K. Alfonso, H.Z. Huang

IPNL Lyon, France
Q. Arnaud, C. Augier, J. Billard, A. Cazes, F. Charlieux, E. Elkhoury, J. Gascon, M. De Jesus, A. Juillard, D. Misiak, V. Sanglard, L. Vagneron

INFN Sezione di Milano Bicocca and University of Milano Bicocca, Milano, Italy
M. Beretta, M. Biassoni, C. Brofferio, S. Capelli, P. Carniti, D. Chiesa, M. Clemenza, O. Cremonesi, M. Faverzani, E. Ferri, A. Giachero, L. Gironi, C. Gotti, M. Nastasi, I. Nutini, L. Pagnanini, M. Pavan, G. Pessina, S. Pozzi, E. Previtali, A. Puiu, M. Sisti

ITEP Moscow, Russia
A. Barabash, S. Konovalov, V. Yumatov

Yale University, New Haven, CT, USA
K. Heeger, R. Maruyama, J. Nikkel, D. Speller, P. T. Surukuchi

NIIC Novosibirsk, Novosibirk, Russia
V. Shlegel

CSNSM Orsay, France
L. Bergé, M. Chapellier, L. Dumoulin, A. Giuliani, H. Khalife, P. de Marcillac, S. Marnieros, E. Olivieri, D. Poda, T. Redon, A. Zolotarova

LAL Orsay, France
M. Brière, C. Bourgeois, E. Guerard, P. Loaiza

INFN Sezione di Padova, Padova, Italy
L. Taffarello

Drexel University, Philadelphia, PA, USA
G. Karapetrov

INFN Sezione di Roma and Sapienza University of Rome, Rome, Italy
F. Bellini, L. Cardani, N. Casali, A. Cruciani, I. Dafinei, V. Pettinacci, G. D' Imperio, C. Tomei, M. Vignati

INFN Sezione di Roma and CNR-NANOTEC, Rome, Italy
I. Colantoni

CEA Saclay, France
E. Armengaud, A. Charrier, M. de Combarieu, F. Ferri, Ph. Gras, M. Gros, D. Helis, X.F. Navick, C. Nones, P. Pari, B. Paul

Cal Poly, San Luis Obispo, CA, USA
T. Gutierrez

Shanghai Jiao Tong University, Shangai, China
K. Han

Fudan University, Shangai, China
L. Ma, Y. Shen, W. He

Universidad de Zaragoza, Zaragoza, Spain
M. Martinez

13 Bibliography

[1] M. Tanabashi *et al.* (Particle Data Group), Phys. Rev. **D98**, 030001 (2018).

[2] S. R. Elliott and P. Vogel, Ann. Rev. Nucl. Part. Sci. **52**, 115 (2002), arXiv:hep-ph/0202264 [hep-ph] .

[3] F. T. Avignone, S. R. Elliott, and J. Engel, Rev. Mod. Phys. **80**, 481 (2008).

[4] O. Cremonesi and M. Pavan, Adv. High Energy Phys. **2014**, 951432 (2014), arXiv:1310.4692 [physics.ins-det] .

[5] A. Giuliani and A. Poves, Adv. High Energy Phys. **2012**, ID 857016 (2012).

[6] K. Alfonso *et al.* (CUORE), Phys. Rev. Lett. **115**, 102502 (2015), arXiv:1504.02454 [nucl-ex] .

[7] C. Alduino *et al.* (CUORE), Phys. Rev. Lett. **120**, 132501 (2018), arXiv:1710.07988 [nucl-ex] .

[8] J. W. Beeman *et al.*, JINST **8**, P05021 (2013), arXiv:1303.4080 [physics.ins-det] .

[9] L. Cardani *et al.*, J. Phys. **G41**, 075204 (2014), arXiv:1312.4680 [nucl-ex] .

[10] J. W. Beeman *et al.*, Phys. Lett. B **710**, 318 (2012).

[11] L. Cardani *et al.*, JINST **8**, P10002 (2013).

[12] T. Bekker *et al.*, Astropart. Phys. **72**, 38 (2016).

[13] E. Armengaud *et al.*, The European Physical Journal C **77**, 785 (2017), arXiv:arXiv:1704.01758v1 .

[14] A. S. Barabash *et al.*, The European Physical Journal C **76**, 487 (2016).

[15] O. Azzolini *et al.* (CUPID-0), Phys. Rev. Lett. **120**, 232502 (2018).

[16] O. Azzolini *et al.* (CUPID), Phys. Rev. Lett. **123**, 032501 (2019), arXiv:1906.05001 [nucl-ex] .

[17] D. V. Poda (CUPID-Mo), "^{100}Mo $\beta\beta$ decay search in the CUPID-Mo experiment with enriched scintillating bolometers," Poster presented at XXVIII Int. Conf. Neutrino 2018, Heidelberg, Germany, 04–09 June, 2018.

[18] A. D'Addabbo *et al.* (CUORE), *17th International Workshop on Low Temperature Detectors (LTD 17) Kurume City, Japan, July 17-21, 2017*, J. Low. Temp. Phys. **193**, 867 (2018), arXiv:1805.06209 [physics.ins-det] .

[19] C. Alduino *et al.*, (2019), arXiv:1904.05745 [physics.ins-det] .

[20] M. Agostini *et al.* (GERDA), Phys. Rev. Lett. **120**, 132503 (2018), arXiv:1803.11100 [nucl-ex] .

[21] C. E. Aalseth *et al.* (Majorana), Phys. Rev. Lett. **120**, 132502 (2018), arXiv:1710.11608 [nucl-ex] .

[22] M. Auger *et al.* (EXO Collaboration), Phys. Rev. Lett. **109**, 032505 (2012).

[23] J. Martín-Albo *et al.* (NEXT), JHEP **05**, 159 (2016), arXiv:1511.09246 [physics.ins-det] .

[24] A. Gando *et al.* (KamLAND-Zen Collaboration), Phys. Rev. Lett. **117**, 082503 (2016).

[25] S. Andringa *et al.* (SNO+), Adv. High Energy Phys. **2016**, 6194250 (2016), arXiv:1508.05759 [physics.ins-det] .

[26] J. Myslik (LEGEND), in *13th Conference on the Intersections of Particle and Nuclear Physics (CIPANP 2018) Palm Springs, California, USA, May 29-June 3, 2018* (2018) arXiv:1810.00849 [physics.ins-det] .

[27] D. V. Poda *et al.*, AIP Conference Proceedings **1894**, 020017 (2017), https://aip.scitation.org/doi/pdf/10.1063/1.5007642 .

[28] V. Alenkov *et al.*, (2019), arXiv:1903.09483 [hep-ex] .

[29] S. Pirro *et al.*, Physics of Atomic Nuclei **69**, 2109 (2006).

[30] O. Azzolini *et al.* (CUPID), Eur. Phys. J. **C78**, 428 (2018), arXiv:1802.06562 [physics.ins-det] .

[31] C. Arnaboldi *et al.*, Astroparticle Physics **34**, 797 (2011).

[32] A. Giuliani, "The Mid and Long Term Future of Neutrinoless Double Beta Decay," (2018).

[33] X. Chen *et al.*, Sci.China Phys.Mech.Astron. **60**, 061011 (2017).

[34] E. Fiorini and T. O. Niinikoski, Nuclear Instruments and Methods in Physics Research **224**, 83 (1984).

[35] A. Giuliani, Journal of Low Temperature Physics **167** (2012), 10.1007/s10909-012-0576-9.

[36] D. Poda and A. Giuliani, Int. J. Mod. Phys. A **32**, 1743012 (2017).

[37] C. Alduino *et al.* (CUORE), Eur. Phys. J. C **77**, 543 (2017).

[38] D. R. Artusa *et al.* (CUORE), Eur. Phys. J. **C74**, 3096 (2014), arXiv:1404.4469 [nucl-ex] .

[39] E. Armengaud *et al.*, Eur. Phys. J. C **77**, 785 (2017).

[40] A. Giuliani, F. A. Danevich, and V. I. Tretyak, The European Physical Journal C **78**, 272 (2018).

[41] C. Arnaboldi *et al.* (CUORICINO), Phys. Rev. **C78**, 035502 (2008).

[42] T. Tabarelli de Fatis, Eur. Phys. J. **C65**, 359 (2010).

[43] A. D. *et al*, Cryogenics **93** (2018), 10.1016/j.cryogenics.2018.05.001, arXiv:1712.02753 [nucl-ex] .

[44] A. Alessandrello *et al.*, Nucl. Instrum. Meth. **B142**, 163 (1998).

[45] E. Buccheri *et al.*, Nucl. Instrum. Meth. **A768**, 130 (2014), arXiv:1405.0852 [physics.ins-det] .

[46] G. Benato *et al.*, Journal of Instrumentation **13**, P01010 (2018).

[47] C. Arnaboldi *et al.*, JINST **13**, P02026 (2018).

[48] S. Di Domizio *et al.*, JINST **13**, P12003 (2018).

[49] C. Bucci *et al.*, JINST **12**, P12013 (2017).

[50] C. Arnaboldi *et al.*, Rev. Sci. Instrum. **86**, 124703 (2015).

[51] P. Carniti *et al.*, Rev. Sci. Instrum. **87**, 054706 (2016).

[52] K. Alfonso *et al.*, JINST **13**, P02029 (2018).

[53] S. Stalio, G. D. Carlo, S. Parlati, and P. Spinnato, CoRR **abs/1212.4658** (2012), arXiv:1212.4658 .

[54] L. Bergé *et al.*, Physical Review C **97**, 1 (2018), arXiv:1710.03459 .

[55] S. Cecchini *et al.*, EPL **87**, 39001 (2009), arXiv:0907.5235 [hep-ex] .

[56] G. Bellini *et al.* (Borexino), JINST **6**, P05005 (2011), arXiv:1101.3101 [physics.ins-det] .

[57] D. Mei and A. Hime, Phys. Rev. **D73**, 053004 (2006), arXiv:astro-ph/0512125 [astro-ph] .

[58] E. Andreotti *et al.* (CUORICINO), Astropart. Phys. **34**, 18 (2010), arXiv:0912.3779 [nucl-ex] .

[59] F. Bellini *et al.*, Astropart. Phys. **33**, 169 (2010).

[60] C. Arnaboldi, G. Pessina, and S. Pirro, Nucl. Instrum. Meth. **A559**, 826 (2006).

[61] M. Barucci, V. Martelli, and G. Ventura, J Low Temp Phys **157**, 541 (2009).

[62] ECP, `http://www.ecp.ru/eng/`.

[63] D. M. Chernyak *et al.*, Nucl. Instrum. Meth. A **729**, 856 (2013).

[64] L. Bergé *et al.*, JINST **9**, P06004 (2014).

[65] D. M. Chernyak *et al.*, Opt. Mat. **49**, 67 (2015).

[66] L. L. Nagornaya *et al.*, IEEE Trans. Nucl. Sci. **56**, 2513 (2009).

[67] L. Gironi *et al.*, JINST **5**, P11007 (2010).

[68] P. Belli *et al.*, Nucl. Phys. A **846**, 143 (2010).

[69] R. Arnold *et al.*, Nucl. Instr. Meth. A **474**, 93 (2001).

[70] A. M. Dubovik *et al.*, Acta Phys. Pol. A **117**, 15 (2010).

[71] O. P. Barinova *et al.*, Nucl. Instr. Meth. A **613**, 54 (2010).

[72] O. P. Barinova and others., Nucl. Instrum. Meth. **A607**, 573 (2009).

[73] V. D. Grigorieva *et al.*, J. Mat. Sci. Eng. B **7**, 63 (2017).

[74] A. A. Pavlyuk *et al.*, *Proceedings of The APSAM-92, Asia Pacific Society for Advanced Materials (Shanghai, P.R.C., 26–29 April 1992), Institute of Materials Research, Tohoku University, Sendai, Japan*, , 164 (1993).

[75] Y. A. Borovlev *et al.*, J. Cryst. Growth **229**, 305 (2001).

[76] M. Velazquez *et al.*, Solid State Sci. **65**, 41 (2017).

[77] G. Buşe *et al.*, Nucl. Instr. Meth. A **891**, 87 (2018).

[78] C. Stelian *et al.*, J. Cryst. Growth **492**, 6 (2018).

[79] P. Chen *et al.*, Materials Letters **215**, 225 (2018).

[80] F. Alessandria *et al.* (CUORE), Astropart. Phys. **35**, 839 (2012).

[81] A. Alessandrello *et al.*, Nucl. Instrum. Meth. **A412**, 454 (1998).

[82] E. Andreotti *et al.*, Nucl. Instrum. Meth. **A664**, 161 (2012).

[83] F. Bellini, Int. J. Mod. Phys. A **33**, 1843003 (2018).

[84] S. Pirro and P. Mauskopf, Radiat. Meas. **67**, 161 (2017).

[85] J. W. Beeman *et al.*, JINST **8**, P07021 (2013).

[86] D. R. Artusa *et al.*, Eur. Phys. J. C **76**, 364 (2016).

[87] M. Barucci *et al.*, (2019), arXiv:1901.11009 [physics.ins-det] .

[88] M. Mancuso *et al.*, EPJ Web Conf. **65**, 04003 (2014).

[89] N. Coron *et al.*, Opt. Eng. **43**, 1568 (2004).

[90] P. N. Luke, J. Appl. Phys. **64**, 6858 (1988).

[91] M. A. Dobbs *et al.*, Review of Scientific Instruments **83**, 073113 (2012), https://doi.org/10.1063/1.4737629 .

[92] K. Hattori *et al.*, Journal of Low Temperature Physics **184**, 512 (2016).

[93] M. Pyle *et al.*, Nuclear Instruments and Methods in Physics Research Section A: Accelerators, Spectrometers, Detectors and Associated Equipment **559**, 405–407 (2006).

[94] K. Irwin and G. Hilton, "Transition-edge sensors," in *Cryogenic Particle Detection*, edited by C. Enss (Springer Berlin Heidelberg, Berlin, Heidelberg, 2005) pp. 63–150.

[95] R. Holm and W. Meissner, Zeitschrift für Physik **74**, 715 (1932).

[96] R. Hennings-Yeomans *et al.*, (2017), arXiv:1711.03648 [physics.ins-det] .

[97] F. Aubin *et al.*, Journal of Low Temperature Physics (2018), 10.1007/s10909-018-1877-4.

[98] P. K. Day *et al.*, Nature **425**, 817 EP (2003).

[99] L. J. Swenson *et al.*, Appl. Phys. Lett. **96**, 263511 (2010), arXiv:1004.5066 [physics.ins-det] .

[100] D. C. Moore *et al.*, Appl. Phys. Lett. **100**, 232601 (2012), arXiv:1203.4549 [astro-ph.IM] .

[101] L. Cardani *et al.*, Supercond. Sci. Technol. **31**, 075002 (2018), arXiv:1801.08403 [physics.ins-det] .

[102] E. S. Battistelli *et al.*, Eur. Phys. J. **C75**, 353 (2015), arXiv:1505.01318 [physics.ins-det] .

[103] F. Bellini *et al.*, Appl. Phys. Lett. **110**, 033504 (2017), arXiv:1606.04565 [physics.ins-det] .

[104] F. Danevich *et al.*, Nucl. Instr. Meth. A **336**, 26 (2014), arXiv:1404.7846 .

[105] N. Casali *et al.*, The European Physical Journal C **75**, 12 (2015), arXiv:arXiv:1403.5528v1 .

[106] E. Hansen, N. DePorzio, and L. Winslow, Journal of Instrumentation **12**, P09018 (2017), arXiv:1609.00720 .

[107] M. Mancuso *et al.*, EPJ Web of Conferences **65**, 04003 (2014).

[108] N. Casali, Astroparticle Physics **91**, 44 (2017), arXiv:1604.01587 .

[109] D. V. Poda, in *AIP Conference Proceedings*, Vol. 1894 (2017) p. 020017, arXiv:1709.07846 .

[110] M. Velázquez *et al.*, Solid State Sciences **65**, 41 (2017).

[111] G. Buse *et al.*, Nucl. Instr. Meth. A **891**, 87 (2018), arXiv:1801.07909 .

[112] O. Barinova, S. Kirsanova, A. Sadovskiy, and I. Avetissov, Journal of Crystal Growth **401**, 853 (2014).

[113] D. A. Spassky *et al.*, Journal of Luminescence **186**, 229 (2017).

[114] J. Caravaca *et al.*, Physical Review C **95**, 055801 (2017), arXiv:1610.02029 .

[115] M. Pyle, E. Feliciano-Figueroa, and B. Sadoulet, (2015), arXiv:1503.01200 [astro-ph.IM] .

[116] F. Alessandria *et al.*, Astroparticle Physics **45**, 13 (2013).

[117] M.-M. Chen and R. H. Wang, Journal of Vacuum Science & Technology A **1**, 708 (1983), https://doi.org/10.1116/1.571983 .

[118] J. N. Sasserath and J. Vivalda, Journal of Vacuum Science & Technology A **8**, 3914 (1990), https://doi.org/10.1116/1.576420 .

[119] A. S. Barabash *et al.* (SuperNEMO), JINST **12**, P06002 (2017), arXiv:1702.07176 [physics.ins-det] .

[120] A. S. B. et al. (SuperNEMO Collaboration) (SuperNEMO), JINST **12**, P06002 (2017).

[121] O. Azzolini *et al.* (CUPID), Eur. Phys. J. **C79**, 583 (2019), arXiv:1904.10397 [nucl-ex] .

[122] D. M. C. *et al*, Eur. Phys. J. C **72**, 1989 (2012).

[123] D. M. C. *et al*, Eur. Phys. J. C **74**, 2913 (2014).

[124] D. M. C. *et al*, Eur. Phys. J. C **77**, 3 (2016).

[125] C. Alduino *et al.* (CUORE), Eur. Phys. J. C **77**, 13 (2017), arXiv:1609.01666 [nucl-ex] .

[126] C.-M. coll., In preparation (2019).

[127] G. Heusser, Ann. Rev. Nucl. Part. Sci. **45**, 543 (1995).

[128] S. Cebrián, Int. J. Mod. Phys. A **32**, 1743006 (2017), arXiv:1708.07449 [nucl-ex] .

[129] J. J. Back and Y. A. Ramachers, Nucl. Instrum. Meth. **A586**, 286 (2008), arXiv:0709.3472 [nucl-ex] .

[130] C. J. Martoff and P. D. Lewin, Computer Physics Communications **72**, 96 (1992).

[131] D. Chernyak, *Development of cryogenic low background detector based on enriched zinc molybdate crystal scintillators to search for neutrinoless double beta decay of* ^{100}*Mo*, Ph.D. thesis, CSNSM, Orsay (2015), arXiv:1507.04591 [physics.ins-det] .

[132] F. A. Danevich *et al.*, AIP Conf. Proc. **1686**, 020007 (2015).

[133] D. M. Mei and A. Hime, Phys. Rev. D **73**, 053004 (2006).

[134] M. B. Chadwick *et al.*, Nucl. Data Sheets **112**, 2887 (2011).

[135] Https://www.nndc.bnl.gov/capgam/index.html.

[136] M. Bhattacharya, E. G. Adelberger, and H. E. Swanson, Phys. Rev. C **73**, 055802 (2006).

[137] D. H. Wilkinson and D. E. Alburger, Phys. Rev. Lett. **26**, 1127 (1971).

[138] N. F. de Barros and K. Zuber, J. Phys. G **38**, 105201 (2011).

[139] H. Ejiri *et al.*, Phys. Rev. Lett. **85**, 2917 (2000).

[140] H. Ejiri and S. R. Elliott, Phys. Rev. C **95**, 055501 (2017).

[141] S. Dell'Oro, S. Marcocci, M. Viel, and F. Vissani, Adv. High Energy Phys. **2016**, 2162659 (2016), arXiv:1601.07512 [hep-ph] .

[142] J. Kotila and F. Iachello, Phys. Rev. **C85**, 034316 (2012), arXiv:1209.5722 [nucl-th] .

[143] J. Barea, J. Kotila, and F. Iachello, Phys. Rev. **C91**, 034304 (2015), arXiv:1506.08530 [nucl-th] .

[144] F. Šimkovic, V. Rodin, A. Faessler, and P. Vogel, Phys. Rev. **C87**, 045501 (2013), arXiv:1302.1509 [nucl-th] .

[145] J. Hyvärinen and J. Suhonen, Phys. Rev. **C91**, 024613 (2015).

[146] A. Neacsu and M. Horoi, Phys. Rev. **C91**, 024309 (2015), arXiv:1411.4313 [nucl-th] .

[147] J. Menendez, A. Poves, E. Caurier, and F. Nowacki, Nucl. Phys. **A818**, 139 (2009), arXiv:0801.3760 [nucl-th] .

[148] P. K. Rath *et al.*, Phys. Rev. **C88**, 064322 (2013), arXiv:1308.0460 [nucl-th] .

[149] T. R. Rodriguez and G. Martinez-Pinedo, Phys. Rev. Lett. **105**, 252503 (2010), arXiv:1008.5260 [nucl-th] .

[150] M. T. Mustonen and J. Engel, Phys. Rev. **C87**, 064302 (2013), arXiv:1301.6997 [nucl-th] .

[151] A. Meroni, S. T. Petcov, and F. Simkovic, JHEP **02**, 025 (2013), arXiv:1212.1331 [hep-ph] .

[152] N. López Vaquero, T. R. Rodríguez, and J. L. Egido, Phys. Rev. Lett. **111**, 142501 (2013), arXiv:1401.0650 [nucl-th] .

[153] J. M. Yao *et al.*, Phys. Rev. **C91**, 024316 (2015), arXiv:1410.6326 [nucl-th] .

[154] M. Horoi and A. Neacsu, Phys. Rev. **C93**, 024308 (2016), arXiv:1511.03711 [nucl-th] .

[155] R. A. Sen'kov and M. Horoi, Phys. Rev. **C90**, 051301 (2014), arXiv:1411.1667 [nucl-th] .

[156] J. Menendez, "private communication," .

[157] M. Agostini, G. Benato, and J. Detwiler, Phys. Rev. **D96**, 053001 (2017), arXiv:1705.02996 [hep-ex] .

[158] J. J. Gomez-Cadenas (2019) arXiv:1906.01743 [hep-ex] .

[159] J. Galan *et al.*, (2019), arXiv:1903.03979 [physics.ins-det] .

[160] M. Mitra, G. Senjanovic, and F. Vissani, Nucl. Phys. **B856**, 26 (2012), arXiv:1108.0004 [hep-ph] .

[161] T. Tomoda, Phys. Lett. **B474**, 245 (2000), arXiv:hep-ph/9909330 [hep-ph] .

[162] F. Simkovic and A. Faessler, *Progress in particle and nuclear physics. Vol. 48, Pt. 1: Neutrinos in astro, particle and nuclear physics. Proceedings, International School of Nuclear Physics, 23rd Course, Erice, Italy, September 18-26, 2001*, Prog. Part. Nucl. Phys. **48**, 201 (2002), [,201(2001)], arXiv:hep-ph/0112272 [hep-ph] .

[163] M. Aunola and J. Suhonen, Nuclear Physics A **602**, 133 (1996).

[164] J. Suhonen, Phys. Rep. **300**, 124 (1998).

[165] E. Andreotti *et al.*, Phys. Rev. C **85**, 045503 (2012).

[166] A. Barabash, in *AIP Conference Proceedings*, Vol. 942 (AIP, 2007) pp. 8–12.

[167] J. D. Vergados, Nucl. Phys. **B218**, 109 (1983).

[168] J. Kotila, J. Barea, and F. Iachello, Phys. Rev. C **89**, 064319 (2014).

[169] G. Gelmini and M. Roncadelli, Physics Letters B **99**, 411 (1981).

[170] C. P. Burgess and J. M. Cline, Phys. Rev. D **49**, 5925 (1994).

[171] P. Bamert, C. Burgess, and R. Mohapatra, Nuclear Physics B **449**, 25 (1995).

[172] S. R. Elliott, A. A. Hahn, and M. K. Moe, Phys. Rev. Lett. **59**, 1649 (1987).

[173] R. Arnold *et al.*, Nuclear Physics A **765**, 483 (2006).

[174] A. Gando *et al.* (KamLAND-Zen Collaboration), Phys. Rev. C **86**, 021601 (2012).

[175] M. Voloshin and L. Okun, JETP Lett **28**, 145 (1978).

[176] L. Okun and Y. Zeldovich, Physics Letters B **78**, 597 (1978).

[177] A. Ignatiev, V. Kuzmin, and M. Shaposhnikov, Physics Letters B **84**, 315 (1979).

[178] P. Belli *et al.*, Phys. Rev. D **61**, 117301 (2000).

[179] H. O. Back *et al.*, Phys. Lett. **B525**, 29 (2002).

[180] D. Colladay and V. A. Kostelecký, Phys. Rev. D **55**, 6760 (1997).

[181] D. Colladay and V. A. Kostelecký, Phys. Rev. D **58**, 116002 (1998).

[182] V. A. Kostelecký, Phys. Rev. D **69**, 105009 (2004).

[183] J. S. Díaz, Phys. Rev. D **89**, 036002 (2014).

[184] O. Greenberg, Nuclear Physics B - Proceedings Supplements **6**, 83 (1989).

[185] G. Bellini *et al.* (Borexino Collaboration), Phys. Rev. C **81**, 034317 (2010).

[186] H. Shi *et al.*, The European Physical Journal C **78**, 319 (2018).

[187] P. Belli *et al.*, Physics Letters B **460**, 236 (1999).

[188] K. S. Babu *et al.*, in *Proceedings, 2013 Community Summer Study on the Future of U.S. Particle Physics: Snowmass on the Mississippi (CSS2013): Minneapolis, MN, USA, July 29-August 6, 2013* (2013) arXiv:1311.5285 [hep-ph] .

[189] K. Babu, I. Gogoladze, and K. Wang, Physics Letters B **570**, 32 (2003).

[190] A. Del Popolo, in *AIP Conference Proceedings*, Vol. 1548 (AIP, 2013) pp. 2–63.

[191] L. Roszkowski, E. M. Sessolo, and S. Trojanowski, Reports on Progress in Physics **81**, 066201 (2018).

[192] A. G. *et al.*, The European Physical Journal C **78**, 203 (2018).

[193] F. Mayet *et al.*, Physics Reports **627**, 1 (2016).

[194] H. Baer, K.-Y. Choi, J. E. Kim, and L. Roszkowski, Physics Reports **555**, 1 (2015), dark matter production in the early Universe: Beyond the thermal WIMP paradigm.

[195] J. Ipser and P. Sikivie, Phys. Rev. Lett. **50**, 925 (1983).

[196] F. Alessandria *et al.* (CUORE), JCAP **1305**, 007 (2013), arXiv:1209.2800 [hep-ex] .

[197] M. M. *et al.*, Physical review D **64**, 115016 (2001).

[198] D. R. Artusa *et al.*, Physics Letters, Section B: Nuclear, Elementary Particle and High-Energy Physics **767**, 321 (2017), arXiv:1610.03513 .

[199] C. Arnaboldi *et al.*, Journal of Crystal Growth **312**, 2999 (2010), arXiv:1005.3686 .